Large-Eddy Simulations of Fully Developed Turbulent Channel and Pipe Flows with Smooth and Rough Walls

Thesis by

Namiko Saito

In Partial Fulfillment of the Requirements

for the Degree of

Doctor of Philosophy

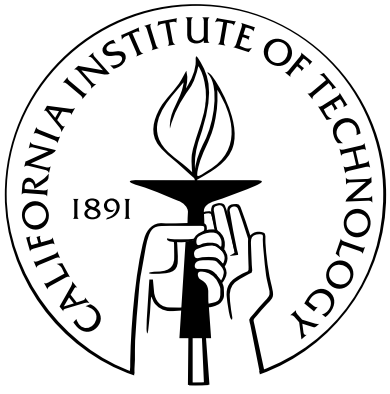

California Institute of Technology

Pasadena, California

2014

(Submitted February 14, 2014)

To those who brighten my life...

Acknowledgements

I would like to express my sincere gratitude to my advisor, Professor Dale Pullin for being the first to engage me in this area of research. His mentorship has enticed me into the academic world and increased my competence. He has given me the freedom to pursue my ideas while his warm and steady guidance has allowed me to feel safe in the thought that his support will always be there. I am truly fortunate to be his student and hopeful that he will always remain my lifelong mentor.

I am deeply thankful to my committee members: Professor Daniel Meiron, Professor Beverley McKeon, and Professor Tim Colonius. Their parts in the completion of this work have all been essential. I am profoundly indebted to Professor Hugh Blackburn (Monash University) for providing me with his expertise and many hours of valuable discussion. My life in GALCIT has been supported by many professors and their encouragement is deeply appreciated; I thank Professor John Dabiri, Professor Mory Gharib, Professor Anatol Roshko, Professor Paul Dimotakis, Professor Joe Shepherd, Professor Hans Hornung, Professor Tony Leonard, Professor Michael Ortiz, Professor Chiara Daraio, Professor Sergio Pellegrino, and Professor Guruswami Ravichandran.

I would like to gratefully acknowledge Ms. Cheryl Gause, Ms. Alexandra Katsas, Ms. Dimity Nelson, Ms. Christine Ramirez, Ms. Jennifer Stevenson, Ms. Denise Ruiz, Ms. Lydia Suarez, and Ms. Barbara McKinzie Slater. Their support has always been warm and personal.

My life at Caltech has been greatly enriched by my friends here. I thank my group members Alejandro Lopez, Marcello Gori, and Dustin Summy. I am especially thankful to Michio Inoue for sharing invaluable help and great friendship. My masters class has cultivated my affection towards the Caltech community; thank you, Jocelyn Escourrou, Philipp Oettershagen, Juan Pedro Mendez Granado, Adrian Sanchez Menguiano, Jomela Meng, Siddhartha Verma, Kristen John, Ignacio Maqueda, Stephanie Coronel, Vicki Stolyar, Xin Ning, and Andy Galvin. My special thanks go to Terry Gdoutos, Landry Fokoua, and Monica Martinez Wilhelmus. Their friendship has always been, and will always be, a light in my life.

It is a pleasure to extend my gratitude to my professors at University of Washington for their continual support and encouragement beyond my graduation and throughout my years at Caltech. Professor Robert Breidenthal, Professor Mitsuru Kurosaka, Professor Dana Dabiri, and Professor Nathan Kutz, your continued presence has been a bridge between life in Seattle and Los Angeles.

From across the Pacific Ocean, my friends have always been the true source of my confidence, happiness, and motivation. I am forever indebted to Mizuho Todate, who has constantly sent her love in the form of messages, flowers, and often herself, flying here to see me. My loving thanks also go to Saeko Kuwasaki for her warm support that I have always been able to turn to. I'm deeply grateful to my family for their unconditional and undivided love and understanding. Thank you.

This work has been supported in part by the National Science Foundation under grant CBET-1235605.

Abstract

Studies in turbulence often focus on two flow conditions, both of which occur frequently in real-world flows and are sought-after for their value in advancing turbulence theory. These are the high Reynolds number regime and the effect of wall surface roughness. In this dissertation, a Large-Eddy Simulation (LES) recreates both conditions over a wide range of Reynolds numbers $Re_\tau = \mathcal{O}(10^2) - \mathcal{O}(10^8)$ and accounts for roughness by locally modeling the statistical effects of near-wall anisotropic fine scales in a thin layer immediately above the rough surface. A subgrid, roughness-corrected wall model is introduced to dynamically transmit this modeled information from the wall to the outer LES, which uses a stretched-vortex subgrid-scale model operating in the bulk of the flow. Of primary interest is the Reynolds number and roughness dependence of these flows in terms of first and second order statistics. The LES is first applied to a fully turbulent uniformly-smooth/rough channel flow to capture the flow dynamics over smooth, transitionally rough and fully rough regimes. Results include a Moody-like diagram for the wall averaged friction factor, believed to be the first of its kind obtained from LES. Confirmation is found for experimentally observed logarithmic behavior in the normalized stream-wise turbulent intensities. Tight logarithmic collapse, scaled on the wall friction velocity, is found for smooth-wall flows when $Re_\tau \geq \mathcal{O}(10^6)$ and in fully rough cases. Since the wall model operates locally and dynamically, the framework is used to investigate non-uniform roughness distribution cases in a channel, where the flow adjustments to sudden surface changes are investigated. Recovery of mean quantities and turbulent statistics after transitions are discussed qualitatively and quantitatively at various roughness and Reynolds number levels. The internal boundary layer, which is defined as the border between the flow affected by the new surface condition and the unaffected part, is computed, and a collapse of the profiles on a length scale containing the logarithm of friction Reynolds number is presented. Finally, we turn to the possibility of expanding the present framework to accommodate more general geometries. As a first step, the whole LES framework is modified for use in the curvilinear geometry of a fully-developed turbulent pipe flow, with implementation carried out in a spectral element solver capable of handling complex wall profiles. The friction factors have shown favorable agreement with the superpipe data, and the LES estimates of the Kármán constant and additive constant of the log-law closely match values obtained from experiment.

Contents

List of Figures

Chapter 1

Introduction and Background

1.1 Dissertation Overview

Two conditions that are abundant in environmental and engineering fluid flows are those bounded by solid walls with surface roughness and flows exhibiting high Reynolds number turbulence [52, 68]. Both the study of turbulence and the study of roughness in fluid dynamics trace back over a century and their widespread application has kept their respective fields under continual advancement [81]. One of the most revealing research thrusts of late comes from efforts seeking to achieve ever higher Reynolds number, and in doing so, shedding light on some of the longstanding questions about the very nature of turbulence, including how rigorously our present models match its incredibly complex motion [68] and – relevant to the present work – how surface roughness may alter turbulent flow dynamics at high Reynolds number [71, 52]. Naval, aerospace, and industrial communities have long maintained a vested interest in roughness due to its effect on drag and heat transfer and it remains an essential component to meteorological prediction [31, 109, 7].

Recent evidence points to situations in practice where high Reynolds number regimes are significantly affected by the presence of roughness, even when wall surfaces are manufactured such that they are considered highly smooth. Roughness in these cases becomes inseparable from the analysis and inextricably connected to explaining flow phenomena. Consequently, the involvement of advanced numerical simulation techniques that solve very high Reynolds number flows requires taking into account surface roughness also. The present work is concerned with a class of numerical strategies known as large-eddy simulation (LES) that is capable of creating such very high Reynolds number environments, and therefore the correct modeling of roughness effects in LES is of primary focus in this work.

The body of discourse for this dissertation begins with background material on turbulence theory, high Reynolds number experiments, roughness effects, and computational advances in the field, which is then followed by three main chapters. The first chapter introduces a novel roughness modeling technique in LES using a grid that is based on a regular Cartesian coordinate system. This model for roughness resides in a framework comprising a stretched vortex subgrid scale model (SGS) and a wall model [19]. The spatially periodic flow through both

smooth- and rough-wall channels is simulated and the results are compared. The second chapter turns to exploring the dynamical behavior of flows encountering abrupt changes in surface roughness at very high Reynolds numbers. Both the first and second chapters are based on a finite difference-and-spectral-method Navier-Stokes solver. The third and final chapter embeds the stretched vortex SGS model and wall model in a pipe flow geometry and extends them to fit with curved-wall boundary conditions. Rather than a finite difference solver, on this occasion a spectral element solver platform drives the wall-modeled LES implementation, and, while it accommodates pipe flow geometries in this case, it has the capability of handling complex boundary shapes beyond those of the canonical flows, thus setting the stage for future work.

1.2 Background

Introductory background material begins with a discussion of the Navier-Stokes equations, followed by an overview of smooth-wall turbulence theory, including the merits of canonical flow research and especially at high Reynolds number. This continues with a discussion of surface roughness both from theoretical and experimental perspectives, and concludes with a brief survey of some computational studies in turbulence. Here, the computational discussion focuses on two classes of solvers: direct numerical simulation (DNS) and large-eddy simulation (LES). Since LES was originally pioneered by Smagorinsky [121] and Deardorff [26] specifically for flow away from walls, contemporary computational approaches have required additional treatment near walls – predominantly of wall-modeled or wall-resolved types – which are introduced.

1.2.1 Navier-Stokes Equations and Filtering Processes for LES

The governing equations for incompressible Newtonian flows are given by a set of partial differential equations that describe the continuity and momentum balance within the field; these are known as the Navier-Stokes equations:

$$\rho\frac{\partial u_i}{\partial t} + \rho u_i\frac{\partial u_j}{\partial x_i} = -\frac{\partial p}{\partial x_i} + \mu\frac{\partial^2 u_i}{\partial x_j \partial x_j}, \tag{1.1}$$

$$\frac{\partial u_i}{\partial x_i} = 0. \tag{1.2}$$

where p and μ are pressure and viscosity respectively. We typically define kinematic viscosity as $\nu = \mu/\rho$.

Real turbulent velocity fields satisfy the Navier-Stokes equations well under the incompressible assumption when their Mach number $M \ll 1$. A turbulent velocity field is characterized by a spectrum of rotational eddy motions at various scales. As further discussed in later chapters, the main idea of large-eddy simulation (LES) is to solve dynamical equations for turbulent "eddy" scales that are greater than a cutoff defined by some measure of the local grid size. The effect of the finer, unresolved scales on the resolved scales is represented with statistical information com-

puted under some subgrid-scale model. The filtering process can be either implicit or explicit, where some of the common explicit filters are the box filter, Gaussion filter, and sharp spectral filter [103]. Presently, we perform implicit filtering, with the only filtering parameter being the cutoff length associated with the local grid-scale, Δ_c and therefore, the filtered quantity $\widetilde{\phi}$ is given by the convolution,

$$\widetilde{\phi}(x_i) = \int G(x_i - x_i'; \Delta_c)\phi(x_i')dx'. \tag{1.3}$$

Regardless of the choice of the filter, the full-scale velocity $u_i(t)$ is decomposed into the resolved-scale velocity $\widetilde{u}_i(t)$ and fluctuating velocity $u_i'(t)$, i.e. $u_i(t) = \widetilde{u}_i(t) + u_i'(t)$. Accordingly, the governing equations in Equation (1.1) and (1.2) can be re-cast in terms of filtered quantities as well as the modeled stresses as shown in Equations (1.4)-(1.7).

$$\frac{\partial \widetilde{u}_i}{\partial t} + \widetilde{u}_i \frac{\partial \widetilde{u}_j}{\partial x_i} = -\frac{1}{\rho}\frac{\partial \widetilde{p}}{\partial x_i} + \nu \frac{\partial^2 \widetilde{u}_i}{\partial x_j \partial x_j} - \frac{\partial T_{ij}}{\partial x_j}, \tag{1.4}$$

$$T_{ij} = \widetilde{u_i u_j} + \widetilde{u}_i \widetilde{u}_j \tag{1.5}$$

$$= \widetilde{\widetilde{u}_i \widetilde{u}_j} + \widetilde{\widetilde{u}_i \widetilde{u}_j} + \widetilde{\widetilde{u}_i u_j'} + \widetilde{u_i' \widetilde{u}_j} + \widetilde{u_i' u_j'}, \tag{1.6}$$

$$\frac{\partial \widetilde{u}_i}{\partial x_i} = 0. \tag{1.7}$$

These modeled stresses are called subgrid stresses and denoted as T_{ij} in tensor form. We presently use the stretched vortex model as introduced in Chapter 2.

1.2.2 Canonical Wall-Bounded Flow

Turbulent flows past smooth wall boundaries have considerable complexity, even in canonical geometries like the zero-pressure-gradient flat-plate turbulent boundary layer (ZPGFPTBL), pipe flow, and channel flow. These three flows are considered "canonical" because their analysis is greatly eased by having a simple wall geometry, and hence they have been favored by theoretical researchers seeking to solve manageable portions of the larger unsolved problem of turbulence. Indeed, there is a great likeness between the relations governing the mean velocities and turbulent statistics among canonical flows (described below in Section 1.2.3).

Each canonical flow provides an investigator with distinct advantages over the other two. Channel flows, for instance, have two periodic directions that make spectral-type numerical methods doubly effective. They also lend themselves to regular Cartesian coordinates, avoiding mathematical issues such as axis singularities found in cylindrical coordinates for pipes. Channels share an advantageous property with pipe flow: given sufficient stream-wise extent, the flow becomes statistically independent of downstream location. From an implementation point of view, pipe geometry adds one extra advantage in having periodicity along the azimuthal direction, while a channel and ZPGFPTBL require that their infinite span-wise domains be approximated.

1.2.3 Turbulence Structure and Scaling Over a Smooth Wall

In order that we appreciate the effect of wall roughness in context, a brief review of classical wall-bounded turbulent scaling and structure is helpful for the case of a smooth wall. We refer the reader to Clauser [21] and Coles & Hirst [24] for full and comprehensive reviews on this topic. Here we provide basic scaling and flow structure details relevant to roughness modeling in canonical environments.

Inner and Outer Scales

It was Prandtl who introduced the concept of a viscous boundary layer and an inviscid region of flow outside of this. The idea has remained unchanged up to the present, and hence a classical turbulent boundary layer will typically be presented as being composed of two principal regions that follow distinct scalings; in contemporary nomenclature, there is said to be a near-wall region where viscous effects are important and an outer region where they are not. Pipe and channel flows scale in the same manner, although it has been suggested in Marusic *et al.* [68] that small differences may exist.

In the near wall region, scaling quantities can be obtained by a number of approaches, including basic dimensional analysis. Here, based on the mean momentum equation, we take the velocity and length scales in the near-wall region to be $u_\tau = \sqrt{\overline{\tau_w}/\rho}$ and ν/u_τ respectively, where $\overline{\tau_w}$ is the total wall stress, ρ is the fluid density, and ν is the kinematic viscosity. Quantities normalized by these wall units are henceforth identified by a $^+$ superscript. Prandtl postulated that the mean stream-wise velocity near the wall is independent of δ, where δ is the boundary layer thickness, which leads to the famed "law of the wall." Written non-dimensionally, it becomes

$$U^+ = F(y^+), \tag{1.8}$$

where F is a universal function [115]. On the other hand in the outer region, it is assumed that the appropriate length scale δ is related to the boundary layer thickness while the friction velocity u_τ remains relevant, since u_τ sets up the boundary condition for the outer flow [68]. For channel and pipe flows, δ becomes the channel half-height and pipe diameter respectively. Based on outer scaling, von Kármán formulated the "velocity-defect law" in 1930 as

$$U_e^+ - U^+ = G(\eta), \tag{1.9}$$

where $\eta = y/\delta$ and the velocity at the outer edge of the boundary layer, U_e, is normalized to $U_e^+ = U_e/u_\tau$. Townsend regarded u_τ as a "slip" velocity condition felt by the outer flow [131]. Hence, u_τ becomes a global velocity scale and we can define a new "friction" Reynolds number, $Re_\tau = \frac{u_\tau \delta}{\nu}$, or when written in wall unit notation, as δ^+ for boundary layers. The friction Reynolds number Re_τ defines the scale separation between inner and outer length scales [52].

Near-Wall Flow Structure

Within the near-wall region, two layers can be distinguished by the differences in their mean velocity profiles: a viscous sub-layer below $y^+ \approx 5$, and a buffer layer between $10 \leq y^+ \leq 100$, approximately. Below $y^+ \approx 5$, fluid viscosity is dominant and the inner scaled mean velocity resembles a linear profile $U^+ = y^+$ for a smooth wall. Above this, the buffer region marks where the gradual transition occurs between the viscosity-dominated and the turbulence-dominated parts of the flow. It is this buffer region in which the flow is most active, being involved in a nonlinear self-sustaining cycle known as the "near wall cycle" [53]. Hamilton *et al.* [40] and Jiménez & Pinelli [54] have studied the mechanics of the buffer layer, finding that this is where most of the turbulent energy is generated for moderate Reynolds number flow.

Above the buffer layer is the outer layer, but at high enough Reynolds number (δ^+), an overlap layer develops between the two wherein any wall distance scaled in wall units, y^+, lies beyond the dominant viscous region, yet y/δ is too small for δ to have an influence. Thus the only remaining length scale is y itself. Millikan [77] proposed – by matching the velocity profiles in the law of the wall (Equation (1.8)) and the velocity-defect law (Equation (1.9)) – that a logarithmic velocity distribution results in the overlap region ($\nu/u_\tau \ll y \ll \Delta$) at sufficiently high Reynolds number.

$$U^+ = \frac{1}{\kappa}\log(y^+) + B, \tag{1.10}$$

where κ is the von Kármán constant. In classical turbulence theory, the value of κ is thought to be universal and often cited as having a value between 0.37 and 0.42 [68]. Equation (1.10) is valid for $y^+ \gg 1$ and has an upper limit at $y/\delta \approx 0.15$ [52]. The constant B should allow the profile to satisfy the no-slip boundary condition and is affected by the viscous sub-layer and buffer layer. In a way, it may be interpreted as measuring the influence of the viscous sub-layer on the flow. Outer-layer dynamics between the log-law and the inviscid free stream can be incorporated by including the Coles wake function $\mathcal{W}(y/\delta)$ [23] as

$$\Delta U^+ = \frac{1}{\kappa}\log(y^+) + B + \frac{\Pi}{\kappa}\mathcal{W}(y/\delta). \tag{1.11}$$

For its form, $\mathcal{W}(y/\delta)$ depends on the external flow outside of the boundary layer and the convention is to have $\mathcal{W}(0) = 0$ and $\mathcal{W}(1) = 2$. The non-dimensional Coles wake factor Π is flow dependent and for the channel flow considered here, where there is no outer region like that of a boundary layer, the wake term in Equation (1.11) has a small contribution.

1.2.4 High Reynolds Number

As previously stated, studies at ever higher Reynolds numbers are sought out as a way to address longstanding questions about the character of turbulent flow and to settle some important contemporary questions about accepted models of the mean and statistical behaviors of the flow

motions. Recurring questions in the community include whether the correct mathematical expression is being utilized to describe the mean stream-wise velocity profile – is it a logarithm or a weak power law? (Barrenblatt [9]; Marusic *et al.* [69]) – whether the Kármán constant is indeed universally constant among canonical flows (Marusic *et al.* [68]), how best to obtain a fluid's frictional force at the wall, and which scaling factor might collapse the various statistical moments describing fluid velocities and fluctuations (McKeon & Morrison [72]; Marusic *et al.* [68, 69]). The answers to these sometimes subtle questions have far-reaching implications concerning our ability to understand and accurately control or predict flow in turbulent environments.

One of the most recent studies that addresses these aforementioned questions about the nature of turbulence is Marusic *et al.* [69]. They observe two universal logarithmic scalings, one in mean velocity and the other in stream-wise turbulent intensity. Only when the friction Reynolds number reaches a certain threshold is the logarithmic behavior noted over a full decade of wall normal heights y^+. Consequently, they have set a Reynolds number standard, $Re_\tau > 40,000$, for acquiring enough data to discern logarithmic scaling. To do so, they note that in the inertial region of their data, from $3Re_\tau^{1/2}$ up to $0.15Re_\tau$, turbulent intensities fit well with a logarithmic profile having a slope given by the Townsend-Perry constant $A_1 = 1.26$. The inertial region is thought to begin at approximately $3Re_\tau^{1/2}$ because Klewicki *et al.* [58] have shown that the mean viscous force loses leading order influence above $2.6Re_\tau^{1/2}$. Also, the outer region of the inertial layer has been noted in Pope [103] to end at $y/\delta \approx 0.1$. Based on these ranges, if one seeks a decade or more of scaling data, one must select Re_τ such that it exceeds $40,000$.

Yet, what constitutes a "large" Reynolds number is still open to debate. Another definition might be that all important quantities have reached either their constant asymptotic state, or else are well approximated by a function that accurately describes their asymptotic state at arbitrarily large Reynolds numbers. This state of course, is expected to differ for smooth-wall and for rough-wall turbulence. For smooth-wall, canonical wall-bounded flows such as channel and pipe flow, and the ZPGTBL, Pullin *et al.* [106] suggest that a large Reynolds number means that $\log(Re_\tau) \gg 1$. By this definition of "large Reynolds number," smooth-wall bounded flows do not exist in practice. There are no actual or laboratory wall-bounded flows that satisfy this condition, nor are there likely to be any time soon. Further, any real-world attempt to establish incompressible, smooth-wall turbulent flows for which $\log(Re_\tau) \gg 1$ would encounter other important physics such as compressibility, the effects of the Earth's curvature, or perhaps most importantly, surface roughness. In this sense, the present work addresses moderate Reynolds numbers up to $Re_\tau = \mathcal{O}(10^8)$.

The turbulence community is continually pushing towards reaching ever-higher Reynolds numbers, although certain recurring limitations in our experimental and numerical proficiency fall short of being able to address the above mentioned questions with full rigor. At $Re_\tau > 40,000$, the fundamental experimental challenge is having instrumentation that can resolve the tiny eddy scales. Two choices are available. One can either a) attempt to create a very large facility to increase the characteristic length scale in the flow and make use of regular pitot or

hotwire measurements[127, 75] or b) use nano-scale probes [132] or perhaps highly controlled pitot tubes [8] in a relatively smaller facility. The highest known Reynolds number pipe flow experiments as of this writing have been carried out in the Superpipe facility at Princeton, reaching friction Reynolds numbers Re_τ of up to 0.3×10^6 [137, 71]. Hultmark *et al.* [44] have resolved over a decade of data to an exceptional degree of accuracy up to $Re_\tau = 98,190$ in this facility. The highest canonical flow tests ever conducted have been for thermally-neutral atmospheric boundary layers generated on the salt flats of Utah, SLTEST at $Re_\tau = 0.63 \times 10^6$ [76, 38]. This work does not specifically address geophysical flows viewed as rough surfaces and their unique character despite them typically having the high Reynolds number and rough wall characteristics relevant here (see Monin [80], Counihan [25], and Metzger & Klewicki [76]). We presently concern ourselves only with the incompressible canonical flows without reference to either transition from laminar to turbulent flow or thermal effects.

1.3 Roughness

As we look back into the history of experimental fluid dynamics, the early works of Hagen (1854) and Darcy (1857), who examined pressure losses in conduits, stand out as some of the first to demonstrate a key roughness phenomenon that led to the pervasiveness of smooth vs. rough wall studies since then. Their data shows how rough-walled pressure losses become independent of viscosity when the viscous length scale becomes small (i.e. high Reynolds number) in relation to the roughness length scale. Both Hagen and Darcy had yet to appreciate the significance of their finding, having made no attempt at a physical explanation at the time, but these Reynolds number independent fully rough flows would receive constant interest from that time onward.

Almost a century later, roughness was studied in a famous set of pipe flow experiments by Nikuradse [88], wherein he collected data over a Reynolds number range of many orders of magnitude. His mentor, Ludwig Prandtl [104], had developed a theoretical analysis for smooth wall turbulent flow in 1931 and subsequently used Nikuradse's data and that of others to establish the empirical constants in his relation for a smooth-wall friction factor,

$$\frac{1}{\sqrt{f}} = 2.0 \log_{10}\left(\sqrt{f} Re\right) - 0.8, \tag{1.12}$$

where f is the Darcy-Weisbach friction factor, hereafter referred to as "friction factor." Later, Theodore von Kármán [134] developed an expression of similar form to Prandtl's for the fully rough wall case, and hence independent of Reynolds number. From Schlichting [114], it is written as,

$$\frac{1}{\sqrt{f}} = 2.0 \log_{10}\left(d/k\right) + 1.74. \tag{1.13}$$

Evidently, a regime existed that bridged the gap between the smooth wall case (Equation (1.12)) and the fully rough wall case (Equation (1.13)) and it would come to be known as the transitional

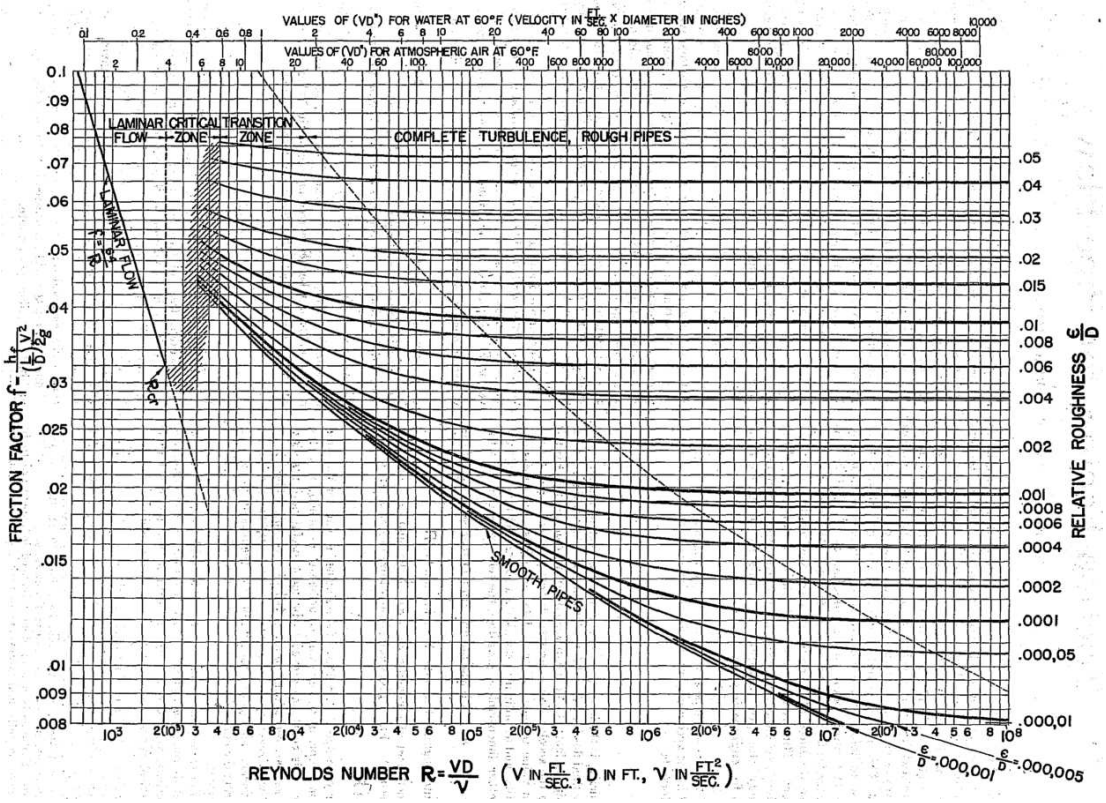

Figure 1.1: Moody Diagram - Darcy-Weisbach friction factor for pipe flow as a function of centerline Reynolds number R and relative roughness ϵ/D (Moody 1944 [82])

regime, though it bears no relation to the transition from laminar to turbulent flow. Colebrook [22] found an empirical formula by using the data of Nikuradse and others that fills the gap while still agreeing with the two extremes of smooth and fully rough. Moody [82] then used Colebrook's formula to generate the celebrated Moody diagram (Figure 1.1) that illustrates the dependence of the friction factor on both Reynolds number and relative roughness. This is a compelling visual of the four stages required to reach the "fully rough" limit as Reynolds number increases. Using current nomenclature, these are (in order) laminar flow, transition to turbulent flow over a smooth wall, transitionally rough flow, and finally the fully rough asymptotic limit. Here, "fully rough" means that the roughness height is small, $k/d \ll 1$, where k is some length-scale measure of surface roughness and d is some outer length scale, and the Reynolds number is sufficiently high.

Since the early studies of roughness, canonical flows have been extensively studied in the context of roughness, vastly broadening our knowledge of surface roughness effects. Among many, here we introduce two findings. First, at a sufficiently high Reynolds number, wall roughness effects emerge in experiments. Of notable example are the experimental studies in the Princeton Superpipe that are pushing their maximum Reynolds number above 35×10^5 [71, 68]. In this facility, McKeon *et al.*[71] have confirmed that above $Re = 20 \times 10^6$, roughness effects can be detected even using advanced honing of pipes to create smooth-wall conditions. Second, the inner layer experiences a complex effect from wall roughness, while the outer layer only experiences a

change in boundary condition, that, given enough scale separation, i.e. high Reynolds number, can be expressed as a roughness correction to friction velocity. This is known as Townsend's hypothesis of outer-layer similarity [131]. For smooth-wall flows, the velocity defect profile $U_0 - U$, where U_0 is some outer variable, is known to collapse on u_τ and outer length scale δ for sufficiently high Reynolds number, as derived from the law of the wall by Millikan [68]. Townsend's hypothesis then suggests that the same scalings should collapse this defect profile when roughness is introduced. Schultz & Flack [116] support Townsend's hypothesis through their experiments in rough-walled boundary layers up to $Re_\tau = 10,100$ while the experiments with two-dimensional roughness tend to suggest otherwise. For example, Krogstad & Antonia [59] conclude that the normal turbulent intensities and Reynolds shear stress hold evidence against it, explaining their observations in conjunction with a quadrant analysis in which they show increased strength and frequency of Q2 "ejection" and Q4 "sweep" events.

1.3.1 Roughness Types and Characterizations

A common choice for the roughness length scale k is to denote it as the root-mean-square (r.m.s.) height k_{rms} of the physical surface profile $k\,(x, z)$. Nikuradse developed another roughness length scale used commonly in later studies; he defined a parameter k_s to represent the sand grain size that he used to roughen pipe surfaces. Several popular empirical models such as those of Colebrook [22] and Cebeci & Bradshaw [17] that stem from Nikuradse's data sets make use of k_s as an input, making it necessary that non-sand-grain rough surfaces also have an equivalent k_s. Thus, when experiments or simulations use rough walls that are coated or bounded with anything other than single diameter sand grains, their roughness length scale is typically expressed as a "geometric" or "equivalent" sand roughness denoted $k_{s\infty}$. It is generally possible *a posteriori* to deduce $k_{s\infty}$ from a measured or simulated velocity profile by matching the value of their wall shear stress in the fully rough regime to that of Nikuradse [52]. Measuring $k_{s\infty}$ in practice, as it appears in Equation (1.14), requires the involvement of u_τ estimates, which must also come from measurement.

Skin friction can be straightforward to ascertain in the case of a smooth wall where one typically makes use of oil-film interferometry [86], direct drag force measurement with a force balance, Preston-tube [105, 42, 94], or the Clauser method [20, 21] to deduce the value of u_τ. Alternatively, in the case of internal canonical flows, we can measure the mean pressure gradient to deduce the skin friction for both smooth and rough walls. To directly measure the skin friction for rough surfaces, however, poses significant problems in measuring both u_τ and $k_{s\infty}$. Oil-film interferometry is highly accurate over smooth walls, often to with less than a percentage point accuracy [91, 92], but the method can be sensitive to temperature variation and is in any case incompatible with rough walls. Force balances like those used by Efros & Krogstad [27] for rough wall skin friction measurement are a trade off between the high accuracy afforded by direct measurement and their complexity to set up, which is perhaps why they are rare in the literature. Both the Preston and Clauser methods are simple, and give similar results to one

another over smooth walls, each relying on the assumption of a known universal scaling law. Uncertainties in the Clauser method may be large at times and can be as high as 20% [57]. Since the Clauser method on its own does not resolve u_τ and $k^+_{s\infty}$ in a rough wall flow yet can be modified to a form that does so and is both popular and equally simple, we describe the use of the modified Clauser method below [99]. Subsequently we touch on the connection between $k_{s\infty}$ and physical measures of roughness like the roughness peak height k_{max}, the r.m.s. height k_{rms}, and the distributional properties of roughness heights.

The Clauser method relies on the flow having a high enough Reynolds number to educe logarithmic behavior in the velocity profile, thus conforming to the log-law, which can be rearranged from Equation (1.10) to (1.14):

$$\frac{u(y)}{u_\infty} = \frac{u_\tau}{u_\infty}\frac{1}{\kappa}\log\left(\frac{yu_\infty}{\nu}\right) + \frac{u_\tau}{u_\infty}\frac{1}{\kappa}\log\left(\frac{u_\tau}{u_\infty}\right) + \frac{u_\tau}{u_\infty}B + \frac{u_\tau}{u_\infty}\frac{\Pi}{\kappa}W_c\left(\frac{y}{\delta}\right). \tag{1.14}$$

The unknown is u_τ/u_∞ for a smooth wall, so in selecting the correct u_τ/u_∞ such that measured smooth wall velocity data best matches the scaling in the log-law in a least squares sense, the skin friction can be approximated. Under rough wall scaling given by Equation (1.15), as Perry & Joubert [98] discuss, the number of unknowns jumps to three, these being $\Delta U/u_\tau$, u_τ/u_∞, and the error in origin.

$$\frac{u(y)}{u_\tau} = \frac{1}{\kappa}\log\left(y^+\right) + B - \Delta U^+ + \frac{\Pi}{\kappa}W_c\left(\frac{y'}{\delta}\right). \tag{1.15}$$

The error in origin is also known in the atmospheric sciences as zero plane displacement or in engineering as the offset in the virtual origin, which we denote d. Under the modified Clauser method given by Equation (1.16), one runs through an iterative procedure by modifying three unknowns, although this time they are u_τ and d, and the Coles wake parameter Π [61].

$$\frac{u(y)}{u_\infty} = 1+\frac{u_\tau}{u_\infty}\frac{1}{\kappa}\log\left(\frac{y'}{\delta^*}\right)+\frac{u_\tau}{u_\infty}\frac{1}{\kappa}\log\left(\frac{u_\tau}{u_\infty}\right)+\frac{u_\tau}{u_\infty}\frac{1}{\kappa}\left(\log\left(1+\Pi\right)-2\Pi-\log\left(\kappa\right)+\kappa W_c\left(\frac{y'}{\delta}\right)\right). \tag{1.16}$$

where $y' = y + d$ and the displacement thickness is denoted by δ^*:

$$\delta^* = \int_0^\delta 1 - \frac{u(y)}{u_\infty}dy. \tag{1.17}$$

When the iterative procedure converges, ΔU^+ is extracted from the relation in Equation (1.15) based on the converged estimates for the three unknowns and thereafter $k^+_{s\infty}$ is obtained from Equation (1.18) (See LeHew [61] for derivation),

$$k^+_{s\infty} = \exp\left(\kappa\left(\Delta U^+ + 8.5 - B\right)\right). \tag{1.18}$$

A systematic approach is therefore available from experimental or simulation data that estimates the equivalent sand grain roughness with reasonable accuracy. On the other hand, as

stressed in Schultz & Flack[116], to use only geometric properties of the surface height distribution to predict $k_{s\infty}$ *a priori* remains an open question, a problem both challenging and of significant importance.

An *a priori* generalized theory is elusive, but a number of empirical connections have been made in this regard that link one or two physical roughness measurements with $k_{s\infty}$. Simpson [120] has explored the relevance of roughness density in turbulent boundary layers. Schultz [117] has used multiple length scales by constructing nine pyramid-covered rough surfaces to seek the effect of element slope as well as element height. Slope has been found to hold no effect above a certain threshold, and they find in all cases a collapse in mean velocity, which exhibits smooth wall behavior upon plotting in velocity-defect form. Gioia & Chakraborty [35] have taken a theoretical approach to find an expression for friction factor that includes the general roughness size. Finally, Mejia-Alvarez & Christensen, in an effort to understand different scales associated with surface topology that may affect the turbulent boundary layer, have decomposed an irregular surface topology into a set of basis functions via singular value decomposition and have found that the effect of finer scale details of the surface is relevant within the roughness sublayer, but largely invisible in the outer layer.

Roughness element peak height, k_{max}, appears to have less bearing on $k_{s\infty}$ than does k_{rms}. LeHew [61], for example, observed that $k_{s\infty}$ measured in a rough-walled boundary layer with sparse roughness elements was half the height of element peaks k_{max}, though it was just 1.3 times larger than k_{rms}, potentially suggesting a stronger correlation with the latter. Since sparsity is known to affect wall shear stress, the observation makes sense if one considers the extra information carried in k_{rms} pertaining to nominal spacing between elements, information absent from k_{max}.

We digress briefly to note that much remains to be understood about sparsity and Jimenez [52] reviews the ongoing debates among the two major roughness types, known as k-type and d-type surfaces (see also Leonardi *et al.* [62]), which differ primarily in the spacing between elements. Only k-surfaces are considered in the present work since in d-type surfaces, $k_{s\infty}$ is found to be proportional not to physical roughness height but rather to boundary layer thickness.

Returning to empirical relationships, LeHew's result described above of $k_{s\infty} = 1.3k_{rms}$ differs from a result reached by Zagarola & Smits [137] of $k_{s\infty} = 3k_{rms}$ for Gaussian-distributed pipe roughness, potentially as a result of distributional skewness. Flack & Schultz [30] have identified surface geometry moments that are most relevant as scaling parameters, finding that the strongest correlation exists using skewness s_k and k_{rms} as expressed in the relation, $k_{s\infty} \approx 4.43k_{rms}(1 + s_k)^{1.37}$. Anderson & Meneveau [3] have provided an overview of other proposed empirical relationships and conclude that due to their variety, a simple relation with a universal constant and a single roughness scale is unlikely to be successful. Empirical relations provide needed insight, yet it is the uncertainty in their applicability for roughness element profiles outside of their source experiment that drives us toward a theoretical foundation.

1.3.2 Flow Response to Roughness

In Chapter 1.2 the scaling and structure of a turbulent flow bounded by smooth walls has been described, and a brief overview of its response to the presence of roughness is now provided. Our intuition tells us that flow is retarded more over a rough wall than a smooth one. It is known experimentally that this extra skin friction is accompanied by changes to the mean velocity profile, turbulence structure, and turbulent statistics [2]. There is, to date, continued debate as to the other aspects of the flow that are affected [68], especially concerning roughness topologies [62], but the present research will concentrate on the three mentioned explicitly above and we provide details below.

Mean Velocity

At the surface of a rough wall, elements of the surface generate additional pressure drag that is noticed as a momentum deficit in the mean velocity profile (Schultz & Flack[117]). There is a corresponding downward shift in the mean velocity profiles, and to that end Hama[39] modified the log-law to include a roughness function ΔU. Subsequent data sets have supported this additive shift (e.g. Shockling *et al.*[119]) but not the functional dependence of ΔU. It is well recognized that the height of roughness elements k^+ plays a dominant role in the canonical flows for determining the overall magnitude of ΔU (e.g. for boundary layers see Castro[16]), but not which specific surface shapes determine the exact form[68]. At present, the literature contains little extant work that comprehensively treats how roughness scales affect the nature of structural changes in the flow, when they begin, or whether the changes depend on the nature of the roughness[16]. However, there are certainly three distinct roughness regimes noted in this work which differ markedly from one another in terms of the flow behaviors and which we now define for use in the results to follow.

Roughness Height Regimes

Regime I: In the first regime, the flow behaves characteristically as if bounded by a smooth wall due to a low Reynolds number and/or simply very small roughness lengths. There is thus a dual dependence on both Reynolds number and roughness length scales, which can be consolidated into a "roughness Reynolds number" (simply the roughness height written in wall units, k^+) and we define the first regime as representing those flows with small k^+. Note that in flows with sufficiently small k^+, roughness is shown empirically to have no measurable effect on flow resistance [88, 15]. As k^+ grows larger, resistance does become detectable, although Bradshaw [15] highlighted the ongoing debate as to which exact k^+ represents the correct threshold for the onset of roughness effects, known as transition, and if such a threshold even exists. Nikuradse, for example, observed that for pipes with uniform graded-sand roughness, the flow initially behaves as if it were a smooth wall up until when a sudden transition is detected for $k^+_{s\infty} \geq 4$ [52]. On the other hand, when studying industrial pipe surfaces, Colebrook[22] found a more

gradual transition and consequently proposed that since multiple scales of roughness elements are present, they transition at different critical Reynolds numbers and the integrated effect is thus gradual.

A transition from smooth wall flow to one with measurable roughness effects hence defines the upper limit of the first regime. In the present work, we require that no precise upper limit definition of the first regime be set, imposing no exact threshold. Rather, we simply regard smooth-walled flow as the height k^+ smaller than that for which roughness effects are marked (in a comparable experiment) by a departure of the friction factor from Prandtl's hydraulically-smooth turbulent flow expression and an accompanying shift in the logarithmic layer belonging to the smooth wall.

Regime II: Typical roughness effects exist in the second regime due to sufficiently large roughness elements at the wall or high Reynolds number. Flow begins as transitionally rough and with increasing Reynolds numbers, fully rough flows are eventually expected. Most authors illustrate the nature of the second regime by plotting ΔU^+ against the single length scale k^+. Data for different surface shapes collapse in such a plot for both smooth-walled flow and fully rough flow but not during transition, indicating that k^+ alone is not sufficient to characterize the complexity of all rough surface shapes [52]. As k^+ grows further in the transitionally rough regime, roughness Reynolds number must usually exceed O(1) for viscous scales to become less relevant and thus for fully rough conditions to exist [124]. Roughness elements increase the drag but do not affect the outer layer structure, in accord with Townsend's hypothesis with exceptions noted by Krogstad *et al.* [59].

Structurally speaking, the characteristic smooth wall viscous sub-layer transforms into a roughness sub-layer that is $3 - 6k$ in height [31, 32]. Only above the roughness sub-layer does outer layer similarity still hold. The log-law region is, in most cases, affected by a shift downward in the additive constant B due to the increased wall drag. A few rough surfaces, like those designed by Bechert [10], exist that decrease drag and would cause a upward shift, though such specialized surfaces are not considered here.

Regime III: Finally, as the height of roughness elements k^+ grows to be extremely large, to a size more comparable with the height of near-wall viscous regions, the flow then differs from flows in the second regime on condition that rough elements exceed a threshold suggested by Jiménéz [52] of $k/\delta \approx 1/40$; their size is then large enough that they behave as discrete obstacles to the flow and destroy the near-wall viscous structures. Thus, $k/\delta \approx 1/40$ defines the threshold between the second and third regime. Where the roughness elements penetrate well into the log-law region within the third regime $k/\delta > 1/40$, the result is a breakdown of the similarity in the outer-layers [16]. Presently we do not consider roughness of this final regime, but only the smooth, transitional, and fully rough behavior of the first and second regimes.

Turbulent Statistics

For turbulence statistics, assuming a sufficient distance from the wall, single point measurements over rough and smooth walls, such as Reynolds stresses, and higher order statistics are expected to collapse in outer variables [116]. Studies by Raupach [109] and Kunkel [60] show support for this, while Krogstad *et al.* [59] and Leonardi *et al.*[63] have concluded otherwise. Although there is general literature consensus that the stream-wise Reynolds normal stress displays reasonable similarity in the outer flow, with the exception of a few studies [126], the Reynolds normal stress and Reynolds shear stress are often shown to increase due to surface roughness, as demonstrated by Krogstad *et al.* [59].

1.4 Computational Framework

In the area of computational fluid dynamics, large-eddy simulation (LES) has shown success in addressing the challenges of direct numerical simulation (DNS) associated with its high computational requirements. As the Reynolds number is increased, the range of eddy length scales existing in turbulent flows increases rapidly, requiring correspondingly higher resolutions for DNS. The required grid points for DNS scales roughly as $O(Re^{9/4})$, currently falling short of computing power at engineering Reynolds numbers. LES takes a different approach by resolving the larger scales while modeling the smaller scales. It generally involves four steps: filtering the velocities, and consequently obtaining the Navier-Stokes equations with the residual stress terms, obtaining closure in the equations by means of modeling, and finally solving the filtered Navier-Stokes equations [103]. While LES of unbounded homogeneous and shear turbulence is well established (e.g. Misra & Pullin[78], Ferrante *et al.*[29], Pitsch[102], Matheou *et al.*[70], and Foysi & Sarkar[33]), LES of wall bounded flows has remained challenging, first, because the existence of a wall causes the length scales to be progressively smaller towards the wall, and second, owing to near-wall anisotropy. For near-wall resolved LES, nearly 99% of grid points are used to resolve wall layers in channel flow [101] and therefore, the phenomena associated with wall bounded flows tend to bring the required computing resources up to $O(Re^{1.8})$, close to that of DNS [100]. However, the development of near-wall modeled LES [19, 46, 100, 101, 129, 130] has broadened the range of applications of LES for wall bounded flows. In near-wall modeled LES, the statistical effects of the near-wall anisotropic fine scales are not resolved but modeled via wall models that attempt to approximate near-wall physics.

Near-wall modeled LES is computationally more efficient than near-wall resolved LES because only the outer layer is computed, with the required grid size determined by the outer flow eddies [101]. Ideally, these approaches would use an outer layer grid that is Reynolds number independent, although a weak dependence such as $O(\log(Re))$ is also acceptable. Inoue & Pullin [46] summarize several empirical approaches to wall modeling. These have focused on modeling wall motions either empirically with the log-law, using the thin-boundary layer equations with damped-mixing length eddy-viscosity, or by matching the LES eddy-viscosity to that in the

Reynolds-averaged Navier-Stokes (RANS) equations. Other recent approaches include optimal-control theory methods [130] and those that consider the physics of near wall vortices, like the stretched spiral vortex model of Chung & Pullin [19]. For a given Reynolds number flow, all of these wall models boast a smaller number of grid points compared to near-wall resolved LES, making them faster to compute and hence more feasible as design tools.

Of interest in this research effort is the wall model of Chung & Pullin [19], which combines elements of equilibrium-stress models and zonal approaches (see classification of Piomelli [101]) but falls into neither category completely. Their approach extends the SGS model of Misra & Pullin [78] with a view to circumvent, as much as possible, the empiricism in RANS methods, while offering the advantage of using the stretched spiral vortex model in both wall model and outer LES [78]. The model is physical and only assumes near-wall vortices exist in a hierarchy of sizes that scale with their distance from the wall [87], so that all other results are derived from this. Hence it contains nothing further empirical except to match the location of intersection between the viscous-sublayer and log-layer. Being only weakly dependent on Reynolds number, this particular near-wall modeled LES has enabled simulation of wall-bounded flows up to at least $Re_\tau = 2 \times 10^6$ [46]. As such, the wall-model of Chung & Pullin is of great engineering interest, because it enables the simulation of a category of flows in the high Reynolds number regime.

When we combine our increased capability to simulate high Reynolds number turbulence by using wall-modeled LES with the aforementioned evidence of non-negligible surface roughness effects at high Reynolds number, the need for high Reynolds number LES to capture such roughness effects becomes clear. This has prompted the present dissertation work, to further wall modeled LES and, along with it, to furnish an appropriate roughness model. In our first stage of discourse, channel flow is the geometry of choice for examining homogeneously rough and smooth surfaces. The second stage examines the performance of the roughness model in a more dynamic manner by orienting strips of roughness transverse to the flow direction, thus creating repeated transitions of the flow from smooth-to-rough and rough-to-smooth. The analysis gains for us an understanding of flow responses to such transitions in various quantities, including the mean velocities, turbulent statistics, and internal boundary layer height growth rates. Finally, in lieu of simulating high Reynolds number turbulent flows in arbitrary geometry while correctly capturing surface roughness effects, the final stage of this work takes the first step towards such a goal by simulating flow in a pipe geometry using a methodology that avoids common pole singularity issues.

Chapter 2

Large-Eddy Simulation of Smooth-wall, Transitional and Fully Rough-wall Channel Flow

2.1 Introduction

The body of this dissertation begins henceforth with the development of a roughness model to be incorporated into wall modeled LES. As discussed in Chapter 1, we briefly reiterate that experimental evidence has incentivized us to consider roughness effects in our LES, which operates at very high Reynolds numbers. The roughness corrected LES methodology is applied to fully turbulent channel flow and the results are analyzed here to understand the Reynolds number and roughness dependence of the flow.

In the computational literature, studies of fully-resolved roughness dynamics have typically used direct techniques to understand flow near individual roughness elements as well as behaviors further from the wall. There have been several DNS studies of rough-wall turbulent channel flows [90, 63, 89, 32]. Orlandi *et al.* [90] have considered 2D- and 3D- roughness elements which are 20% of their half channel height and are fully characterized by grid points on the elements. Their flow visualizations provided insight into the complex flow structure near the roughness elements at Re_τ of a few hundred. Flores *et al.* [32] have taken a different approach to Orlandi *et al.*[90] by simulating rough channel flows at $Re_\tau = 630$, where they have replaced non-slip wall boundary conditions of a smooth wall with zero-mean velocity disturbances and interpreted such perturbed velocity boundary conditions as a roughness effect. Their one-point statistics and spectral analysis of the flow properties, including the mean velocity profiles, has confirmed Townsend's outer layer similarity hypothesis with an exception of the very large scales, which are known to correlate from the wall to the channel center. Additionally, they have examined flows over an individual disturbance, revealing the extent of the roughness sublayer to be about six times the roughness height, which is the equivalent of the buffer-layer of smooth-wall flows.

Only a few LES studies address surface roughness effects, e.g. Nakayama *et al.* [85] and Anderson & Meneveau [3]. The former have compared post-filtered DNS with LES when both

are performed on the same rough-wall geometry. Their results have suggested that unresolved LES subgrid roughness can be accounted for with additional terms in the filtered momentum equations. An associated consequence is added computational cost to evaluate the extra terms at every grid point. This differs from our approach wherein the direct roughness effect is applied only in the wall model, or equivalently only within a half to one percent of the half channel height at the present resolution, while the rest of the flow responds to the rough surfaces through the coupling between the outer LES and the wall model.

Anderson & Meneveau [3] have performed LES of open channel flow as a model of the atmospheric surface layer with multi-scaled surface roughness in the fully rough regime, mimicking naturally rough terrain. They search for a length scale parameter α such that the SGS roughness height, $z_{0,\Delta}$ is proportional to the local root-mean-square of the unresolved part of height fluctuations, σ, by $z_{0,\Delta} = \alpha\sigma$. An appropriate value of α is found by requiring resolution-independence for the total drag force. Once the value of α is determined, it is used to calculate the unresolved SGS part of the stress boundary conditions for the LES, which is then combined with the resolved part of the stress boundary conditions. A scale-dependent Lagrangian dynamic model is implemented, where the Smagorinsky constant is calculated dynamically. In contrast to the traditional dynamic models, this model exhibits improved performance when applied to high-Reynolds number wall-bounded flows without refining the mesh near the walls. We note that since they tailor their simulations for geophysical flows over natural terrain, they maintain interest only in the fully rough regime and neglect the viscous stress in the Navier-Stokes equations. On the other hand, our present interest extends to the capturing of the transitionally rough regime as well. This work also contrasts with Anderson & Meneveau in that the viscosity or equivalently Reynolds number is fully quantified.

In the present work, the roughness function ΔU^+ is incorporated directly into the wall model [19] without altering the SGS model [78], reflecting physically how the roughness is essentially viewed as an additional force that modifies the wall boundary condition on the outer flow. In particular, channel flows with subgrid roughness are simulated in the fully developed turbulent regime. With a choice of the Colebrook formula for the roughness function, we capture the flow in both transitionally and fully rough regimes in terms of the friction factors, mean velocity profiles, turbulent statistics, and dissipations. From here on we will first present a summary of the derivation of the stretched vortex model and the wall model [78, 19, 46] in §2.2, followed by the extension of this approach to surface roughness in §2.2.4. Subsequent sections describe some results of the LES, followed by a summary in §2.9.

2.2 SGS model and wall model with roughness

The implementation of the LES for a rough channel comprises two major parts: the stretched vortex SGS model and the wall model. The former is unaffected by the introduction of roughness, whereas the latter needs to be modified to incorporate the roughness model. In this section,

an overview of the SGS model is laid out, followed by the extension of the wall model [19] to include surface roughness. At this point, the roughness-corrected wall model is developed with a generic form of roughness correction. We then proceed to discuss the selection of the specific form of roughness function from numerous roughness functions available for other flows and applications.

2.2.1 Stretched vortex SGS model

The stretched-vortex approach is a structural SGS model designed to represent the statistical effect of subgrid motion by using information from resolved scale quantities [78]. It is assumed that the subgrid vorticity in each cell comprises a superposition of stretched vortices, each unidirectional and of "cylindrical" type. Upon coordinate transformation from the vortex-fixed frame to the lab-fixed frame, the distribution of orientations of the vortex structures forms a probability density function (PDF) which reflects the local anisotropy of the turbulence [107]. Extending the assumption that the ensemble dynamics of subgrid scale motion are dominated by a vortex aligned with a unit vector e^v, modeled via a delta-function PDF, the subgrid stress tensor is given by [107, 19]

$$T_{ij} = \left(\delta_{ij} - e_i^v e_j^v\right) K. \tag{2.1}$$

Here in Equation (2.1), the subgrid stress tensor, $T_{ij} = \widetilde{u_i u_j} - \widetilde{u}_i \widetilde{u}_j$ is expressed in terms of the unit vector, e^v, and the subgrid kinetic energy K, which is given by the integral of the subgrid stress energy spectrum $E(k)$ as

$$K = \int_{k_c}^{\infty} E(k) dk, \tag{2.2}$$

where $k_c = \pi/\Delta_c$ is the cutoff wave number and $\Delta_c = (\Delta_x \Delta_y \Delta_z)^{1/3}$. In what follows, the derivation of (2.1) is reviewed in some detail.

For subgrid stress closure, the subgrid kinetic energy K must be obtained as in Equation (2.2). The energy spectrum for turbulent incompressible flow $E(k)$, an essential part of calculating the subgrid kinetic energy, is known to have the asymptotic solution of the form (2.3) below for large wave number k, where ϵ is the dissipation rate per unit mass and η is the Kolmogorov length. This relation was initially obtained by using dimensional reasoning by Kolmogorov, and later derived from the Navier Stokes equations by Lundgren [64] in the form of Equation (2.4) for stretched spiral type vortices, where $\overline{a} = e_i^v e_j^v S_{ij}$ is the stretching along the subgrid vortex axis exerted by the resolved scales, and S_{ij} is the resolved strain-rate tensor.

$$E(k) = \epsilon^{2/3} k^{-5/3} F(\eta k). \tag{2.3}$$

$$= \mathcal{K}_0 \epsilon^{2/3} k^{-5/3} \exp\left(-\frac{2k^2\nu}{3|\overline{a}|}\right), \tag{2.4}$$

Upon integration of Equation (2.4) in accordance to Equation (2.2), the subgrid kinetic energy is

obtained as Equation (2.5) in terms of a group constant $\mathcal{K}_0'$ and an incomplete gamma function.

$$K = \frac{1}{2}\mathcal{K}_0'\Gamma[-\frac{1}{3}, \kappa_c^2], \text{ where } \Gamma[s,t] = \int_t^\infty u^{s-1}\exp(-u)du. \tag{2.5}$$

Here, $\mathcal{K}_0' = \mathcal{K}_0\epsilon^{2/3}\lambda_v^{2/3}$, $\lambda_v = (2\nu/3|\overline{a}|)^{1/2}$, and $\kappa_c = k_c\lambda_v$. The approximation of $\Gamma[s,t]$ and the evaluation of $\mathcal{K}_0'$ are given in Chung & Pullin[19].

2.2.2 Wall Model with Roughness: Friction Velocity

The challenge in the LES of wall bounded flows is that the turbulent length scales become progressively smaller towards the wall due to confinement of the near-wall eddies. In near-wall resolved LES, this is addressed by introducing a non-uniform mesh that has higher mesh refinement near the wall, and thus capturing the effect of near-wall fine scales. In wall-modeled LES, the near-wall anisotropic fine scales are modeled via a wall model, thus eliminating the need for higher grid refinement. At the interface between the wall model and outer flow region, i.e. at a lifted virtual wall, Chung & Pullin [19] define a slip velocity, thus providing the outer LES with slip Dirichlet boundary conditions. Here, roughness effects are included while retaining two major features, first solving an ODE to obtain the friction velocity and subsequently evaluating the slip velocity utilizing Townsend's attached-eddy hypothesis. We have denoted x, y, and z as stream-wise, wall-normal, and span-wise coordinates, respectively, and u, v, and w are the corresponding velocity components. The wall-parallel filtering and wall-normal integration operators are defined by

$$\widetilde{\phi}(x,y,z,t) = \int\int \phi(x',y,z',t)\, G(x-x';\Delta_f)\, G(z-z';\Delta_f)\, dx'dz', \tag{2.6}$$

$$\langle\widetilde{\phi}\rangle(x,z) = \frac{1}{h-k(x,z)}\int_{k(x,z)}^{h} \widetilde{\phi}(x,y,z)\, dy, \tag{2.7}$$

where $\widetilde{\phi}$ denotes wall-parallel filtering and $\langle\phi\rangle$ denotes a wall-normal average.

We proceed to give a heuristic derivation of the ODE for the friction velocity u_τ in the rough-wall flow. Let the wall shape be $y = k(x,z)$ with $\overline{k(x,z)} = 0$ and define $f(x,z) = k(x,z) - y$. Here, we denote $\overline{(\ )}$ as the average over the wall-parallel plane. The outward wall-normal (into the wall) is $\mathbf{n} = \nabla f/|\nabla f|$ on $f = 0$. We consider a local control volume at the channel wall with x, z dimensions Δx, Δz (the local grid size), and y-dimension an arbitrary thickness h. It is further assumed that Δx, Δz and h are all much larger than $max|k(x,z)|$. The four wall-normal surfaces intersect the wall and the bottom surface is the wall itself. Applying top-hat filtering and averaging as defined above to the momentum equations, we obtain an integral form of the stream-wise momentum equation over the control volume

$$\frac{\partial}{\partial t}\iiint \mathbf{u}dV = -\oiint \mathbf{n}.\left(\mathbf{u}\,\mathbf{u} + \frac{p}{\rho}\mathbf{I} - \frac{\boldsymbol{\tau}}{\rho}\right) dS, \tag{2.8}$$

where $\boldsymbol{\tau} = 2\nu\mathbf{S}$ and $\mathbf{S}$ is the strain-rate tensor. The RHS of Equation (2.8) essentially represents the flux of momentum through the planes defining the control volume, and exterior forces on the control volume consists of the convective, pressure, and viscous terms, with each contribution requiring special wall boundary treatment upon our inclusion of rough walls.

The pressure term evaluated at the rough wall is non-zero due to the variation of $\mathbf{n}$. Since the roughness geometry of interest is subgrid, this pressure contribution from the rough wall introduces an unknown term in the filtered-averaged momentum equation. A similar situation is found for the viscous contribution at the rough wall, which is also in the form of surface integral over an unknown surface geometry. Collecting all the flux contributions, including unknown terms, and approximating flux differences across wall-normal surfaces in terms of wall-parallel derivatives, the cell-averaged stream-wise momentum equation for the control volume is rewritten as

$$\frac{\partial\langle\widetilde{u}\rangle}{\partial t}+\frac{\partial\langle\widetilde{u}\widetilde{u}\rangle}{\partial x}+\frac{\partial\langle\widetilde{u}\widetilde{w}\rangle}{\partial z}+\frac{1}{h}\widetilde{uv}|_h = -\frac{\partial\widetilde{p}/\rho}{\partial x}\bigg|_h+\frac{\nu}{h}\frac{\partial\widetilde{u}}{\partial y}\bigg|_h-\frac{1}{h}\left[\frac{1}{\Delta x\,\Delta z}\iint\limits_w \frac{p}{\rho}\,n_x\,dS-\frac{\nu}{\Delta x\,\Delta z}\iint\limits_w \mathbf{n}.\nabla\mathbf{u}\,dS\right], \tag{2.9}$$

where n_x is the stream-wise component and the surface integral $\iint_w$ denotes the integral over the wall. The last two integral terms are the unknown pressure and viscous terms due to roughness. To encapsulate the wall skin friction contributions, we define the friction velocity u_τ as

$$u_\tau^2 = \frac{1}{\Delta x\,\Delta z}\iint\limits_w \frac{p}{\rho}\,n_x\,dS-\frac{\nu}{\Delta x\,\Delta z}\iint\limits_w \mathbf{n}.\nabla\mathbf{u}\,dS=\frac{1}{\rho}\overline{\tau_w}, \tag{2.10}$$

where $\overline{\tau_w}$ is the total surface drag force per unit area and $\overline{(\,)}$ refers to an average over the intersection of the control volume (cell) and the wall. The differential equation (2.9) becomes

$$\frac{\partial\langle\widetilde{u}\rangle}{\partial t}+\frac{\partial\langle\widetilde{u}\widetilde{u}\rangle}{\partial x}+\frac{\partial\langle\widetilde{u}\widetilde{w}\rangle}{\partial z}+\frac{1}{h}\widetilde{uv}|_h = -\frac{1}{\rho}\frac{\partial\widetilde{p}}{\partial x}\bigg|_h+\frac{\nu}{h}\frac{\partial\widetilde{u}}{\partial y}\bigg|_h-\frac{1}{h}u_\tau^2. \tag{2.11}$$

Equation (2.11) is identical to the smooth-wall case (see Chung & Pullin [19]), but contains a generalized definition of the friction velocity to account for the additional pressure drag and corrected viscous contributions to the total surface drag for rough walls. The smooth-wall case with the conventional definition of u_τ is recovered with $k(x,y)\equiv 0$ and $\mathbf{n}=(0,1,0)$.

2.2.3 Inner Scaling

The unsteady term of Equation (2.11) is treated with a general form of inner scaling. A classical but empirical roughness correction to inner scaling can be used to account for an increased momentum deficit due to the surface drag on the roughness elements, resulting in a downward shift of the inner-scaled mean velocity profile [117]. Such a downward shift is quantified via roughness function ΔU^+, which is incorporated in the inner scaling as

$$\widetilde{u}(x,y,z,t) = u_\tau(x,z,t)\left(F_1\left(y^+\right)-\Delta U^+\left(k_{s\infty}^+\right)\right), \tag{2.12}$$

where $y^+ = yu_\tau/\nu$ and $k_{s\infty}^+ = u_\tau k_{s\infty}/\nu$. The first term $F_1\left(y^+\right)$ is the common term for both smooth and rough walls, whilst $\Delta U^+\left(k_{s\infty}^+\right)$ is the roughness function expressed in terms of equivalent sand roughness, $k_{s\infty}$ and $k_{s\infty}^+ = k_{s\infty}u_\tau/\nu$. Applying the wall-normal average, and temporal derivative, we obtain the expression given by

$$\frac{\partial}{\partial t}\langle\tilde{u}\rangle = \frac{d}{dt}\left(\frac{u_\tau}{h}\int_0^h F_1\left(y^+\right) - \Delta U^+\left(k_{s\infty}^+\right)dy\right), \tag{2.13}$$

where the friction velocity is spatially and temporally variant, i.e. $u_\tau = u_\tau\left(x,z,t\right)$. In order to find an explicit expression for Equation (2.13), we differentiate Equation (2.12) with respect to u_τ and obtain

$$\frac{\partial\tilde{u}}{\partial u_\tau} = F_1(y^+) + y^+F_1'(y^+) - \Delta U^+\left(k_{s\infty}^+\right) - k_{s\infty}^+\Delta U'^+\left(k_{s\infty}^+\right) = \frac{d(y^+F)}{dy^+} - \frac{d(k_{s\infty}^+\Delta U^+)}{dk_{s\infty}^+}. \tag{2.14}$$

We then apply the wall-normal averaging defined in Equation (2.7) to arrive at

$$\frac{\partial\langle\tilde{u}\rangle}{\partial u_\tau} = \frac{u|_h}{u_\tau} - k_{s\infty}^+\frac{\partial\Delta U^+}{\partial k_{s\infty}^+}. \tag{2.15}$$

Therefore, Equation (2.13) can be re-expressed as

$$\frac{\partial}{\partial t}\langle\tilde{u}\rangle = \frac{\partial\langle\tilde{u}\rangle}{\partial u_\tau}\frac{\partial u_\tau}{\partial t} = \frac{\partial u_\tau}{\partial t}\left(\frac{\tilde{u}\,|_h}{u_\tau} - k_{s\infty}^+\frac{\partial\Delta U^+}{\partial k_{s\infty}^+}\right). \tag{2.16}$$

Equation (2.16) is an exact consequence of Equation (2.12) - (2.13) for arbitrary $F_1(y^+)$ and $\Delta U^+(k_{s\infty}^+)$. In particular we note that integrals of $F_1(y^+)$ do not appear in Equation (2.16) owing to cancellation.

Substitution of Equation (2.16) into the averaged-filtered momentum equation (2.11) and approximations of the filtered-averaged nonlinear terms as values at $y = h$ (one-point estimates), we obtain an ordinary differential equation (ODE) for u_τ as

$$\frac{du_\tau}{dt} = \frac{-\left.\frac{\partial\widetilde{uu}}{\partial x}\right|_h - \left.\frac{\partial\widetilde{uw}}{\partial z}\right|_h - \left.\frac{\partial\widetilde{P}}{\partial x}\right|_h - \frac{1}{h}\widetilde{uv}\,|_h + \frac{\nu}{h}\left.\frac{\partial\widetilde{u}}{\partial y}\right|_h - \frac{1}{h}u_\tau^2}{\frac{\widetilde{u}\,|_h}{u_\tau} - k_{s\infty}^+\frac{\partial\Delta U^+}{\partial k_{s\infty}^+}}. \tag{2.17}$$

The height h protrudes to a distance corresponding to the first or second grid cell of the LES domain and all filtered quantities on the right-hand side are provided by the LES itself. The presence of surface roughness is apparent in the denominator of Equation (2.17) in the form of the derivative of ΔU^+, which indicates that the roughness function is dependent on the inner-scaled roughness height and that the friction velocity is calculated dynamically at each wall point. Equation (2.17) allows local and dynamical calculation of u_τ. In practice, an equivalent differential equation for $\eta = u_\tau^2/\nu$ is solved numerically, and synchronized with the time steps occurring in the Navier-Stokes solver [19, 46]. While for the present channel flow, the wall-averaged u_τ can be calculated using an integrated pressure-gradient, wall-drag balance (es-

sentially an extension of the above argument to the whole channel), Equation (2.17) is more general and can be used for boundary layer flows in the presence of pressure gradient. Further formal extensions of Equation (2.17) to three-dimensional boundary layers in the presence of wall curvature are straightforward, as are the incorporation of more general roughness functions which are functions of several roughness scales $\Delta U^+(k_{s\infty}^{+(1)}, k_{s\infty}^{+(2)}, k_{s\infty}^{+(3)}, ...)$.

2.2.4 Wall Model with Roughness: Slip Velocity at a Lifted, Flat Virtual Wall

Chung & Pullin [19] have defined three near-wall regions: (I) $0 < y < h_\nu$, essentially the viscous sublayer and part of the buffer layer; (II) $h_\nu < y < h_0$, part of the overlap layer where the shear stress is approximately constant and is modeled by the stretched vortex SGS model consisting of attached vortices aligned with the stream-wise direction; (III) $h_0 < y$, where non-universal outer flow features are computed by LES coupled with the original stretched vortex SGS model of detached subgrid vortices aligned with the most extensive strain-rate direction. The lifted virtual wall refers to a plane at $y = h_0$, somewhere within the overlap region. In region (I), the velocity shows a linear profile, i.e. $\widetilde{u}^+ = y^+$ where $\widetilde{u}^+ = \widetilde{u}/u_\tau$ and $y^+ = yu_\tau/\nu$. We take h_ν^+ to be the intercept of the linear and empirical log-profile of the law of the wall, which is $h_\nu^+ \approx 11$ for a hydrodynamically smooth wall.

A summary of the derivation of the slip velocity is presented by Inoue & Pullin [46]. The derivation begins by assuming that the total shear stress is approximately constant [131] and that in the overlap region (region II) near-wall vortices are stream-wise aligned [41, 111]. Such conditions allow us to reduce the Reynolds shear stress expressed in Equation (2.1) to

$$T_{xy} = -\frac{1}{2}\gamma_{II} K^{1/2} \Delta_c \frac{d\widetilde{u}}{dz}. \tag{2.18}$$

Now, we further assume that the near-wall region can be modeled by a hierarchy of stream-wise aligned vortices whose scales are proportional to the wall distance [19]. Along with Equation (2.18), we arrive at

$$\frac{d\widetilde{u}}{dy} = \frac{1}{\mathcal{K}_1}\frac{u_\tau}{y}, \text{ where } \mathcal{K}_1 = -\frac{\gamma_{II} K^{1/2}}{2T_{xy}/u_\tau}. \tag{2.19}$$

The idea behind this model is called attached eddies as opposed to detached eddies, which exist in the outer part of the flow where the vortices are unaware of the wall [131, 97, 87]. Upon integration of Equation (2.19) and setting the constant of integration by requiring that the log-law intersects with the linear-relation near the wall at a particular distance from the wall, $y^+ = h_\nu^+$, a log-relation is obtained for the velocity in the overlap layer above smooth walls as

$$\widetilde{u} = u_\tau \left(\frac{1}{\mathcal{K}_1} \log\left(y^+\right) + B \right), \tag{2.20}$$

where $B = h_\nu^+ - \mathcal{K}_1^{-1} \log\left(h_\nu^+\right)$ [19]. The extension of this relation to rough surfaces is carried

out through the application of the roughness correction $\Delta U^+ \left(k_{s\infty}^+\right)$ to this relation. Thus, we obtain the velocity profile in the overlap layer above rough surfaces as

$$\widetilde{u} = u_\tau \left(\frac{1}{\mathcal{K}_1} \log\left(y^+\right) + B - \Delta U^+ \left(k_{s\infty}^+\right) \right). \tag{2.21}$$

We now assume that we can apply a slip-velocity boundary condition at a flat, lifted virtual wall at $h_0 > k(x,z)$. It is in this sense that the roughness is considered subgrid. The slip velocity is obtained using Equation (2.21) evaluated at $y = h_0$. Further, to simplify the expression for $\mathcal{K}_1$, we recall the assumption that the total shear stress is approximately constant in the overlap region, which allows for modeling the constant value of the total shear stress as the geometric average of its value at the true wall and at the virtual wall, hence, we obtain

$$\widetilde{u}\,|_{h_0} = u_\tau \left(\frac{1}{\mathcal{K}_1} \log\left(h_0^+\right) + B - \Delta U^+ \left(k_{s\infty}^+\right) \right) \text{ where } \mathcal{K}_1 = -\frac{\gamma_{II} K^{1/2}}{2\left(-T_{xy}\,|_{e_{\tilde{s}}}\right)}. \tag{2.22}$$

Chung & Pullin [19] estimate the vertical momentum mixing constant as $\gamma_{II} = 0.45$ by matching Townsend's structure parameter –a measure of the relative amount of shear stress to vortex kinetic energy– at the interface of region (I) and (II). Typically, the height of the virtual wall h_0 is determined as some fraction of the first grid size, and presently $h_0 = 0.18\Delta_y$ is used.

The use of the log-like relation in the wall model in Equation (2.22) could be interpreted as bias introduced in the LES that leads to a log-variation in the mean velocities. However, we point out a study on the influence of the inner-scaling laws on the LES results. Cheng & Samtaney have implemented LES with the stretched vortex model and wall model, using both the power-law and log-law for the wall model. They have shown that when a power-law wall model is used instead, a log-profile in LES is still obtained.

In summary, the near-wall SGS model, for subgrid roughness, is implemented as follows: for every cell adjacent to the walls, Equation (2.17) is solved for u_τ and hence the friction velocity is calculated dynamically. Then the log-relation in Equation (2.22) is used to obtain the slip velocity at the lifted virtual wall at $y = h_0$. These processes are coupled with the outer LES in two ways: first, some terms in the RHS of the ODE in Equation (2.17), as well as the shear stress $T_{xy}\,|_{e_{\tilde{s}}}$ necessary for evaluating $\mathcal{K}_1$, are supplied by the outer LES. The resultant slip velocity at the lifted virtual wall provides the LES with the Dirichlet boundary conditions. The roughness functions are left in the implicit form to accept any roughness type and empirical formula appropriate to the specific use of the model. The explicit form of roughness function in this work is discussed subsequently.

2.2.5 Wall-Normal Velocity Boundary Condition

We have thus far considered wall-parallel slip velocity to incorporate surface roughness effects, yet it is also possible to account for wall-normal velocity at the virtual wall with roughness taken

into consideration. The filtered continuity equation is given by

$$\frac{\partial \tilde{u}}{\partial x} + \frac{\partial \tilde{v}}{\partial y} + \frac{\partial \tilde{w}}{\partial z} = 0. \tag{2.23}$$

By integrating this continuity equation from the actual wall to the virtual wall height and assuming that the filtered span-wise velocity is zero, we obtain the vertical velocity at the virtual wall as

$$\widetilde{v} \mid_{h_0} = -h_0 \frac{\partial \langle \tilde{u} \rangle}{\partial x}. \tag{2.24}$$

Utilizing an inner-scaling argument, which is similar to how Equation (2.16) is obtained for the wall-parallel velocity boundary condition, leads to the expression for the wall-normal velocity boundary condition,

$$\widetilde{v} \mid_{h_0} = -h_0 \frac{\partial u_\tau}{\partial x} \left(\frac{\tilde{u} \mid_{h_0}}{u_\tau} - k_{s\infty}^{+} \frac{\partial \Delta U^{+}}{\partial k_{s\infty}^{+}} \right). \tag{2.25}$$

In the studies of Flores & Jiménez [32] and Orlandi *et al.* [89] where roughness effects are modeled by finite velocity perturbation at wall boundaries, the wall-normal velocity is observed to have influences on the flow. Flores & Jiménez have observed ΔU^{+} of 4.6 when the wall-normal velocity alone is forced using a disturbance magnitude of $v'^{+} = 0.72$ at the wall. In contrast, when the stream-wise velocity is disturbed in the same phase as the wall-normal velocity, the resultant velocity shift has been shown to nearly double. Here, the wall-normal velocity has been calculated passively in the simulation at each wall point to identify the relative magnitudes of the wall-normal velocity to wall-parallel slip velocity. It has been found that the wall-normal velocity is three to four orders of magnitude smaller than the wall-parallel slip velocity; thus, the vertical velocity at the virtual wall is omitted in our simulations.

2.2.6 Roughness Function

The explicit forms of roughness functions have been of interest in theoretical, experimental, and computational studies of wall bounded turbulent flows. The choice of roughness function should be determined by specific surface type and is considered an input to the present model. The forms of roughness functions are influenced by both universal roughness effects and potentially by the individual choice of roughness types according to their topographical profile. A comprehensive summary of roughness functions is presented by Jiménez [52]. Roughness is quantified in terms of equivalent sand roughness $k_{s\infty}$, and the well established Colebrook empirical formula in Equation (2.26) is used for the roughness function.

$$\Delta U^{+} \quad = \quad \kappa^{-1} \log\left(1 + 0.26 k_{s\infty}^{+}\right). \tag{2.26}$$

The equivalent sand roughness in wall units can be expressed in terms of the Reynolds number Re_τ and relative roughness ϵ.

$$k_{s\infty}^+ = \epsilon\, Re_\tau, \qquad \epsilon \equiv \frac{k_{s\infty}}{\delta}, \quad Re_\tau = \frac{u_\tau\, \delta}{\nu} \tag{2.27}$$

In the present implementation, the roughness is strictly subgrid and hence the level of roughness is characterized by $k_{s\infty}$ rather than alternatives, such as considering individual roughness element shapes, fluvial-type topography [3], or with systematic methods such as morphometry in urban landscapes [37, 65]. Accordingly, zero-plane displacement correction d is not germane since all surfaces have a $d = 0$ designation in our coordinate system [48].

When the Colebrook formula is incorporated into our wall model, the second term of the denominator in Equation (2.17) becomes

$$\begin{aligned} k_{s\infty}^+ \frac{\partial \Delta U^+}{\partial k_{s\infty}^+} &= \frac{1}{\mathcal{K}_1} \frac{0.26\, k_{s\infty}^+}{1 + 0.26\, k_{s\infty}^+}, \\ &= \frac{1}{\mathcal{K}_1} \frac{0.26\, \epsilon\, \delta\, u_\tau/\nu}{1 + 0.26\, \epsilon\, \delta\, u_\tau/\nu}. \end{aligned} \tag{2.28}$$

Here, the locally and dynamically determined value of friction velocity u_τ is obtained from the wall model. With the introduction of the Colebrook formula, the log-relation in Equation (2.22) takes the following form:

$$\widetilde{u}\,|_{h_0} = u_\tau \left(\frac{1}{\mathcal{K}_1} \log\left(h_0^+\right) + B - \frac{1}{\mathcal{K}_1} \log\left(1 + 0.26\, k_{s\infty}^+\right) \right). \tag{2.29}$$

We remark that the roughness-corrected model is semi-empirical in the sense that the roughness function is a model input supplied by experiment, theory, low Reynolds number DNS, or some other means. Further, the flow obeying Townsend's hypothesis may be interpreted as the inevitable consequence of the LES directly setting the slip velocity according to the empirical roughness function. However, such empiricism is applied to a thin layer immediately adjacent to the wall; the use of a roughness function is confined to the wall model only, which presently operates over $0.5 \sim 1\%$ of the half channel height δ, dependent on resolution. Additionally, the present model calculates the slip velocity using the friction velocity that is calculated locally and dynamically (see Equation (2.17)), and hence the slip velocity only partially relies on the empiricism. Finally, Townsend's hypothesis suggests that the wall surface information is transmitted from the wall to the bulk of the flow through the friction velocity. However, the current models operate via two-way coupling and hence the outer flow information also travels towards the wall; this nature is not included in the hypothesis.

2.2.7 LES Summary

We have addressed two important components of the current LES framework, the wall model and the stretched vortex SGS model. In short, in a typical time-step of the overall LES, the

following three stages are implemented:

1. The friction velocity u_τ is calculated by integration of Equation (2.17) locally and dynamically over the time-step. The input to the ODE is supplied by the outer LES.

2. With an updated u_τ now known at every point on the wall, a local slip velocity is calculated using Equation (2.29) and is supplied to the outer LES as the boundary conditions at the lifted virtual wall.

3. With the boundary condition at each grid point on the virtual wall now known, one time-step of the LES equations is then performed using the fractional step method described subsequently in §2.3, using the stretched-vortex SGS model described earlier to calculate subgrid stresses via Equation (2.1).

In terms of assumptions, inputs and interactions, we can summarize the framework as follows. The wall model assumes inner-scaling in calculating the friction velocity and slip velocity, given by Equation (2.17) and (2.29), respectively; it is in this way that the wall model is designed to be optimal for high Reynolds number flow, where such scaling is clearly identified. Operating on smooth walls, the model requires two empirical values: the log-linear profile intersect, h_ν^+ and virtual wall height, $h_0 = 0.18\Delta_y$. Upon inclusion of roughness, another measure of empiricism, Hama's roughness function is required; currently, we used the Colebrook formula, given in Equation (2.26). The other inputs to the wall model are supplied by the outer LES at the virtual wall.

The wall model supplies the boundary conditions for the outer LES via the slip velocity, which is the singular mechanism for the LES to know of the wall roughness conditions. In other words, the subgrid stresses, calculated by Equation (2.1), are entirely unmodified by the inclusion of roughness effects, but are responsible for correctly transmitting the wall roughness information towards the bulk of the flow as well as feeding back the bulk flow information to the wall model.

Using this framework, we aim to first improve the predictive capability of LES for rough-wall flows at large Reynolds number, and second to investigate the effects of roughness on the bulk of a turbulent flow including the outer region, while less focus is placed on the details in the near-wall region. As discussed in the remainder of this chapter and Chapter 3, the current roughness corrected model is robust when applied to channel flows with uniform and nonuniform roughness distributions at the wall. The application is not limited to channel flow, but can, in principle, be applied to other flows such that the roughness distribution can be space dependent as well as time dependent, so long as roughness elements are subgrid. Finally, the wall model with roughness is entirely local, and hence in principle can be incorporated into any LES or DNS code, for which arbitrary Dirichlet-like boundary conditions are admissible.

2.3 Numerical Methods

The incompressible Navier Stokes equations given in Equation (2.30) are solved numerically for a rough-wall channel of dimensions $L_x \times L_y \times L_z$ (stream-wise, wall-normal, and span-wise directions respectively).

$$\frac{\partial \mathbf{u}}{\partial t} + \mathbf{u} \cdot \nabla \mathbf{u} = -\nabla p + \frac{1}{Re}\nabla^2 \mathbf{u} - \nabla \cdot \mathbf{T} \tag{2.30}$$

$$\nabla \cdot \mathbf{u} = 0, \tag{2.31}$$

where bold-face denotes tensors. The velocity vector and pressure are denoted by $\mathbf{u}$ and p respectively. In the current implementation, we employ the skew-symmetric form of the non-linear terms since, despite its higher computational cost, it handles the aliasing errors well. As introduced in Perot [96], this set of equations can be discretized and set in matrix form,

$$\begin{bmatrix} \mathbf{A} & \mathbf{G} \\ \mathbf{D} & \mathbf{0} \end{bmatrix} \begin{bmatrix} \mathbf{u}^{n+1} \\ p^{n+1} \end{bmatrix} = \begin{bmatrix} \mathbf{r}^n \\ 0 \end{bmatrix} + \begin{bmatrix} bc_1 \\ bc_2 \end{bmatrix}, \tag{2.32}$$

where the current time step is denoted by n. The operators $\mathbf{A}$, $\mathbf{D}$, and $\mathbf{G}$ are respectively the advection-diffusion, divergence, and gradient operators. Denoted by $\mathbf{r}^n$ is the explicit term on the right-hand-side of the momentum equations. The specific forms for these operators depend on the discretization schemes used in the simulation. The first boundary condition bc_1 is imposed on the momentum equation and the second boundary condition bc_2 is imposed on the continuity equation. In the span-wise and stream-wise direction, the boundary conditions are periodic, while the wall-normal boundary condition is Dirichlet, as specified by the wall model dynamically.

Through block LU factorization and first-order approximation of the advection-diffusion operator, the matrix system in Equation (2.32) reduces to the following system of equations,

$$\begin{aligned} \mathbf{A}\ \mathbf{u}_*^{n+1} &= \mathbf{r}^n + \beta_m bc_1, && (2.33)\\ dt(\alpha_m + \beta_m)\mathbf{D}\ \mathbf{G}p' &= (\mathbf{D}\ \mathbf{u}_*^{n+1} + bc_2), && (2.34)\\ \mathbf{u}^{n+1} &= \mathbf{u}_*^{n+1} - dt(\alpha_m + \beta_m)\mathbf{G}p', \end{aligned}$$

where

$$\begin{aligned} \mathbf{A} &= \mathbf{I} - \frac{\beta_m dt}{Re}\mathbf{L}, \\ \mathbf{r}^n &= dt\left[-\gamma_m \mathbf{N}\ \mathbf{u}^n - \xi_m \mathbf{N}\ \mathbf{u}^{n-1} + \alpha_m(\mathbf{L}\ \mathbf{u}^n + bc_1^n) + \overline{\nabla p}\ \right]. \end{aligned}$$

Here, the matrix $\mathbf{I}$ is the identity matrix and $\mathbf{L}$ is the Laplacian operator. We apply the mean

pressure gradient in the stream-wise direction only. The subscript m denotes the index that follows the fractional steps. The discretizations resemble that of the second-order Adams-Bashforth method for the explicit terms and Crank-Nicolson for the implicit terms, but the coefficients are designed differently from these schemes in order to achieve third-order accuracy. The values of coefficients, α_m, β_m, γ_m, and ξ_m are given in Spalart *et al.* [125]. The spatial discretization employs a fourth-order finite difference method on a staggered grid in the stream-wise (x) and wall-normal (y) directions and a pseudo-spectral method is applied in the span-wise direction (z) with a p_1th-order Fourier exponential filter, which mimics the 2/3 rule in order to prevent aliasing errors [36, 19]. The boundary treatment, in part, follows Morinishi [83], where a ghost-point scheme extends the grid points beyond the computational domain so that a consistent stencil can be employed throughout. The ghost-point scheme is designed to globally conserve mass and momentum and is effectively equivalent to a one-sided finite-difference scheme at the walls [46]. The wall model uses the same numerical method as the Navier-Stokes equations for time-integration and the boundary points have been extended in a smiler way via the ghost-point scheme.

2.3.1 Helmholtz Equation for Pressure

Flow incompressibility is enforced by the pressure-Poisson equation. The three-dimensional Helmholtz equation reduces to a series of two-dimensional equations and ultimately a series of linear equations via Fourier transform in the span-wise direction, and cosine transforms in the stream-wise direction as described in Inoue & Pullin [46]. Here, the basic steps are introduced.

In the current implementation, the field variables are Fourier-transformed in the span-wise direction and discretized via fourth-order scheme in the other direction. Noting that since the domain is also periodic in the stream-wise direction, a discrete cosine transform can be applied to the flow variables and the pressure can be expressed as

$$p(x_i, y_j, k_z) = \frac{2}{N} \sum_{k_x=0}^{N-1} \widetilde{p}(k_x, y_j, k_z) \cos\left(\frac{\pi k_x (i+1/2)}{N}\right). \tag{2.35}$$

Denoting the RHS of Equation (2.34) by $f(x, y, k)$, the Helmholtz equation for pressure is expressed as

$$\mathbf{D}\,\mathbf{G}p(x_i, y_j, k_z) = \frac{\partial^2 p(x_i, y_j, k_z)}{\partial x_i^2} = f(x_i, y_j, k_z), \tag{2.36}$$

where the leading constant of the LHS of Equation (2.34) is neglected for simplicity. In the Fourier and cosine-transformed space, Equation (2.36) is expressed as

$$\frac{2}{N} \sum_{k_x=0}^{N-1} \left[\frac{\lambda_i}{\Delta x} + \delta_y^2 + k_z^2\right] \widetilde{p}(k_x, y_j, k_z) \cos\left(\frac{\pi k_x (i+1/2)}{N}\right) = \frac{2}{N} \sum_{k_x=0}^{N-1} \widetilde{f}(k_x, y_j, k_z) \cos\left(\frac{\pi k_x (i+1/2)}{N}\right), \tag{2.37}$$

where δ_y^2 is the fourth-order finite difference operator and λ_i is an explicit operator based on the fourth-order center difference given by

$$\lambda_i = 2\left(\cos\left(\frac{3\pi k_x(i+1/2)}{N}\right) - 54\cos\left(\frac{2\pi k_x(i+1/2)}{N}\right) + 783\cos\left(\frac{\pi k_x(i+1/2)}{N}\right) - 730\right). \tag{2.38}$$

Finally, Equation (2.37) is simplified to

$$\left[\frac{\lambda_i}{\Delta x} + \delta_y^2 + k_z^2\right]\widetilde{p}(k_x, y_j, k_z) = \widetilde{f}(k_x, y_j, k_z). \tag{2.39}$$

Note that if the application of this numerical method is to be limited to channel flow, the field variables could be transformed into Fourier space in the stream-wise direction as well. However, since such an operation would not be valid in an important canonical flow, the boundary layer, the cosine transform has been selected to keep the numerical method general.

2.4 Model Validation

Prior to discussing the present high Reynolds number LES, we make contact with the DNS results of Hoyas & Jiménez [43] for smooth-wall channel flow at $Re_\tau \sim 2,000$ and Flores & Jiménez [32], who have performed channel-flow DNS at $Re_\tau \sim 630$ where the non-slip and impermeability velocity boundary conditions are perturbed by zero-mean fluctuations in order to model the effect of roughness. The mean velocity profiles and stream-wise turbulent intensities are shown in Figure 2.1. For the rough-wall cases, the DNS profile at $Re_\tau = 632$ and $k_{s\infty}^+ = 129$ was obtained by perturbing both the stream-wise and wall-normal velocities. We remark that this technique could be adapted to the present LES approach as an alternative wall-model for roughness but is not explored presently. Also shown in Figure 2.1 is our LES profile at $k_{s\infty}^+ = 129$. Only a few LES data points overlap the DNS. This is because our LES has the requirement that the roughness be subgrid. Since $k_{s\infty}^+ = \epsilon\, Re_\tau$, then $k_{s\infty}^+ = 129$ and $Re_\tau = 632$ would give $\epsilon \approx 0.20$, which violates this condition with the present uniform grid. Our LES uses $Re_\tau = 2.58 \times 10^4$ and $\epsilon = 5 \times 10^{-3}$. Also included on the plot is the Colebrook-corrected log-law. The DNS result at $k_{s\infty}^+ = 129$ lies close to the LES results and the associated Colebrook corrected log-law expressed as

$$u^+ = \kappa^{-1}\log\left(y^+\right) + B - \kappa^{-1}\log\left(1 + 0.26k_{s\infty}^+\right). \tag{2.40}$$

The comparison of the stream-wise intensity (Figure 2.1-b) features only the rough-wall cases and shows reasonable agreement between the DNS result of Flores & Jiménez and our LES results. A relatively large discrepancy is observed closer to the wall and is attributed to the present wall-modeled LES, which does not resolve the near-wall region.

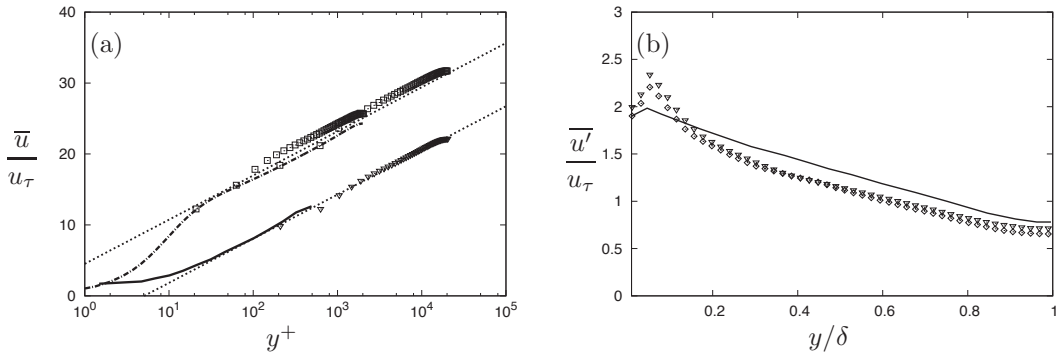

Figure 2.1: Comparison between LES and DNS[43, 32] (a) Mean velocity profiles, (b) stream-wise turbulence intensity. □ : LES $\epsilon = 0$ (Smooth), ▽ : LES $k_{s\infty}^+ = 129$, Dash-dot line: DNS smooth, Solid line: DNS $k_{s\infty}^+ = 129$, Dotted line: log-law with the Colebrook formula associated with LES with $\kappa = 0.37$ and $B = 4.5$.

2.5 Results

Large-eddy simulations are implemented with two different resolutions over a range of the relative roughness $\epsilon = k_{s\infty}/\delta$ as well as the Reynolds number from $Re_\tau = 650 - 2 \times 10^8$. The upper limit of the roughness ϵ is imposed by the assumption that the roughness of interest is subgrid, and hence it should not exceed the height of the lifted virtual wall, $k_{s\infty} < h_0$. This implies that the upper limit of the relative roughness is resolution dependent. With the current wall model, this upper limit of the relative roughness is estimated as $\epsilon < 0.18\Delta_y/\delta$. After a summary of the simulation conditions, some major results are discussed, including friction factor, mean velocity profile, universal asymptotic velocity defect profile, turbulent statistics, and dissipation.

2.5.1 LES Performed

A summary of the simulation conditions is given in Table 2.1. Most of the simulations have been implemented at two different resolutions to ensure the consistency of the results, which is discussed later in §2.5.2. The range of Reynolds number based on the friction velocity, $Re_\tau = 650-2\times10^8$, corresponds to the bulk-velocity based Reynolds number of $Re_b = \mathcal{O}(10^4)-\mathcal{O}(10^{10})$.

This bulk velocity is a simulation constant and fixed in time, while the mean stream-wise pressure gradient is time-varying and calculated such that the bulk velocity stays constant. In addition to the first sub-step of the time integration (Equation (2.33)), we solve the same equation with the RHS replaced by unity. The solution to the former problem, u_1, represents the intermediate velocity without the mean pressure gradient at all, while the solution to the latter, u_2, represents the intermediate velocity with only the pressure gradient being applied. The bulk velocity of u_1 is then compared to the desired bulk velocity with respect to that of u_2, and through this comparison we obtain the coefficient α that represents the amount of pressure gradient necessary to achieve the mass flux desired. Finally, due to the linearity of Equation (2.33), the intermediate velocity is corrected as $u_*^{n+1} = u_1 + \alpha u_2$. Whether the simulation is implemented with the mean pressure gradient or bulk velocity fixed makes no discernible

Table 2.1: Summary of LES simulations. The first letter of each case indicates the resolution (high or low). The first and second number of each case indicate different realizations of ϵ and Re_τ, respectively.

Case	Re_τ	L_x/δ	L_y/δ	L_z/δ	N_x	N_y	N_z	ϵ	ϵRe_τ
L0.1 − L0.6	$650 - 2 \times 10^6$	32	2	8	192	48	48	0	0
L1.1 − L1.6	$650 - 2 \times 10^6$	32	2	8	192	48	48	1×10^{-4}	$0.065 - 200$
L2.1 − L2.6	$650 - 2 \times 10^6$	32	2	8	192	48	48	5×10^{-4}	$0.325 - 1000$
L3.1 − L3.6	$650 - 2 \times 10^6$	32	2	8	192	48	48	1×10^{-3}	$0.65 - 2000$
L4.1 − L4.6	$650 - 2 \times 10^6$	32	2	8	192	48	48	2×10^{-3}	$1.3 - 4000$
L5.1 − L5.6	$650 - 2 \times 10^6$	32	2	8	192	48	48	5×10^{-3}	$3.25 - 10000$
H0.1 − H0.9	$650 - 2 \times 10^8$	32	2	8	384	96	96	0	0
H1.6	2×10^6	32	2	8	384	96	96	1×10^{-6}	2
H2.6	2×10^6	32	2	8	384	96	96	5×10^{-6}	10
H3.5 − H3.6	$2 \times 10^5 - 2 \times 10^6$	32	2	8	384	96	96	1×10^{-5}	$2 - 20$
H4.5	2×10^5	32	2	8	384	96	96	5×10^{-5}	10
H5.1 − H5.9	$650 - 2 \times 10^8$	32	2	8	384	96	96	1×10^{-4}	$0.065 - 200$
H6.1 − H6.9	$650 - 2 \times 10^8$	32	2	8	384	96	96	5×10^{-4}	$0.325 - 1000$
H7.1 − H7.9	$650 - 2 \times 10^8$	32	2	8	384	96	96	1×10^{-3}	$0.65 - 2000$
H8.1 − H8.6	$650 - 2 \times 10^6$	32	2	8	384	96	96	2×10^{-3}	$1.3 - 4000$
H9.1 − H9.9	$650 - 2 \times 10^8$	32	2	8	384	96	96	5×10^{-3}	$3.25 - 10000$

difference in the resultant statistics.

Typically, the simulation requires $15-20$ convection times for the statistics up to second order to settle. With an exception of the data for the flow visualization, the data for any statistical quantity is first averaged in time and second in space. One-dimensional statistics use the spatial average in all three directions, while two-dimensional statistics such as the wall-normal profiles use the planar average.

2.5.2 Friction Factor from LES

Channel flows are driven by their mean pressure gradient. One way of measuring this is to define the friction factor. For both channel and pipe flows, friction factor is defined as the mean pressure gradient scaled by the dynamic pressure, which can be written using the friction velocity as

$$f \equiv \frac{-2\,\delta\,\overline{dp/dx}}{\rho\,u_b^2} = \frac{2\,\overline{\tau_w}}{\rho\,u_b^2}, \tag{2.41}$$

$$= 2\,\frac{u_\tau^2}{u_b^2}, \tag{2.42}$$

where u_b denotes the channel bulk velocity, and $\overline{\tau_w}$ is the wall-averaged shear stress. We have used $-\overline{dp/dx} = \overline{\tau_w}/\delta$ for the channel flow and $\overline{\tau_w} = \rho u_\tau^2$, where u_τ is the wall-time-averaged square friction velocity.

From each LES the friction factor f is calculated in accordance with Equation (2.42), where the time-average of the ratio of wall-averaged u_τ^2 to bulk velocity u_b^2 at every instance is calculated. Defining the bulk Reynolds number as $Re_b = \delta u_b/\nu$ then defines LES-generated points for the function $f = f(\epsilon, Re_b)$. These are shown in Figure 2.2 against Re_b for various ϵ. The

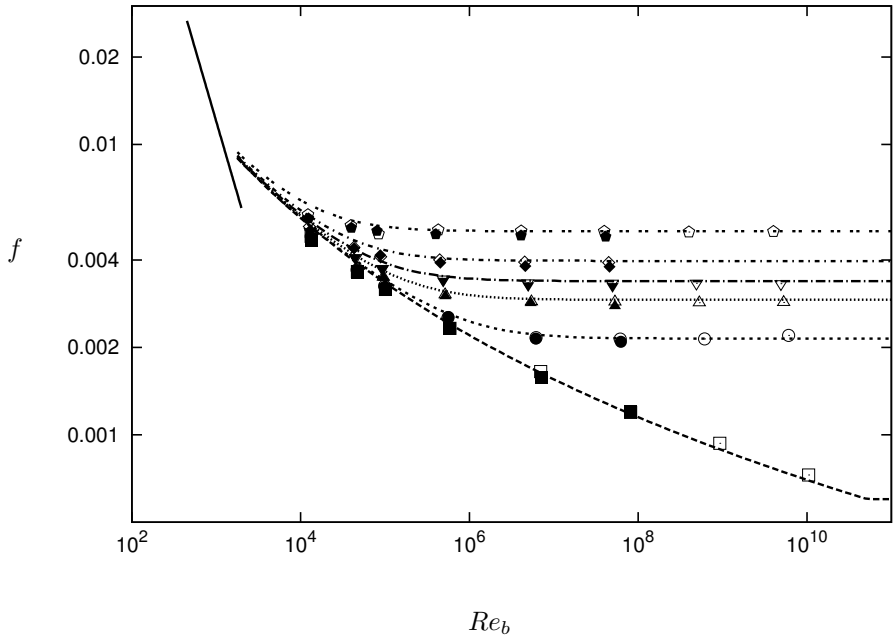

Figure 2.2: Friction factor as a function of Re_b at various roughness ϵ. Open symbols, high resolution H5.1-H9.6. Solid symbols, low resolution L0.1-L5.6. Symbols indicate $\square:\ \epsilon = 0$, $\bigcirc:\ \epsilon = 1 \times 10^{-4}$, $\triangle:\ \epsilon = 5 \times 10^{-4}$, $\bigtriangledown:\ \epsilon = 1 \times 10^{-3}$, $\diamond:\ \epsilon = 2 \times 10^{-3}$, $\pentagon:\ \epsilon = 5 \times 10^{-3}$. Dashed line, empirical results from §2.5.3. Solid line, theoretical laminar result $f = 12/Re_b$.

open and solid symbols distinguish the high resolution cases (H5.1-H9.9) and low resolution cases (L0.1-L5.6), respectively. These results can be viewed as a Moody-like diagram obtained from LES for the given $\Delta U(k^+_{s\infty})$. Our results cover the fully turbulent regime consisting of smooth, transitionally rough and fully rough flows. For the smooth-wall case $\epsilon = 0$, the friction factor continuously decreases with Reynolds number. In contrast, at fixed $\epsilon > 0$, the friction factor decreases with Reynolds number, passing through a Reynolds number dependent phase in the hydrodynamically smooth regime and the transitional regime, and finally approaches a Reynolds number independent phase in the fully rough regime. This asymptotic rough-wall limit is not built into either the wall model or the LES, but results from the overall LES-wall-model dynamic calculation.

2.5.3 Empirical Equivalent Moody Diagram

The original Moody diagram is a representation of friction factor in a pipe as a function of Reynolds number and roughness as introduced by Moody [82]. It is a graphical representation of an empiricism developed by Colebrook [22]. Presently we obtain an empirical Moody-diagram for channel flow for comparison with the LES results. We utilize an empirical log-law corrected for roughness with the Colebrook formula as

$$\frac{\widetilde{u}(y)}{u_\tau} = \frac{1}{\kappa}\log\left(\frac{yu_\tau}{\nu}\right) + B + \frac{\Pi}{\kappa}\mathcal{W}\left(\frac{y}{\delta}\right) - \frac{1}{\kappa}\log\left(1 + 0.26\epsilon Re_\tau\right), \tag{2.43}$$

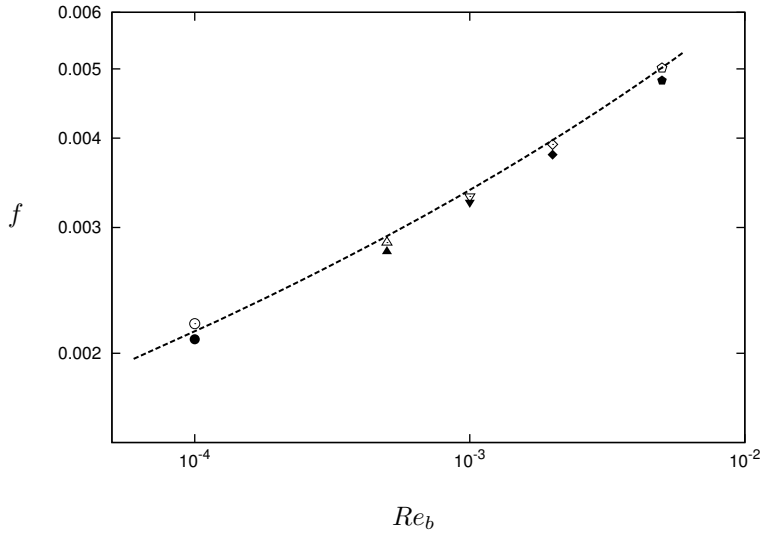

Figure 2.3: High Reynolds number limit of friction factor for rough walls. Open symbols, fully rough regime (H5.6, H6.6, H7.6, H8.6, H9.6). Solid symbols, fully rough regime (L1.6, L2.6, L3.6, L4.6, L5.6). Dashed line, mathematical limit of empirical result obtained by Equation (2.47) with $\kappa = 0.37$ and $B = 4.5$.

where here κ is the Kármán constant, B is the constant term of the log-law, Π is the Coles wake factor, $\mathcal{W}(y/\delta)$ is the universal wake function, and u_τ is here interpreted as an average (wall or time-averaged or both) friction velocity. Presently, for simplicity we neglect the wake contribution since it is small for channel flow.

In integrating Equation (2.43) to obtain u_b, an approximation to the velocity profile below the log-region is required. Three possible approximations are : (I) The log-law is assumed to extend to the wall at $y_0^+ = 0$, which is the lower integration limit. (II) The log-law is solved for y_0^+ assuming $u^+(y_0^+) = 0$, and this result is substituted as the lower integration limit y_0 such that the inner scaled velocity is zero at the lower integration limit. (III) The piecewise integral of the linear and log-profiles of the velocity with intercept h_ν^+. For rough walls, this intercept depends on roughness and hence it requires solving a relation equating the linear and log-profiles of the velocity, which does not have real solutions for $k_{s\infty}^+ > 14$ approximately. The three methods of computing u_b were all implemented and found to give similar results to plotting accuracy. In practice, Method (I) is used for its simplicity, for which

$$\begin{aligned} \frac{u_b}{u_\tau} &= Re_\tau^{-1}\left[\int_0^{Re_\tau}\left(\kappa^{-1}\log y^+ + B - \Delta U^+\right)dy^+\right], \\ &= \frac{1}{\kappa}\left(\log\left(Re_\tau\right) - 1\right) + B - \Delta U^+. \end{aligned} \tag{2.44}$$

Substituting Equation (2.44) into Equation (2.42) together with the Colebrook formula then gives an empirical function $f = f(\epsilon, Re_\tau)$. If we further note that the bulk Reynolds number and friction Reynolds number are related via

$$Re_b = Re_\tau\,\frac{u_b}{u_\tau} = Re_\tau\sqrt{\frac{2}{f}}, \tag{2.45}$$

then an implicit expression involving the friction factor and other parameters is obtained as

$$f = 2\left[\frac{1}{\kappa}\left(\log\left(Re_b\sqrt{f/2}\right) - 1\right) + B - \frac{1}{\kappa}\log\left(1 + 0.26\epsilon Re_b\sqrt{f/2}\right)\right]^{-2}. \tag{2.46}$$

The value of the Kármán constant and additive constant B of the log-law are computed by least-square fitting our high resolution LES data to Equation (2.46) and taking the average across different roughness levels; this fitting gives $\kappa = 0.37$ and $B = 4.5$. In taking the average, the data below Reynolds number $Re_\tau = 2 \times 10^4$ has been excluded, since this regime is not considered high enough Reynolds number to have sufficient scale-separation for obtaining accurate values of the log-law constants. Using these values, the empirical predictions with Equation (2.46) are shown in Figure 2.2, in addition to the LES results. The empirical predictions and LES results are well matched, with some difference for low Re_b. For the highest relative roughness case of $\epsilon = 5 \times 10^{-3}$, the equivalent sand roughness height actually exceeds the virtual wall height, thus violating one of the assumptions of subgrid roughness. Nonetheless, the friction factors are robustly calculated and match the empirical curve reasonably well. The values at the lower resolution are somewhat below the higher resolution cases but the differences are small. We use the higher resolution grid in the remainder of the LES studies since the larger number of data points provides more detailed insights, while the higher resolution grid is still computationally affordable. To the best of our knowledge Figure 2.2 is the first attempt to calculate a Moody-like diagram for rough-wall channel flows using either LES or DNS.

The limiting case of the empirical friction factor in the fully rough asymptotic regime can be obtained by taking the limit of Equation (2.44) when $Re_\tau \to \infty$ with ϵ fixed. This gives

$$\begin{aligned}
\lim_{Re_\tau\to\infty} f &= \lim_{Re_\tau\to\infty} 2\left[\frac{1}{\kappa}\left(\log\left(Re_\tau\right) - 1\right) + B - \frac{1}{\kappa}\log\left(1 + 0.26\epsilon Re_\tau\right)\right]^{-2}, \\
&= \begin{cases} \dfrac{2}{\left(B - \kappa^{-1}\left(\log\left(0.26\,\epsilon\,\right) + 1\right)\right)^2} & \text{for} \quad \epsilon \neq 0 \\ 0 & \text{for} \quad \epsilon = 0. \end{cases}
\end{aligned} \tag{2.47}$$

For $\epsilon > 0$, this limit is shown in Figure (2.3) together with the LES estimate obtained at $Re_b = 2 \times 10^6$ with good agreement for our high-resolution LES.

2.5.4 Mean Velocity Profiles

The inner-scaled, mean velocity profiles from the LES results show collapse on constant values of ϵRe_τ ranging from 2 to 2000 as illustrated in Figure 2.4 for $\{\epsilon : 0, 1\times10^{-6}, 5\times10^{-6}, 1\times10^{-5}, 5\times10^{-5}, 1\times10^{-4}, 1\times10^{-3}\}$ and $\{Re_\tau : 2\times10^4, 2\times10^5, 2\times10^6\, 2\times10^7, 2\times10^8\}$. At each value of Reynolds number, the inner-scaled mean velocity profile is shifted downwards as the relative roughness is increased, and this is expected in rough-wall flows where surface drag is increased by roughness elements. Since we have applied Colebrook's velocity deficit to the inner scaling in the region below the virtual wall, the observed downward shift of the mean velocity profiles are partially expected; the wall model reduces the boundary condition by the amount suggested by

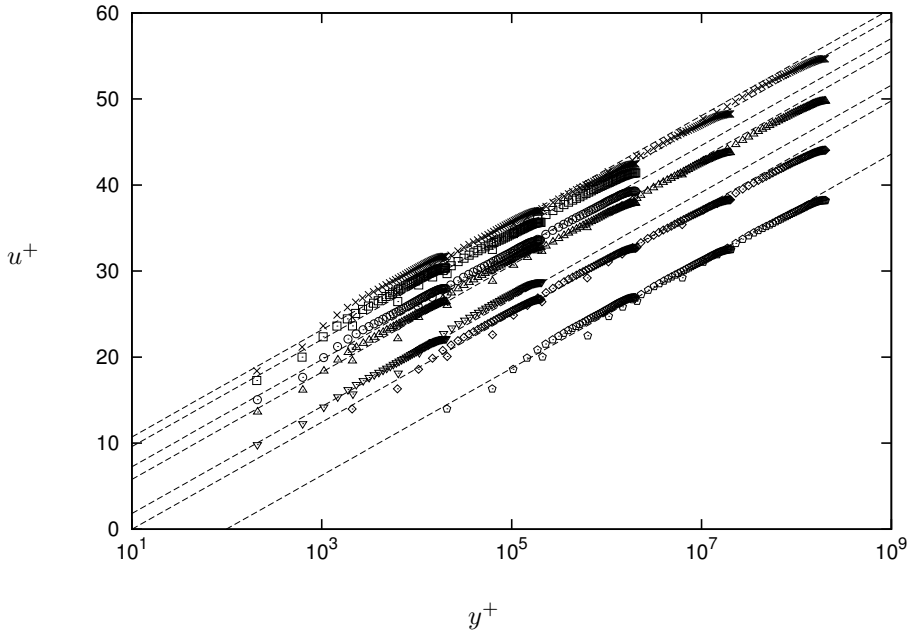

Figure 2.4: Mean velocity profiles. Open symbolds, LES results $\times$: $\epsilon Re_\tau = 0$, $\square$: $\epsilon Re_\tau = 2$, $\bigcirc$: $\epsilon Re_\tau = 10$, $\triangle$: $\epsilon Re_\tau = 20$, $\bigtriangledown$: $\epsilon Re_\tau = 100$, $\diamond$: $\epsilon Re_\tau = 200$, $\pentagon$: $\epsilon Re_\tau = 2000$. Dashed lines, empirical log-law with Colebrook's formula.

the Colebrook's formula. However, the region below the virtual wall, where the velocity deficit due to roughness is directly imposed by the model corresponds to only 0.4% of δ and the rest of the flow must pick up the roughness information through the information transmitted by the wall model.

The wall effect is visible, although it is relatively small. The sensitivity of the LES to the height of the virtual wall, i.e. the value of h_0/Δ_y, has been investigated for $0.09 < h_0/\Delta_y < 0.36$. It has been shown that the centerline velocity of each case does not depart from the case with the currently adopted value of 0.18 by more than 5%, as is consistent with the observation of Chung & Pullin [19].

Also plotted in Figure 2.4 are the log-law and the Colebrook based velocity profiles with the Kármán constant $\kappa = 0.37$ as computed by fitting the friction factor data of the LES in §2.5.3. We recall from Equation (2.43) that with a roughness correction, the log-law intercepts are shifted downwards, and that the amount of the shift solely depends on the value of $k_{s\infty}^+ = \epsilon Re_\tau$. This is consistent with the LES results in Figure 2.4. For the smooth-wall cases ($\epsilon = 0$), the LES fits well with the empirical results with its intercept $B = 4.5$. This value of the intercept is in agreement with our wall model definition in Equation (2.19) and, due to our higher Reynolds number regime, is consequently lower than the classic value of ≈ 5 (as in the numerical study at $Re_\tau = 620$ conducted by Moin & Kim [79]). For rough walls, the LES results also closely align themselves with the empirical profiles having intercept $4.5 - \kappa^{-1}\log(1 + 0.26\epsilon Re_\tau)$ for each value of ϵRe_τ, thus providing a quantification of the momentum loss due to roughness from the perspective of an inner-scaled mean velocity profile. We note that the LES profiles span the entire transitionally rough regime.

2.5.5 Universal Asymptotic Velocity Deficit Profile

When wall surfaces are rough there exists a universal asymptotic velocity profile in the limit of $Re_\tau \to \infty$. To demonstrate this, we take the limit of the empirical log-law with Colebrook's roughness correction by allowing $Re_\tau \to \infty$ and we arrive at a universal, asymptotic velocity-deficit profile for rough walls. Our analysis starts by considering the ratio of the mean velocity to the centerline velocity, $\widetilde{u}(y)/u_c$ where u_c is the channel centerline velocity. We write this as Equation (2.48) and consider both ratios on the RHS separately.

$$\frac{\tilde{u}\,(y)}{u_c} = \frac{\tilde{u}\,(y)}{u_\tau}\frac{u_\tau}{u_c}. \tag{2.48}$$

The first ratio $\tilde{u}(y)/u_\tau$ is given by the empirical log-law, with Colebrook's roughness correction (Equation (2.43)) and its limit is expressed in terms of the wall-normal distance and relative roughness ϵ in the limit of large Reynolds number as

$$\begin{aligned}\lim_{Re_\tau\to\infty}\frac{\tilde{u}\,(y)}{u_\tau} &= \lim_{Re_\tau\to\infty}\frac{1}{\kappa}\log\left(y^+\right) + B - \frac{1}{\kappa}\log\left(1+0.26\,\epsilon Re_\tau\right), \\ &= \frac{1}{\kappa}\log\left(\frac{y}{\delta}\right) + B - \frac{1}{\kappa}\log\left(0.26\,\epsilon\right).\end{aligned} \tag{2.49}$$

The second ratio u_τ/u_c is given by the log-law with Colebrook formula evaluated at the centerline $y=\delta$, whose limit of high Reynolds number is obtained as

$$\begin{aligned}\lim_{Re_\tau\to\infty}\frac{\tilde{u}\,(\delta)}{u_\tau} = \lim_{Re_\tau\to\infty}\frac{u_c}{u_\tau} &= \lim_{Re_\tau\to\infty}\frac{1}{\kappa}\log\left(\frac{\delta u_\tau}{\nu}\right) + B - \frac{1}{\kappa}\log\left(1+0.26\epsilon Re_\tau\right), \\ &= B - \frac{1}{\kappa}\log\left(0.26\epsilon\right).\end{aligned} \tag{2.50}$$

Using these two ratios (Equation (2.49) and (2.50)) in Equation (2.48) then gives the ratio of $\tilde{u}(y)/u_c$ in the high Reynolds number limit as

$$\frac{\tilde{u}(y)}{u_c} = \frac{\kappa^{-1}\log\left(y/\delta\right) + B - \kappa^{-1}\log\left(0.26\,\epsilon\right)}{B - \kappa^{-1}\log\left(0.26\,\epsilon\right)}, \tag{2.51}$$

which can then be rearranged to obtain the deficit form

$$K\left(1-\frac{\tilde{u}(y)}{u_c}\right) = -\frac{1}{\kappa}\log\left(\frac{y}{\delta}\right) \text{ where } K = B - \kappa^{-1}\log\left(0.26\,\epsilon\right). \tag{2.52}$$

Figure 2.5 shows the LES results plotted in the form of the LHS of Equation (2.52) that are to be compared with the RHS of Equation (2.52) using $\kappa = 0.37$. The left figure (Figure 2.5-a) includes all LES data regardless of the Reynolds number or roughness level (H5.1-H9.6). These cases include profiles for the transitionally rough regime up to the fully rough regime, and they are observed to deviate from the log-profile suggested by Equation (2.52). In Figure 2.5-b, the profiles are limited to those that show collapse on the RHS of Equation (2.52), including the most rough case of $\epsilon = 5\times10^{-3}$ at $Re_\tau = 2{,}000$ as well as the least rough cases of

$\epsilon = 1 \times 10^{-4}$ at $Re_\tau = 2 \times 10^6$. Physically, the collapse can be explained by Townsend's hypothesis, noting that the LHS of Equation (2.52) recovers the standard defect form in the limit of high Reynolds number. Commonly true for the collapsed profiles is that the values of $k^+_{s\infty}$ are above the order of unity, which approximately corresponds to the fully rough regime in our friction factor plot (Figure 2.2). This supports that given a sufficiently large value of $k^+_{s\infty}$, the high-Reynolds-number-asymptotic-limit is in fact universal with a Colebrook-type roughness characterization in the sense that the flow at all Reynolds number and roughness satisfies the deficit profile given sufficiently high $k^+_{s\infty}$. Presently, we have used an empirical roughness function with $\Delta U^+ \sim \kappa^{-1}\log(\epsilon Re_\tau)$ with $\epsilon = k_{s\infty}/\delta$. Equation (2.52) suggests an empirical method for determining an equivalent geometrical roughness for a given surface defined as $k_{s\infty}$, obtained by determining the value of K that gives the best fit for the experimental velocity profile. Values for B and κ would be required.

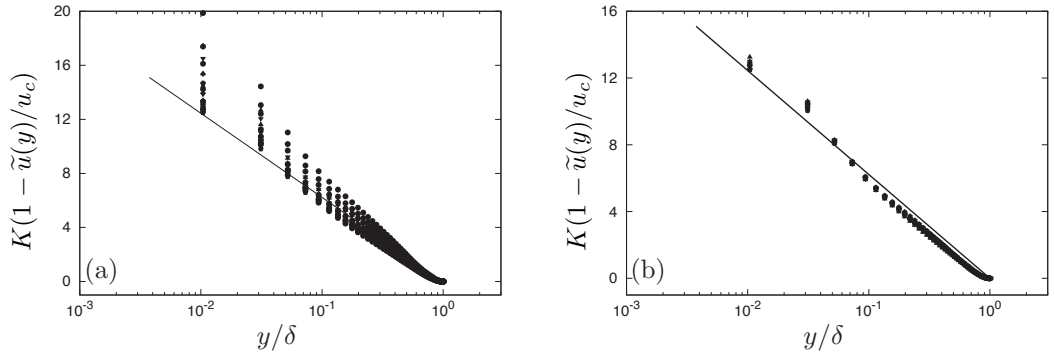

Figure 2.5: Universal asymptotic velocity profiles. (a) $K(1-\widetilde{u(y)}/u_c)$ for H5.1-H9.6 , (b) $K(1-\widetilde{u}(y)/u_c)$ for H5.5-H5.6, H6.4-H6.6, H7.4-H7.6, H8.3-H8.6, and H9.2-H9.6. Solid line, $\kappa^{-1}\log(y/\delta)$. Symbols, LES results.

2.5.6 Turbulent Statistics

We now examine turbulent statistics to explore roughness and Reynolds number effects on statistical quantities scaled on the outer length scale δ and friction velocity u_τ. We consider single point statistics above the virtual wall, including fluctuations of velocity and Reynolds shear stress, while distinguishing between the subgrid and total components of these quantities. First, we examine a set of data where the entire range of Re_τ and ϵ is present, i.e. smooth, trasitionally rough, and fully rough regimes, shown in Figure 2.6. A common observation in all these statistical quantities is their uniform collapse upon scaling with u_τ, although a weak dependence on Re_τ and ϵ over the range of Re_τ from 2×10^3 to 2×10^8 is noted except at $Re_\tau = 650$, since the wall model is designed for higher Reynolds number. Also notable in Figure 2.6 is that the subgrid components of the fluctuations in the span-wise and wall-normal direction, as well as in the Reynolds shear stress, illustrate an inherent feature of the stretched vortex SGS model, that being that the subgrid components are dominant near the wall while their effect is felt to a lesser extent as we approach the centerline. Statistics for smooth-wall cases are examined below,

followed by the rough-wall cases.

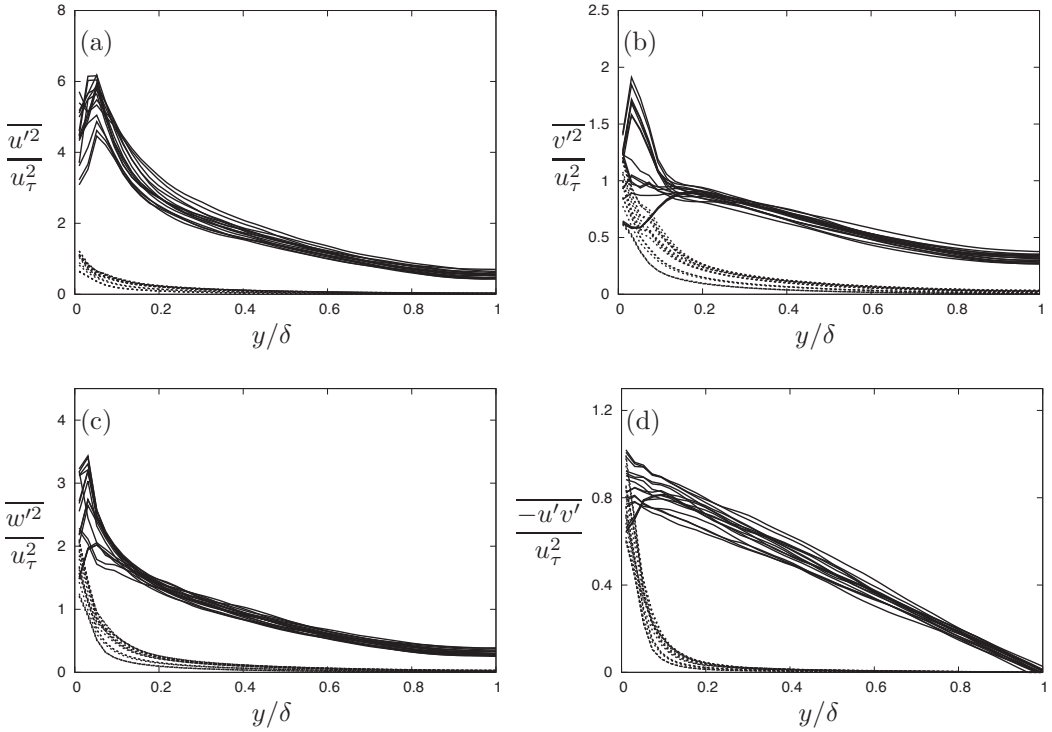

Figure 2.6: Turbulent statistics for both smooth and rough walls over full range of Reynolds number. Solid lines, total components. Dashed lines, subgrid components. Reynolds number and relative roughness ranges are $650 \leq Re_\tau \leq 2 \times 10^8$ and $0 \leq \epsilon \leq 5 \times 10^{-3}$.

Smooth-wall cases: $\epsilon = 0$

A subset of data in Figure 2.6 corresponding to the statistics of smooth-wall cases is discussed. Over the full range of Reynolds number ($650 \leq Re_\tau \leq 2 \times 10^8$), we observe at least some degree of Reynolds number dependence, yet it is only when the higher Reynolds number cases are considered, as in Figure 2.7, that a remarkable improvement in collapse is observed. In addition to their collapse, Reynolds stresses show linear profiles ranging from zero at the channel centerline to unity at the wall.

Recent studies of smooth-wall flows (e.g. Marusic & Kunkel [67]) suggest that the stream-wise intensities show a log-profile for the outer part of smooth flat-plate boundary layer flow. The stream-wise intensities from our smooth-wall LES are plotted on semi-log axes in Figure 2.8. While the profiles show variations for small Reynolds numbers ($Re_\tau \leq 2 \times 10^5$) as we observe in Figure 2.8-a, those at high Reynolds numbers ($Re_\tau \geq 2 \times 10^6$) collapse well on $\log(y/\delta)$ in the outer flow in Figure 2.8-b. The LES cannot probe the near-wall region and so we expect our results to be accurate only for $y/\delta \geq 0.1$. Here the stream-wise fluctuations are bounded above by the sum of a log-profile plus an additional term $T\,(y/\delta)$ introduced to represent the departure

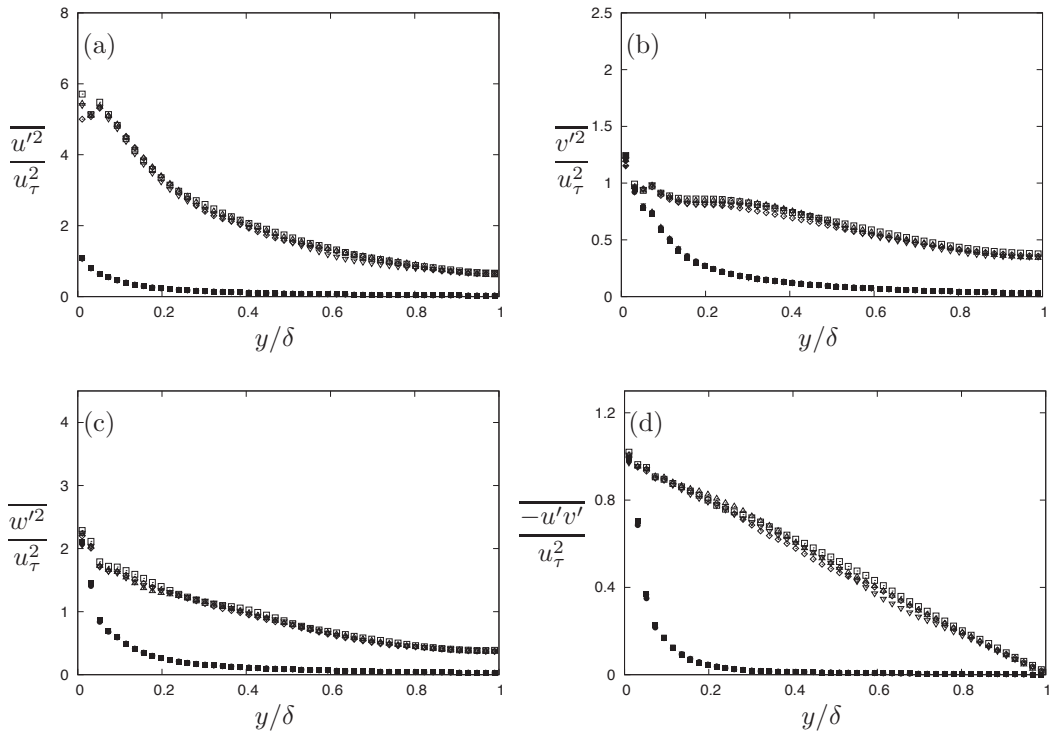

Figure 2.7: Turbulent statistics for smooth-wall at high Reynolds number. Open symbols, total components. Solid symbols, subgrid components. $\square$: $Re_\tau = 2 \times 10^6$, $\bigcirc$: $Re_\tau = 1 \times 10^7$, $\triangle$: $Re_\tau = 2 \times 10^7$, $\diamond$: $Re_\tau = 2 \times 10^8$.

of the profile from the logarithmic line near the centerline

$$\frac{\overline{u'^2}}{u_\tau^2} = \alpha \log\left(\frac{y}{\delta}\right) + \beta + T\left(y/\delta\right), \tag{2.53}$$

Clearly, $T\left(y/\delta\right) \to 0$, as $y/\delta \to 0$. In Equation(2.53), $\overline{(\,)}$ denotes the temporal-planar average, and $(\,)'$ denotes the fluctuating quantities. Allowing adequate distance from the wall and centerline, where $T\left(y/\delta\right)$ is very small, the coefficients in each case are determined by a least-squares regression, which are then averaged across the range of Re_τ to obtain $(\alpha, \beta) = (-1.82, 0.433)$. The implications of this result are explored in §2.8.

Rough-wall cases : $\epsilon \geq 0$

Smooth-wall data makes up one end of the ϵRe_τ range, while at the other end is the rough-wall data, shown in the fully rough regime in Figure 2.9 at Reynolds numbers above $Re_\tau > 2 \times 10^5$. In comparison to the all-encompassing plot of Figure 2.6 where smooth, transitionally rough, and fully rough cases are included, the collapse of exclusively fully rough cases improves, with persisting weak dependencies on Reynolds number and roughness. Note that, for the total components of Reynolds stress in the fully rough regime, the plots of higher values of ϵ tends to lie nearer the origin.

We seek further insight into the logarithmic nature of stream-wise fluctuations by fitting

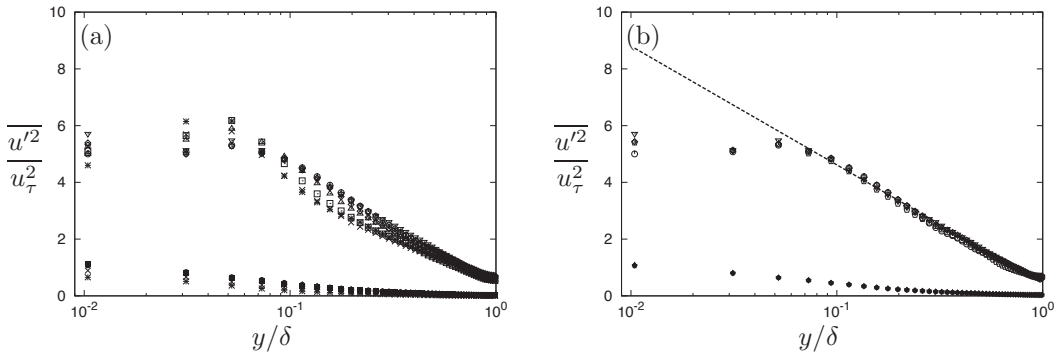

Figure 2.8: Stream-wise velocity fluctuations on log-scaled wall-normal distance for smooth-wall cases. (a) Over full range of Reynolds numbers (H0.1-H0.9), (b) At high Reynolds number. Open symbols, total components. Solid symbols, subgrid components. $*$: $Re_\tau = 650$, $\times$: $Re_\tau = 2 \times 10^3$, $\square$: $Re_\tau = 2 \times 10^4$, $\bigcirc$: $Re_\tau = 2 \times 10^5$, $\triangle$: $Re_\tau = 2 \times 10^6$, $\bigtriangledown$: $Re_\tau = 1 \times 10^7$, $\diamond$: $Re_\tau = 2 \times 10^7$, $\pentagon$: $Re_\tau = 2 \times 10^8$. Dashed lines indicate the fitted line according to Equation (2.53).

rough-wall cases with the functional form in Equation (2.53), shown in Figure 2.10. The left pane (Figure 2.10-a) shows cases including smooth, transitional, and fully rough cases, and the right pane (Figure 2.10-b) emphasizes the asymptotic regime by retaining only fully rough data. The collapse is observed to be improved for fully rough cases. When including all the cases, the coefficients of Equation (2.53) are calculated to be $(\alpha, \beta) = (-1.63, 0.315)$, and $(\alpha, \beta) = (-1.65, 0.322)$ when only fully rough cases are included.

2.6 Dissipation

To discuss the dissipation ε we use $\langle Q \rangle$, $\overline{Q}$, and $\widehat{Q}$ to denote a volume-average over the flow domain, a plane-average over an $(x - z)$ plane and a time-average, respectively. We consider the full Navier-Stokes equations for rough-wall channel flow. It is assumed that the bottom wall shape is $y = k_l(x, z)$ and the top wall is $y = 2\delta + k_u(x, z)$, where both $k_l(x, z)$, $k_u(x, z)$ are periodic in x and z with $\overline{k_l(x, z)} = \overline{k_u(x, z)} = 0$. It is further assumed that any cross section of the channel normal to the x-axis has area $A_x = L_x L_z$ that is independent of x so that the channel volume is $V = 2\,\delta\,L_x\,L_z$. The pressure is expressed as

$$p = \mathcal{G}_j(t)\, x_j + p'(x_1, x_2, x_3, t), \tag{2.54}$$

$$\frac{\partial p}{\partial x_i} = \mathcal{G}_j(t)\delta_{ij} + \frac{\partial p'}{\partial x_i}, \tag{2.55}$$

where $x_1 \equiv x$, $x_2 \equiv y$, $x_3 \equiv z$, $\mathcal{G}_i(t)$ is the time-fluctuating mean pressure gradient and $P'(x_1, x_2, x_3, t)$ is periodic in x_1 and x_3. It is further assumed that there is no span-wise mean pressure gradient $\mathcal{G}_2(t) = 0$, which was enforced in the present code.

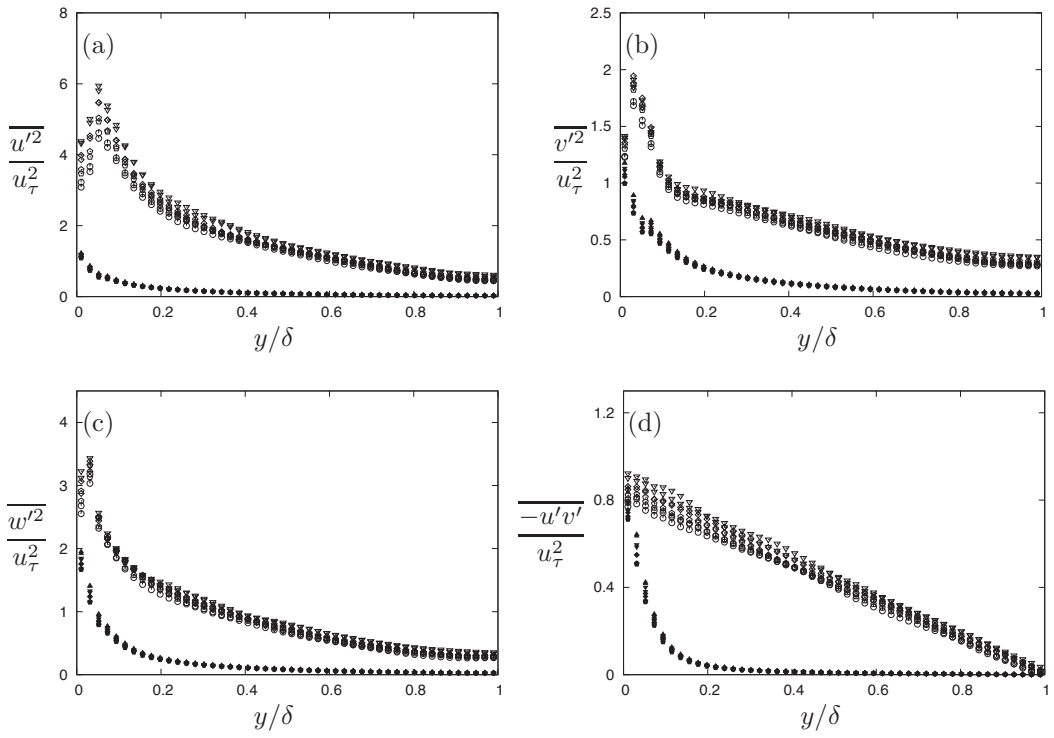

Figure 2.9: Turbulence statistics in fully rough regime at Reynolds numbers above $Re_\tau > 2\times10^5$. Open symbols, total components. Solid symbols, subgrid components. $\triangle:\ \epsilon = 1\times10^{-4}$, $\bigtriangledown:\ \epsilon = 5\times10^{-4}$, $\diamond:\ \epsilon = 1\times10^{-3}$, $\pentagon:\ \epsilon = 2\times10^{-3}$, $\bigcirc:\ \epsilon = 5\times10^{-3}$.

Let us take the volume-average of the Navier-Stokes momentum equations at fixed time t,

$$\frac{\partial}{\partial t}\langle u_i\rangle + \frac{1}{V}\iiint_V \frac{\partial}{\partial x_j}u_iu_jdV = -\frac{1}{V}\iiint_V \frac{\partial p/\rho}{\partial x_i}dV + \frac{\nu}{V}\iiint_V \frac{\partial^2 u_i}{\partial x_j^2}dV. \tag{2.56}$$

Via the divergence theorem, i.e. $\iiint_V \frac{\partial F_i}{\partial x_i}dV = \oiint_S n_i.F_i dS$, convert the volume integrals to surface integrals (except for the unsteady term) and using the periodic and no-slip boundary conditions, the above equation simplifies to

$$\frac{\partial}{\partial t}\langle u_i\rangle = -\frac{G_j}{\rho}\delta_{ij} - \frac{1}{V}\iint_{wall}\frac{p'}{\rho}n_i dS + \frac{1}{V}\iint_{wall}\frac{\partial u_i}{\partial x_j}n_j dS. \tag{2.57}$$

Here, the mean shear stress $\overline{u_\tau^2} = \overline{\tau_w/\rho}$ is defined as the drag force per unit area averaged over both walls in the sense of Equation (2.10), but the integral domain is extended to a plane-average over both complete channel walls. Consequently, the stream-wise momentum equation simplifies to

$$\frac{\partial\langle u_1\rangle}{\partial t} = -\frac{\mathcal{G}_1(t)}{\rho} - \frac{\overline{u_\tau^2}}{\delta}. \tag{2.58}$$

The dissipation can be obtained by multiplying the Navier Stokes equations by u_i, taking a

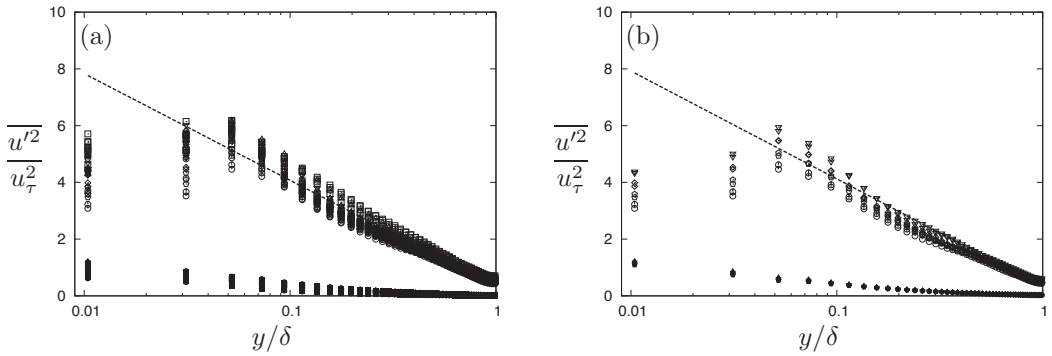

Figure 2.10: Stream-wise velocity fluctuation on log-scaled wall-normal distance. (a) Smooth, transitionally rough, and fully rough regime over full range of Reynolds number, (b)Fully rough regime. Open symbols, total components. Solid symbols, subgrid components. $\triangle:\ \epsilon = 5\times10^{-4}$, $\bigtriangledown:\ \epsilon = 1\times10^{-3}$, $\diamond:\ \epsilon = 2\times10^{-3}$, $\pentagon:\ \epsilon = 5\times10^{-3}$. Dashed lines indicate the fitted line according to Equation (2.53).

volume integral, and again converting volume to surface integrals:

$$\frac{\partial}{\partial t}\langle\frac{1}{2}u_i^2\rangle + \frac{1}{V}\iint n_j\left(\frac{1}{2}u_i^2u_j\right)dS = -\frac{1}{V}\iint n_iu_i\frac{p}{\rho}dS + \frac{\nu}{V}\iiint u_i\frac{\partial^2u_i}{\partial x_j^2}dV. \tag{2.59}$$

Applying boundary conditions and stream-wise periodicity then leads to

$$\frac{\partial\langle\frac{1}{2}\mathbf{u_i}^2\rangle}{\partial t} = -\frac{\mathcal{G}_1(t)}{\rho}\,u_1^{(in)} - \varepsilon(t), \tag{2.60}$$

where $u_1^{(in)}$ and $u_1^{(out)}$ are the mean inlet and outlet stream-wise velocity respectively (equal owing to periodicity), and where $\varepsilon(t) = 2\,\nu\langle\mathbf{S}.\mathbf{S}\rangle$ is the volume-averaged dissipation. The first term on the right-hand side is the pressure work and we note that there is no contribution to this from the generally non-zero but fluctuating mean span-wise velocity at the channel side planes since $\mathcal{G}_2 = 0$, and no contribution from the wall-normal motions owing to the wall boundary conditions and the co-ordinate-normal side planes.

Since $A_1(x)$ is constant then from continuity and periodicity of u_3, $\langle u_1\rangle \equiv u_b(t) = u_1^{(in)} = u_1^{(out)}$. Eliminating $\mathcal{G}_1(t)$ from (2.58) and (2.60) gives

$$\frac{\partial}{\partial t}\left(\langle\frac{1}{2}\mathbf{u}^2\rangle - \frac{1}{2}\langle u_1\rangle^2\right) = u_b(t)\,\frac{\overline{u_\tau^2}(t)}{\delta} - \varepsilon(t). \tag{2.61}$$

We now assume that the channel flow is statistically stationary. The present LES is performed using constant mass flow, in which case u_b is independent of time but $\mathcal{G}_1$ is time-varying and fluctuates about a non-zero mean that, from (2.58), balances the time-averaged wall drag. On taking a long time average of (2.61) we obtain

$$\frac{\delta\,\widehat{\varepsilon(t)}}{u_b\,\widehat{\overline{u_\tau^2}}} = 1, \tag{2.62}$$

or alternatively

$$\frac{\delta\,\widehat{\varepsilon(t)}}{u_b^3} = \frac{f}{2}. \tag{2.63}$$

Equation (2.62) also applies to the LES equations if $\varepsilon(t)$ is replaced by

$$\varepsilon(t) = \langle -T_{ij}\,\widetilde{S_{ij}} + 2\,\nu\,\widetilde{S_{ij}}\,\widetilde{S_{ij}}\rangle, \tag{2.64}$$

where the first and second terms are the subgrid and resolved terms respectively. Figure 2.11 shows the left-hand side (LHS) of (2.62) plotted against Re_b, which has been computed from the LES results for various values of Reynolds number and relative roughness. Included are curves based on the total averaged dissipation and also those based only on the resolved-scale contribution.

The total averaged dissipation term in (2.64) accounts for contributions from regions (I-II), between the actual no-slip walls and the virtual walls, and region (III), the interior LES; see §2.2.4. In region (III), equation (2.64) is used pointwise and integrated over the channel volume. In regions (I-II) below the virtual wall, ε is estimated by approximating the strain-rate tensor $\widetilde{S_{ij}}$ and SGS stress T_{ij} as $d\widetilde{u}/dy$ and $-u_\tau^2$, respectively, leading to the total dissipation contribution from this region, for one wall

$$\int_0^{h_0} \left(-T_{ij}\,\widetilde{S_{ij}} + 2\,\nu\,\widetilde{S_{ij}}\,\widetilde{S_{ij}}\right)\,dy = \int_0^{h_0} \left(u_\tau^2 \frac{d\,\widetilde{u}}{d\,y} + \nu\left(\frac{d\,\widetilde{u}}{d\,y}\right)^2\right)\,dy. \tag{2.65}$$

While the first term of the integral in the RHS of Equation (2.65) has the closed form $u_\tau^2\,u\,|_{h_0}$, the second term is calculated by performing piece-wise integrals over the extent of the linear and log-profiles of mean velocity. The integrands are calculated from the LES using dynamically calculated values of the slip velocity and friction velocity at each wall point. The integrals share a common integration bound, which is calculated as the intercept of the two profiles. Since the log-profile is based on the log-law with Colebrook formula, the intercept varies with ϵ and Re_τ, and thus it is computed through a process of equating the linear relation and the log-relation for each combination of ϵ and Re_τ. In cases where the intercept does not have real solutions ($k^+ > 14$ approximately), the location where the linear and log-profiles are tangent to each other is used as the common integration bound value.

While the region under the virtual wall occupies only 0.5% of δ, it in fact accounts for some $60-70\%$ of the total dissipation. In Figure 2.11, the total calculated dissipation scaled on $u_b\widehat{u_\tau^2}$ is approximately independent of Re_b for all smooth and rough-wall cases. When scaled on u_b^3, agreement with (2.63) is similar to that displayed in Figure 2.11. If the limit $Re_\tau \to \infty$ is taken holding u_b fixed with $\nu \to 0$ then, since the LES and the empirical Moody diagram both support $f \to 0$ for $\epsilon = 0$, it follows that $\widehat{\varepsilon(t)} \to 0$ in this limit.

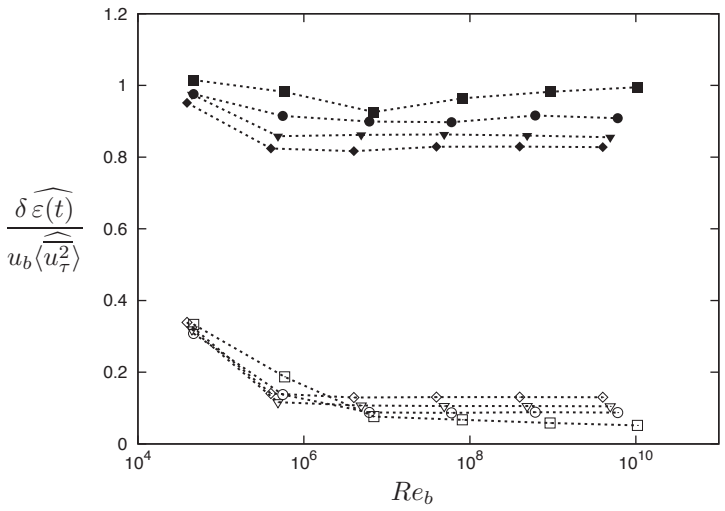

Figure 2.11: Left hand side of Equation (2.62) at various values of roughness ϵ and Reynolds number Re_τ. LES results are for $\{\epsilon : 0, 1\times10^{-4}, 1\times10^{-3}, 5\times10^{-3}\}$ and $\{Re_\tau : 2\times10^3, 2\times10^4, 2\times 10^5, 2\times10^6, 2\times10^7, 2\times10^8\}$. Open symbols denote resolved contributions. Closed symbols denote both subgrid and resolved contributions. Symbol legend: $\square:\ \epsilon = 0$, $\bigcirc:\ \epsilon = 1\times10^{-4}$, $\bigtriangledown:\ \epsilon = 1\times10^{-3}$, $\diamond:\ \epsilon = 5\times10^{-3}$.

2.7 Flow Visualizations

Figure 2.12 illustrates a visualization of the local normalized velocity $\widetilde{u}(x,y)/U_c$ on a wall-normal $x-y$ plane at different roughness heights and at $Re_\tau = 2\times10^6$. Similarly, Figure 2.13 shows the modified velocity deficit $K\left(1-\widetilde{u}\left(x,y\right)/u_c\right)$. Notable in Figure 2.12 is that, while the normalized velocities appear similar near the centerline for all the roughness levels, they are distinctly lower towards the wall when larger roughness is present. This is indicative of increased wall shear stress due to wall roughness. In contrast, this reduction is absent from Figure 2.13, in which the roughness-corrected velocity deficit appears largely independent of ϵ. Recall from §2.5.5 that the velocity deficit profiles collapse in the high Reynolds number asymptotic limit.

Again at $Re_\tau = 2\times10^6$, Figure 2.14 shows the instantaneous and locally determined square of the friction velocity $u_\tau^2(x,z,t)/\overline{u_\tau^2}$ plotted on the bottom physical wall. Note that the color-bar legends are distinct for each plot. By choosing the color-bars to be centered at the mean of each sub-plot data set, the upper and lower bounds can be selected to represent two standard deviations on either side of the mean to highlight the spread of the data. The probability density function (PDF) of $u_\tau^2(x,y)/\overline{u_\tau^2}$ is shown in Figure 2.15-a, where we observe that the spread of the data broadens with increasing roughness. In addition, the long stream-wise oriented streak-like structures in the smooth-wall case (lowest pane) are shortened with increasing roughness. The DNS results of Orlandi & Leonardi [89] have shown a shortening of near-wall ($y^+ \approx 12$) vorticity streaks for several wall roughness types of a 2D and 3D nature. They attribute this effect to the increased intensity of turbulent disturbances produced by the roughness compared to a smooth wall. Despite this qualitative agreement of our results with Orlandi & Leonardi, their roughness height is 20% of the half channel height, with $k^+ \approx 10$, making it difficult to make any direct

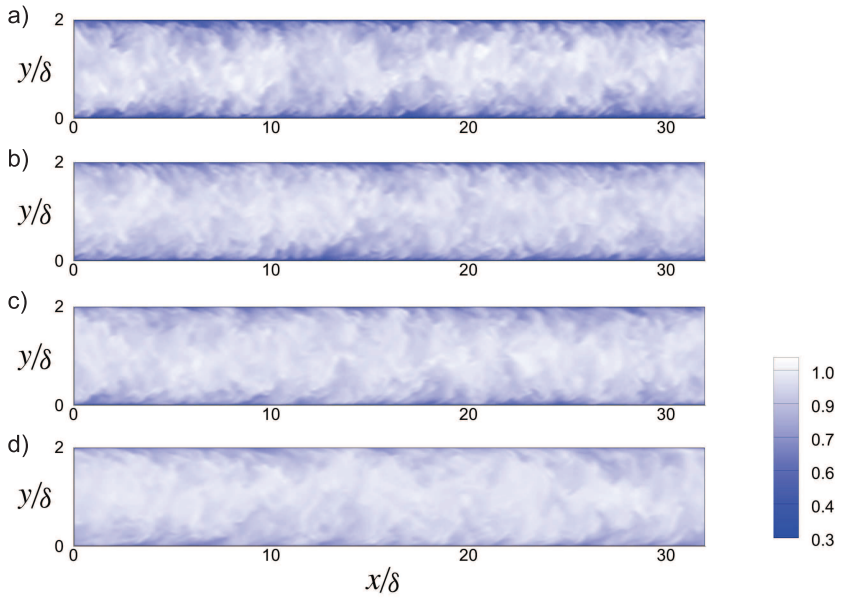

Figure 2.12: Local velocity normalized by centerline velocity $\widetilde{u}(x,y)/u_c$, $Re_\tau = 2 \times 10^6$. Roughness heights from the lower to upper panes are respectively $\epsilon/\delta = 0, 1 \times 10^{-4}, 1 \times 10^{-3}, 5 \times 10^{-3}$.

comparisons with the present results. In a separate DNS study, Flores and Jiménez [32] have observed length-reduction of near-wall streaks and explained the phenomenon as a result of the disturbed near-wall cycle in the buffer-layer caused by the dynamics of the roughness sublayer, where the layer typically extends to 2-5 times the roughness height. However, our virtual wall locates above the buffer layer and we have no direct access to information between the actual wall and virtual wall. Further, the near-wall streaks are known to have span-wise spacing of approximately 100 wall units while the observed friction velocity streaks have significantly larger span-wise spacing, and hence the relation of the observed streak-like structures to the near-wall cycle is unclear. Finally, the instantaneous friction factor fields, $f(x,y) = 2\,u_\tau^2(x,y)/u_b^2$ on the bottom wall are discussed. Owing to our simulation conditions, wherein the mass flow is kept constant, the instantaneous contours of friction factor (not shown) and $u_\tau^2(x,z)/\overline{u_\tau^2}$ (Figure 2.14) show inherent differences in their contour levels but otherwise identical profiles at each roughness level. However, it is apparent in the PDF of the friction factor shown in Figure 2.15-b that the mean value of friction factor is not constant and increases with ϵ, which is expected of the rough-wall cases, as seen in the friction factor plot (Figure 2.2).

2.8 Discussion

The results of the present LES agree with empirical models of the mean-flow velocity and skin friction at large Re_τ and support a stream-wise turbulence intensity that scales on u_τ^2, with logarithmic variation in the outer flow (y/δ) for both the smooth and rough-wall cases, as consistent with Townsend's hypothesis [131]. We therefore use these results to explore the limit $Re_\tau \to \infty$ for both rough and smooth-wall channel flow. For the mean velocity, using Equation

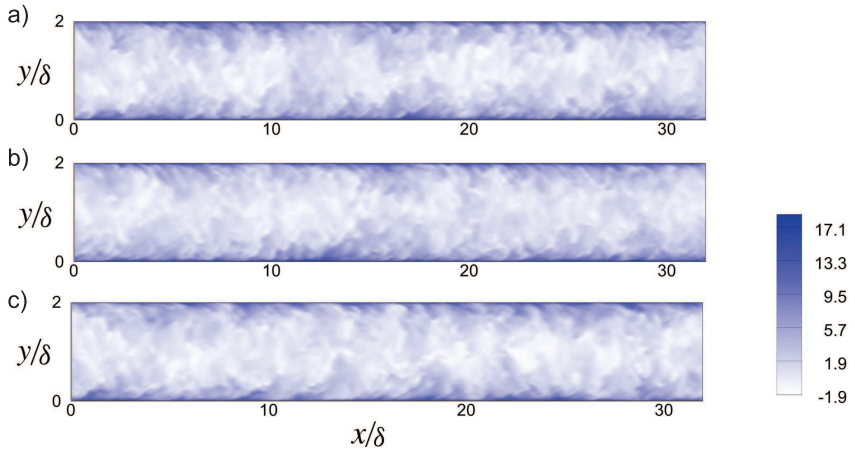

Figure 2.13: Local velocity deficit $K\left(1-\widetilde{u}\left(x,y\right)/u_c\right)$, $Re_\tau = 2\times 10^6$. Roughness heights from the lower to upper panes are respectively $k/\delta = 1\times 10^{-4}, 1\times 10^{-3}, 5\times 10^{-3}$.

(2.43) and (2.44):

$$\left(\frac{u_b}{u_c}\right) = \frac{-\log(1+\alpha\,\epsilon\,Re_\tau)+\kappa\left(B+K_1\right)+\log(Re_\tau)-1}{-\log(1+\alpha\,\epsilon\,Re_\tau)+\kappa\left(B+K_2\right)+\log(Re_\tau)}, \tag{2.66}$$

$$K_1 = \frac{\Pi}{\kappa}\int_0^1 \mathcal{W}(\xi)\,d\xi, \quad K_2 = \frac{\Pi}{\kappa}\,\mathcal{W}(1), \tag{2.67}$$

where u_c is the mean centerline velocity. If ϵ is fixed and $Re_\tau \to \infty$, this has the limit

$$\lim_{Re_\tau\to\infty}\left(\frac{u_b}{u_c}\right) = \begin{cases} \dfrac{\kappa\left(B+K_1\right)-1-\log(\alpha\,\epsilon)}{\kappa\left(B+K_2\right)-\log(\alpha\,\epsilon)} & \text{for} \quad \epsilon \neq 0 \\ \\ 1 & \text{for} \quad \epsilon = 0, \end{cases} \tag{2.68}$$

which suggests limiting plug-flow for the smooth-wall case.

If it is further assumed that, for $0 \leq \epsilon << 1$, the planar-time averaged stream-wise turbulence intensity is bounded above by Equation (2.53) for $0 \leq y/\delta \leq 1$, that is, $\overline{u'^2}/u_\tau^2$ nowhere in the channel exceeds the right-side of Equation (2.53), then the ratio of the total stream-wise turbulence intensity to the square of the bulk velocity in the channel flow is bounded by

$$\frac{\langle u'^2\rangle}{u_b^2} = \frac{\langle u'^2\rangle}{\overline{u_\tau^2}}\,\frac{\overline{u_\tau^2}}{u_b^2} = \frac{f}{2}\left(\beta+|\alpha|+\int_0^1 T(\eta)\,d\eta\right). \tag{2.69}$$

Here, we use $\langle\ \rangle$ to denote the temporal and volumetric average over the flow domain. Since, for $\epsilon = 0$, $f \to 0$ when $Re_\tau \to \infty$ and the integral is expected to be finite, then this is asymptotically zero for $\epsilon = 0$. For any small but finite ϵ the volume-averaged, stream-wise turbulence intensity is expected to remain finite and to scale on f. Substituting Equation (2.47) into the right-hand side of (2.69) gives an approximation for the limiting, average stream-wise turbulent intensity directly in terms of ϵ.

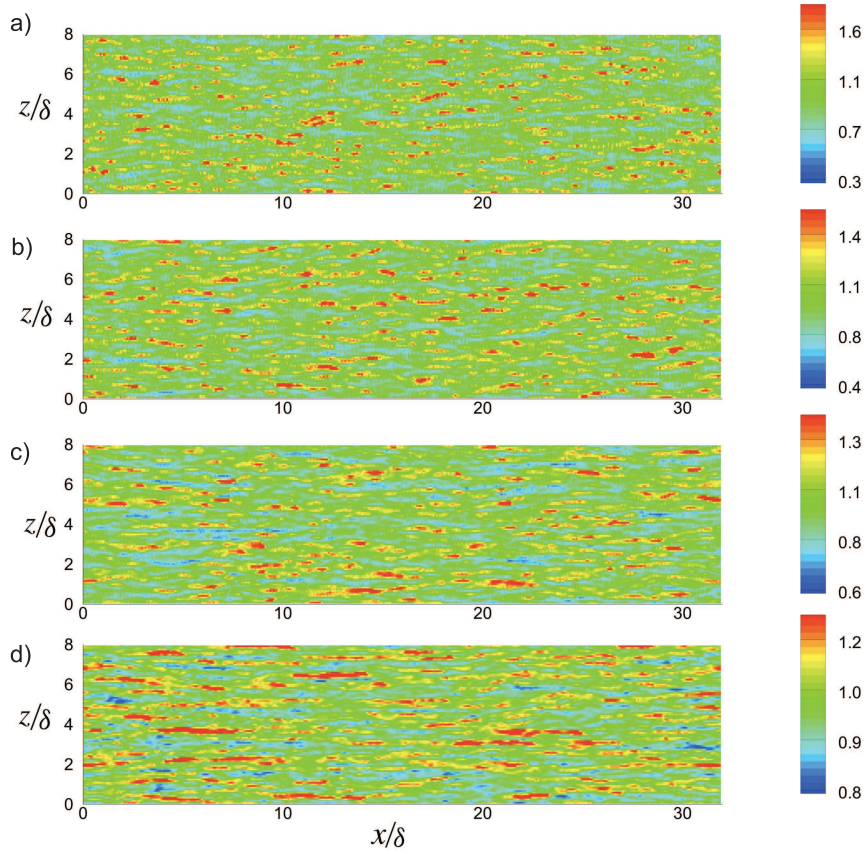

Figure 2.14: Distribution of $u_\tau^2/\overline{u_\tau^2}$ on the bottom wall. (a) $\epsilon = 5 \times 10^{-3}$, (b) $\epsilon = 1 \times 10^{-3}$, (c) $\epsilon = 1 \times 10^{-4}$, (d) Smooth ($\epsilon = 0$).

We note that the present LES cannot resolve the near wall region. The above discussion does not preclude that for $\epsilon = 0$, there exists an inner layer of small thickness, where, for example, $\overline{u'^2}/u_b^2$ could remain finite. When $\epsilon = 0$ in wall-bounded turbulent flow, it is well known that $\overline{u'^2}/\overline{u_\tau^2}$ has a maximum at around $y^+ = 15$. Experimental studies have indicated, at sufficiently large Re_τ in pipe flow, a second maximum for $\overline{u'^2}/\overline{u_\tau^2}$ further from the wall [84, 68]. McKeon & Sharma [73] use a critical-layer argument to infer $y_{II}^+ \sim Re_\tau^{2/3}$ for pipe flow, while Alfredson *et al.* [1] suggest $y_{II}^+ = Re_\tau^{0.56}$.

Let us assume a second peak at $y_{II}^+ = A_1 Re_\tau^a$, where A_1 is constant and $0 \leq a < 1$. It then follows that $y_{II}/\delta = A_1 Re_\tau^{a-1}$, so that $y_{II}/\delta \to 0$, for $Re_\tau \to \infty$ with $\epsilon = 0$. This is not resolved by the present LES. If, however, it is assumed that this peak peels off below Equation (2.53) at $y \sim y_{II}$, then a simple calculation gives the stream-wise turbulent intensity at the second peak as

$$\frac{\overline{u_{II}'^2}}{\overline{u_\tau^2}} = A_2 \log(Re_\tau) + B_2, \tag{2.70}$$

where A_2 and B_2 are constants. According to Equation (2.44), the ratio of u_b/u_τ is proportional to $u_b/u_\tau \sim \kappa^{-1} \log(Re_\tau) + \mathcal{O}(1)$, which is supported by the present LES in Figure 2.2 up to

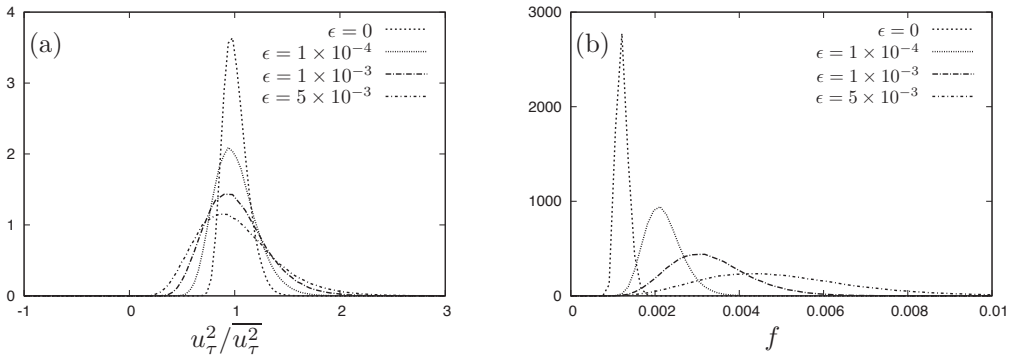

Figure 2.15: Probability density function of (a) friction velocity and (b) friction factor for $Re_\tau = 2 \times 10^5$ and 2×10^6 and $\epsilon = 0, 1 \times 10^{-4}, 1 \times 10^{-3}$, and 5×10^{-3}.

$Re_b = \mathcal{O}(10^{10})$. Therefore, the ratio of $\overline{u_{II}'^2}/\overline{u_\tau^2}$ is proportional to:

$$\frac{\overline{u_{II}'^2}}{u_b^2} \sim 1/\log(Re_\tau). \tag{2.71}$$

Therefore, the ratio approaches zero when $Re_\tau \to \infty$. This simple analysis suggests that, when $Re_\tau \to \infty$, even though the maximum stream-wise intensity (assuming that this is at y_{II}) becomes unbounded relative to u_τ, it is asymptotically zero relative to the outer bulk motion.

For rough-wall flow $\epsilon > 0$, when $Re_\tau \to \infty$, $k_{s\infty}^+ \to \infty$ and all quantities approach finite limits that depend on f and are independent of Re_τ. The present LES, however, uses the Hama roughness function within the wall model. We cannot rule out the possibility, for resolved-scale wall shapes of small slopes for which $\epsilon > 0$ and $k_{s\infty}^+ \to \infty$ but there is no local separation, that a smooth-wall-like limit at $Re_\tau \to \infty$ may be appropriate.

2.9 Summary

Our approach to simulate rough-wall channel flows in LES, with subgrid roughness, has been to implement the stretched vortex SGS model in the outer region, and the wall model [19] has been extended using the Hama roughness correction in the near-wall region. The outer LES calculation has been subject to no direct modifications, while the wall model has been directly modified by the inclusion of roughness. First, the stream-wise momentum equation has been combined with roughness-corrected inner scaling, leading to an ODE to be solved numerically and dynamically for the local u_τ at each point on the wall. Thus, both u_τ and $k_{s\infty}^+$ have been determined dynamically. With u_τ available and assuming that the near-wall region contains attached eddies [87], the velocity profile in the near-wall region has been obtained as a log-relation for smooth walls, which has been corrected for roughness to finally be evaluated at the flat lifted virtual wall and used as a wall boundary condition for the outer LES. When applied to both the ODE and log-relation, these roughness corrections have employed the Colebrook formula, which expresses the downward shift of velocity profiles as a function of equivalent sand

roughness using wall units. The explicit form of the roughness function in this simulation is a model input, and it is possible to employ any given roughness function of the form $\Delta U^+(k_{s\infty}^+)$ or that which can take discrete multi-scale roughness as inputs, that is, $\Delta U^+(k_{s1}^+, k_{s2}^+, k_{s3}^+, ...)$.

Our LES has captured fully developed rough-channel flow in both transitionally rough and fully rough regimes, reaching a maximum bulk velocity based Reynolds number Re_b of order 10^{10}. Our LES results have produced a Moody-like diagram for fully developed channel flow, which has shown favorable agreement with an empirical formula obtained from the log-law, also with the Colebrook roughness correction. The inner-scaled mean velocity profiles have shown collapse on constant values of ϵRe_τ and have exhibited a downward shift compared to the smooth-wall case by an amount depending on $k_{s\infty}^+$. The LES and empirical relation (Equation (2.43)) have been found to be in agreement for each value of ϵRe_τ. The mean velocity profiles have also been plotted in outer-scaled deficit form; in the fully rough regime, it has been shown to collapse onto the universal velocity deficit profile obtained by taking the high Reynolds number limit of the empirical relation, providing a means of empirically acquiring $k_{s\infty}$ in a given geometry.

Our analysis of the turbulent statistics has considered the mean fluctuations of each velocity component as well as the Reynolds shear stress. When including both transitionally and fully rough regimes, weak dependencies on Reynolds number have been observed for all cases. Within the fully rough regime, however, improvements in collapse have been observed for the velocity fluctuations. At very large Reynolds number, it has been observed that the stream-wise turbulence intensities scale on u_τ^2 and δ for both smooth and rough-wall flows, with particularly good collapse for the smooth-wall cases. This is in broad agreement with Townsend's hypothesis. Further more, for both smooth-wall and rough-wall flow in the fully rough regime, the stream-wise turbulence intensities have been noted to follow a $\log(y/\delta)$-profile across almost all of the resolved, outer part of the channel flow. An assumption that these intensities are bounded everywhere by a logarithmic profile has led to the argument that the average stream-wise turbulence intensity is proportional to the friction factor. Based on this argument, we have discussed an infinite Reynolds number flow scenario: when Re_b is extremely large, the aforementioned argument suggests that the total turbulence intensity approaches a finite value, approximated by Equation (2.47) for finite roughness, and zero for smooth-wall flow. The dissipation is also proportional to the friction factor and, when scaled with outer variables, becomes independent of Re_b when Re_b is extremely large. The constant of proportionality is asymptotically zero for smooth-wall flow.

The above suggests that, for smooth-wall flow, the infinite Re_b limit is inviscid slip flow without turbulence across almost the whole channel. In this scenario, the near-wall motion associated with u_τ and its fluctuations decline relative to the centerline velocity as the Reynolds number increases. The detailed small-scale physics of this attenuation are certainly of interest, but are beyond the scope of this work. The indicated infinite Reynolds number limit for rough-wall channel flow shows a universal, roughness corrected, mean velocity deficit profile together with stream-wise turbulence intensities and total energy dissipation that all scale on a finite

friction factor.

Although the present channel setup treats only homogeneous roughness levels at wall surfaces, being smooth everywhere or rough everywhere, owing to the ability of the wall model to assign a roughness level locally and have it be calculated dynamically, it is possible to simulate flows with spatially and temporally varying roughness levels. This sets the stage for the next chapter, wherein the flows over infinitely many transitions between rough and smooth walls are investigated.

Chapter 3

Large-Eddy Simulations of Smooth-Rough-Smooth Transitions in Turbulent Channel Flows

3.1 Introduction

As discussed in Chapter 1, recent experimental evidence of roughness effects appearing in high-Reynolds number canonical wall-bounded turbulent flow has prompted Saito *et al.* [113] to conclude that roughness effects become significant to large-eddy simulation (LES) operating at sufficiently high Reynolds number. Consequently, Chapter 2 studied the roughness and Reynolds number dependence of friction factor and thus produced a Moody-like diagram for channel flow, by incorporating a semi-empirical roughness model into a wall-modeled channel flow LES, which allowed simulations up to $Re_\delta = \mathcal{O}(10^{10})$. In this chapter, the present work builds on Chapter 2 by exploring step transitions from smooth-to-rough ($S \rightarrow R$) followed by rough-to-smooth ($R \rightarrow S$) surfaces in a fully developed turbulent channel flow. Wall geometries such as these are important in areas of micro-meteorology [4, 34], in spoiling of heat exchangers, and in turbine blades with surface degradation or deposits [13, 12, 136]. We refer to these alternating transverse step changes in roughness as roughness "strips," and take advantage of the high Reynolds number capability of our numerical method in a channel flow in order to examine flow responses and trends when various levels of Reynolds number and roughness are encountered by the flow.

In the literature, treatment of a single step change in roughness has traditionally relied on a thermally neutral zero-pressure-gradient, flat plate turbulent boundary layer (ZPGFPTBL), rather than a channel flow, to elucidate the structure and response rates of the perturbed flow. Boundary layer field experiments [14] and wind tunnel work [5, 6, 95, 18] under steady-state conditions reveal that flow encountering a sudden loss of momentum due to a roughness change then sees the formation of an internal boundary layer (IBL) that grows immediately from the location of this change. The height of the IBL δ_i can be determined either through the stream-wise mean velocity [5, 108, 18], stress [118], or through stream-wise turbulent intensities [27].

Detailed findings from several of these studies, including modeled equations for the IBL growth rate, are given in §3.3.4. For the case of a ZPGFPTBL, at any given wall-normal height above the IBL, the flow appears statistically as it would for the upstream wall condition alone except for a slight upward shift of streamlines [6]. Within the IBL, two further layers are observable: a transition layer and an equilibrium layer. The transition layer immediately below δ_i is where flow is affected by both upstream and downstream wall surfaces and where turbulent conditions are transitioning gradually from one equilibrium flow to another. An equilibrium layer is adjacent to the wall up to the height δ_{eq}, wherein the flow is fully adjusted to the new wall state.

Many workers have examined the rates and distances required for flow to adjust towards equilibrium after a step. Quantitatively, an adjustment rate can be examined in a number of direct flow variables such as wall shear stress, mean velocity and turbulent statistics, or indirect quantities such as δ_i, δ_{eq}, or log-law constants. When enough of the direct variables reach a state that no longer has any memory of the upstream step change, a flow can be considered to be fully relaxed. Indeed, one must quantitatively but subjectively select how many variables to consider and what constitutes the signature of transition to this relaxed state in each variable. Relaxation rates and distances may be quite sensitive to the selection of the threshold made, as discussed by Cheng & Castro [18]. The present study reaches consistent trends when exploring each of the following variables: friction velocity, inner- and outer- scaled mean velocity (§1.3.2), and internal boundary layer growth (§3.3.3, §3.3.4).

Several observations in the literature demonstrate firstly that flow after a step and very near the wall relaxes towards equilibrium almost immediately (e.g. Antonia & Luxton[5, 6]; Cheng & Castro[18]; Efros & Krogstad[27]) and secondly, that S→R transitions result in flows that relax more rapidly than R→S flows. A possible exception is Makita [66], who has recorded Reynolds shear stress in both cases as having not relaxed after a distance of 20 δ in a channel flow [128, 14]. Antonia & Luxton [5, 6] have found that boundary layer flows encountering a step from R→S adjust towards equilibrium less rapidly than S→R at $U_\infty\delta/\nu = 1.9 \times 10^4$ and 3.1×10^4, where U_∞ is the free stream velocity. They have shown that the S→R case requires less than 20δ for equilibrium and self-similarity to be restored in the mean flow integral parameters and turbulent intensities, while for their R→S case at $U_\infty\delta/\nu = 2.6 \times 10^4$ and 4.8×10^4, within the extent of their test section of length 16δ, the flow never fully reestablishes equilibrium or similarity. They have suggested that a possible reason for this long "memory" is that in the rough wall flow, a greater proportion of the turbulent energy resides in the larger scale turbulence in the outer layer that is then advected into the flow above the smooth wall. Away from the wall, Jacobs [51] has found that shear stress distributions obtained in the outer part of a channel flow adjust more slowly than those near the wall. This observation is indicative of the slower growth of the equilibrium layer in the outer parts of the flow.

Rather few authors have considered more than one roughness step change. Weng *et al.* [135] have numerically modeled 2-D flow over multiple short strips of roughness. Two transitions, both S→R and R→S transitions, can be created within one flow by introducing a short/impulsive

roughness strip in the flow, which results in two IBL developing after the strip, as demonstrated by Andreopoulos & Wood [4] and Jacobi & McKeon [50, 49]. In between the two IBL's is "stress bore," where the influence of the roughness in the Reynolds shear and normal stresses is found and where the flow is in non-equilibrium [123, 4, 50, 49]. Jacobi & McKeon [50], through their study of static impulsive roughness, have suggested the potential use of impulsive roughness as a tool for flow control, noting that the impulsive roughness affects the spectral energy of the smaller wavelength only. Later, the study has been extended to dynamic impulsive roughness, where the role of the temporal frequency of the impulse has been shown significant [49].

In contrast, the present channel LES utilizes a roughness strip of considerably longer extent (64δ) than the aforementioned studies and this length invites a relaxation towards equilibrium. The majority of workers have examined relaxation rates at only one or two relatively low Reynolds numbers, with many of them being concerned with the non-equilibrium zone immediately after a step and close to the wall. In the present LES we consider a wider range of considerably larger Reynolds numbers and focus on flow responses over the entire domain. The present numerical approach implements spectral techniques that rely on the span-wise periodicity of the channel, and therefore, for given computational resources, the simulation receives a computational benefit such that it allows for a longer stream-wise computational domain to be used. The overall channel flow geometry is advantageous because, far enough downstream from any change in surface roughness, the flow plateaus towards a state that is statistically independent of downstream distance (except close to a downstream transition), making for a more straightforward identification of the relaxed state. We also note that due to the particular numerical wall treatment in our LES, the value of the local wall shear stress is directly available and no further uncertainty is introduced by sampling location or through any indirect calculation.

This chapter investigates sudden roughness changes in channel flow in three main sections. First, the present LES method is expounded briefly in §3.2. This is followed by results and discussion of the mean flow velocity in §3.3.1 and friction velocity in §3.3.2. The stream-wise turbulent intensities and IBL growth rate are discussed in §3.3.3 and §3.3.4. Finally, we present a summary in §3.4.

3.2 Stretched Vortex SGS Model and Roughness-Corrected Wall Model in Spatially Varying Surface Conditions

The full workings of the stretched vortex SGS model and roughness corrected wall model have already been reviewed in Chapter 2, and we refer the reader there for comprehension. In brief, the present strip-roughness channel LES uses the stretched vortex subgrid scale (SGS) model to calculate flow dynamics away from the wall, a region we have thus far been referring to as the "outer" LES. This is distinct from flow dynamics near the wall that are captured by the wall model with roughness correction. Inclusion of surface roughness modifies only the present

wall model, which is responsible for the effect of near-wall fine scales and sets the boundary conditions for the outer LES. Therefore, the flow behaviors observed in the outer LES under rough surface conditions are solely the result of the change in the boundary conditions, which is consistent with the physical picture of flow over rough surfaces.

The numerical implementation relies on the same methodology as before, where the time-integration of the Navier-Stokes, as well as the wall-model ODE, employ a low-storage third-order semi-implicit Runge-Kutta method [125] with a fractional step method at each stage [96, 46].

In what follows, the use of the present LES framework to capture sudden surface-condition changes is discussed. The details of the simulation conditions are given thereafter.

3.2.1 Wall Model with Sudden Roughness Changes

The use of the wall model over abrupt surface condition changes relies on the assumption that the flow up to the first grid adjusts to the new surface condition almost immediately, within one stream-wise grid cell $\Delta x/\delta = 0.083$. This is supported by the findings of Antonia & Luxton [6], who have observed the immediate establishment of a logarithmic velocity profile after the step change from the smooth to rough surface condition. The findings of Cheng & Castro [18] also provide more quantitative support for the assumption. They have observed the equilibrium layer to grow to the top of the roughness sublayer within $166z_0$. Here z_0 is the aerodynamic roughness length scale that satisfies the following equation,

$$u^+ = \kappa^{-1}\log\left(y^+\right) + B - \kappa^{-1}\log\left(1 + 0.26k_{s\infty}^+\right) = \kappa^{-1}\log\left(\frac{y}{z_0}\right). \tag{3.1}$$

Using this relation, the largest value of z_0/δ for our study is approximately 5.0×10^{-5}. According to the empirical relation found by Cheng & Castro, this value of z_0 gives us the estimated stream-wise distance until the equilibrium layer reaches the roughness sublayer as $x/\delta \approx 0.0084$, ten times smaller than the smallest stream-wise grid size.

3.2.2 Strip Roughness Domain and Simulation Conditions

A schematic of our strip-roughness channel is shown in Figure 3.1. The $x-, y-$, and $z-$ directions are stream-wise, wall-normal, and span-wise, respectively. The dimensions and resolutions of the computational domain are $(l_x, l_y, l_z) = (128, 2, 8)\delta$ and $(n_x, n_y, n_z) = (1536, 96, 96)$ respectively. The utility of this resolution has been verified in Chapter 2 in the LES for uniformly rough- and uniformly smooth-wall channel flows at this resolution and also at half this resolution in all three directions. It has been therein demonstrated that, for all Reynolds number and roughness levels considered (including the case of zero-roughness, i.e. smooth), the friction factor obtained in the LES is not sensitive to the LES resolution. A further discussion of resolution effects in the current strip-roughness channel is given in the context of the mean velocity profiles in §1.3.2.

The stream-wise length of each smooth or rough strip is 64δ. The choice of this length aims

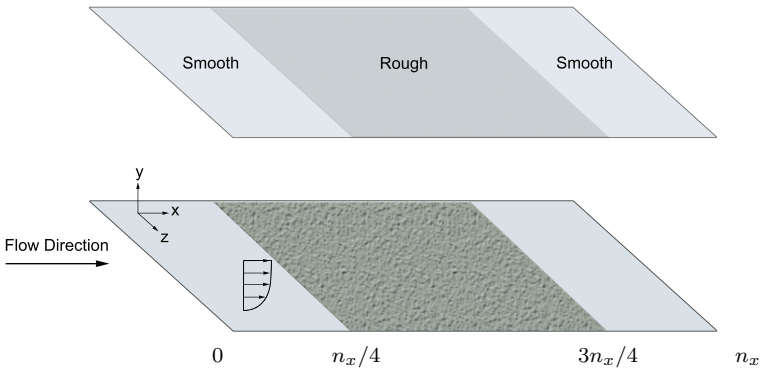

Figure 3.1: Schematic of strip-roughness channel for the LES (Not to scale)

to keep the simulation within computational resource restrictions, and yet facilitate a full flow recovery after each transition. Both top and bottom walls have identical surface conditions consisting of smooth and rough strips. The computational domain is periodic in the stream-wise direction and hence requires a single roughness strip placed at the center of the stream-wise extent, which places the $S \to R$ transition at $x/\delta = 32$ and the $R \to S$ transition at $x/\delta = 96$.

A summary of the simulations is given in Table 3.1. Five channel flows with the aforementioned stream-wise strips are simulated over a range of roughness levels and Reynolds numbers in order to investigate various flow responses to surface changes. The relative roughness, defined as $\epsilon = k_{s\infty}/\delta$, takes the values of $\epsilon = 1 \times 10^{-4}, 5 \times 10^{-4}$, and 1×10^{-3}. The Reynolds number ranges from $Re_\tau = 2 \times 10^4$ to 2.4×10^6. Here, the nominal Reynolds number Re_τ is defined as $Re_\tau = \langle u_\tau \rangle \delta/\nu$, where $\langle u_\tau \rangle$ is the temporal and planar-averaged friction velocity, as will be formally defined subsequently in Equation (3.3). In addition, we include uniformly smooth and rough simulations as "reference" cases [113]. These reference cases have the same bulk velocity u_b as the corresponding roughness strip cases. Note that the bulk velocity u_b is equivalent to the mean stream-wise velocity over any yz-plane, owing to continuity for incompressible flow in a constant yz-plane area channel. The definitions of Reynolds numbers based on $\langle u_\tau \rangle$ and u_b respectively are

$$\begin{aligned} \mathrm{Re}_\tau &= \frac{\langle u_\tau \rangle \delta}{\nu} \text{ where } \langle u_\tau \rangle = \frac{1}{T\, l_x\, l_z} \int_0^T \int_0^{l_x} \int_0^{l_z} u_\tau(x,z,t)\, dz\, dx\, dt, \qquad (3.2) \\ \mathrm{Re}_b &= \frac{u_b \delta}{\nu} \text{ where } u_b = \text{const.} \end{aligned}$$

Here, we also define the temporal- and span-wise averaged quantity:

$$\overline{(\ )} = \frac{1}{T\, l_z} \int_0^T \int_0^{l_z} (\ )\, dz\, dt. \qquad (3.3)$$

	Re_τ	ϵ	$(L_x, L_y, L_z)/\delta$	(n_x, n_y, n_z)	z_0
SRS.1.3	2×10^4	1×10^{-3}	$(128, 2, 8)$	$(1536, 96, 96)$	4.60×10^{-5}
SRS.2.3	2×10^5	1×10^{-3}	$(128, 2, 8)$	$(1536, 96, 96)$	3.95×10^{-5}
SRS.3.1	2×10^6	1×10^{-4}	$(128, 2, 8)$	$(1536, 96, 96)$	3.96×10^{-6}
SRS.3.2	2×10^6	5×10^{-4}	$(128, 2, 8)$	$(1536, 96, 96)$	1.95×10^{-5}
SRS.3.3	2×10^6	1×10^{-3}	$(128, 2, 8)$	$(1536, 96, 96)$	3.90×10^{-5}
SRS.3.1.L	2×10^6	1×10^{-4}	$(128, 2, 8)$	$(1024, 64, 64)$	3.96×10^{-6}
SRS.3.3.L	2×10^6	1×10^{-3}	$(128, 2, 8)$	$(1024, 64, 64)$	3.90×10^{-5}
US.3.0	1.4×10^6	0	$(32, 2, 8)$	$(384, 96, 96)$	N/A
UR.3.1	2.0×10^6	1×10^{-4}	$(32, 2, 8)$	$(384, 96, 96)$	N/A
UR.3.2	2.1×10^6	5×10^{-4}	$(32, 2, 8)$	$(384, 96, 96)$	N/A
UR.3.3	2.4×10^6	1×10^{-3}	$(32, 2, 8)$	$(384, 96, 96)$	N/A
US.3.0.L	1.4×10^6	0	$(32, 2, 8)$	$(256, 64, 64)$	N/A
UR.3.3.L	2.4×10^6	1×10^{-3}	$(32, 2, 8)$	$(256, 64, 64)$	N/A

Table 3.1: Simulation conditions: First letters stand for "Smooth Rough Smooth" (SRS),"Uniformly Smooth" (US), and "Uniformly rough" (UR). The number after the first dot indicates the level of Reynolds number and the second number indicates the level of roughness. The last letter "L" indicates the lower resolution. The value of z_0 is associated with the rough region for the strip-roughness simulations.

3.3 Results and Discussion

3.3.1 Velocity Profiles

In general, flow within the channel responds to a step by undergoing a rapid alteration of its flow field, especially in the vicinity of the wall, and also a propagation of surface effects into the bulk of the flow. Velocity profiles under inner scaling, i.e. $\overline{u}^+(x, y) = \overline{u}(x, y)/\overline{u_\tau}(x)$, are considered in the first subsection below in order to address characteristics of the response near the wall, with the outer region being considered thereafter. The discussion of the mean velocity in the outer region includes a flow visualization of the instantaneous velocity to give a sense of the details found within the flow field and a relaxation length analysis indicating its dependence on roughness and Reynolds number.

Velocity Profiles in the Inner Region

The velocity profiles $\overline{u}^+(x, y)$ are shown at different stream-wise locations in Figure 3.2. We emphasize that $\overline{u}^+(x, y)$ is defined as normalized against the local $\overline{u_\tau}(x)$. Here, the over-bar is defined as the span-wise and temporal averaging, according to Equation (3.3). In each figure, all the profiles are equally spaced 5.3δ apart. At each location, the profile is compared to the uniformly-smooth and uniformly-rough profiles. These reference profiles are obtained in separate uniformly-smooth and uniformly-rough simulations, with the same bulk velocity and hence the same bulk Reynolds number Re_b as the strip-roughness LES. Although the actual computational domain is divided into three regions (upstream smooth (32δ), middle rough (64δ), and downstream smooth (32δ) regions) in Figure 3.2 the two smooth regions are concatenated by making use of the stream-wise periodicity of the domain. The top panel shows profiles in the combined smooth strip and the bottom panel shows those of the rough strip. To show the

most rapid stage of the transition in each panel of the figure, the first profile of panel (a) and the last profile of (b) are separated by one grid cell, i.e. $dx = 0.083\delta$, with the $R \to S$ transition in-between. Similarly, the first profile of the panel (b) and the last of panel (a) are separated by one grid cell and have the $S \to R$ in-between.

First, looking at the profiles in the smooth region, we observe a large deviation of the profile immediately after the $R \to S$ transition except in the vicinity of the wall due to the sudden increase in friction velocity. As discussed in the next section, the mean velocity profile normalized by the bulk velocity at the same location, i.e. profile with no direct effect of the friction velocity, departs from the reference profiles by much less of an amount, which suggests that much of the deviation of the inner scaled mean velocity here is attributed to the change in the friction velocity. This deviation decreases but remains visible downstream until approximately midway into the smooth region. After the midpoint of the strip, the profiles plateau to the uniformly smooth state suggested by the reference profile, and just before the $S \to R$ step, they begin to be affected by the downstream rough region, which causes the profile in the smooth region to be lower than the completely smooth state. Shifting attention to the rough region, the profiles initially have a smaller relative deviation from the reference state than that in the smooth region, although the maximum still occurs immediately after the $S \to R$ transition. Towards the middle of the rough region, the profiles gradually relax and settle down completely to the reference state. Further downstream, it is then affected by the upcoming smooth region, which causes the profile to be higher than the reference profile.

We investigate the effect of resolution on the results by comparing the mean velocity profiles right after each transition, as well as at the center of each region. Shown in Figure 3.3 are the mean velocity profiles at the current resolution and 2/3 of the current resolution. Log-law fits are also included in the plots, with the Karman constant obtained via a linear least squares fit of the profiles at the relaxed states: $\kappa = 0.37$ and $B = 4.5$. A comparison is made at four different points in the domain: right after the $S \to R$, at the center of the rough region, right after the $R \to S$ transition, and at the center of the smooth region. Overall, close agreement is found between the current and lower resolutions at all of the four locations. The maximum discrepancy is found between the profiles right after the $R \to S$ transition, which can be explained by the fact that the differences in the resolution is related to the strength of the discontinuity in the surface transition, and the flow right after the transition is most significantly affected by the discontinuity.

Velocity Profiles in the Outer Region

For the outer flow dynamics, we examine the response of the normalized velocity $\overline{u}(y)/u_b$ vs. y/δ over the transitions, as shown in Figure 3.4. The velocity profiles after both $S \to R$ and $R \to S$ transitions recover to match the reference profiles towards the middle of each strip. Compared to the inner scaled velocity $\overline{u}(x,y)/\overline{u_\tau}(x)$ in Figure 3.2, these outer scaled velocity profiles $\overline{u}(x,y)/u_b$ exhibit to a lesser extent the effect of the downstream surface condition traveling upstream. This

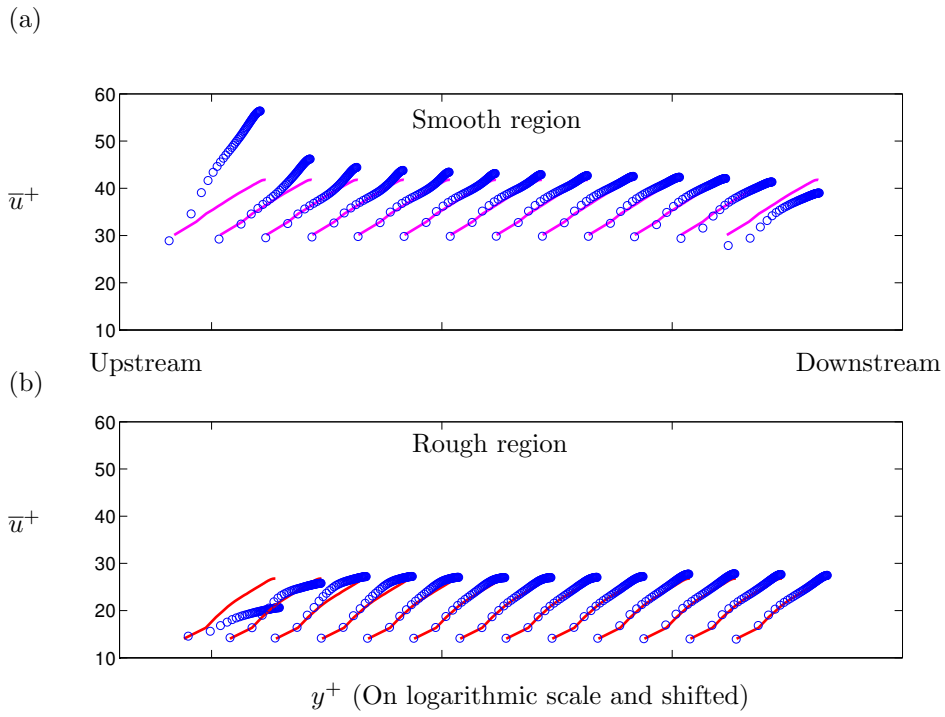

Figure 3.2: Transition of $\overline{u}^+$ vs y^+: (a) profiles over a smooth strip and (b) over a rough strips. Blue symbols: strip-roughness LES, magenta lines: reference profiles from a uniformly smooth channel LES; red lines: reference profiles from a uniformly rough channel LES; all of these have the same bulk velocity. Each profile is 5.3δ apart and shifted horizontally in the figure by one order of magnitude.

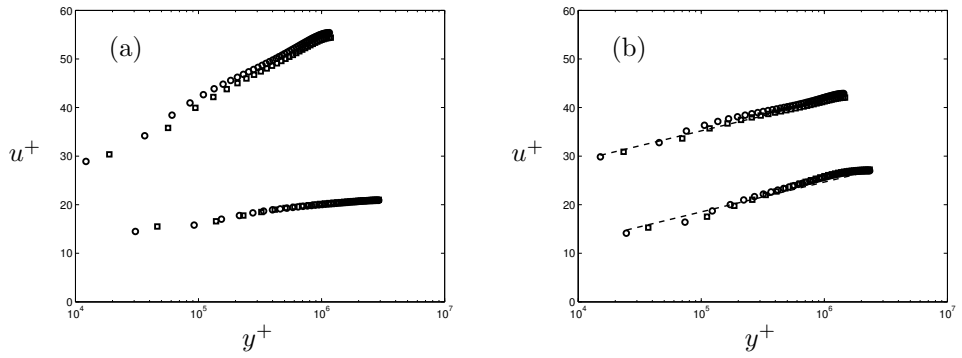

Figure 3.3: Comparison of mean velocity profiles at the current resolution and at 2/3 of the current resolution. Panel (a) shows the profiles right after each transition and panel (b) shows the profiles at the center of each region. Top profiles are in the smooth region and bottom profiles are in the rough region. Open circles: current resolution; squares: 2/3 of the resolution; dashed line: log-law. Flow conditions are $Re_\tau = 2 \times 10^6$ and $\epsilon = 1 \times 10^{-3}$.

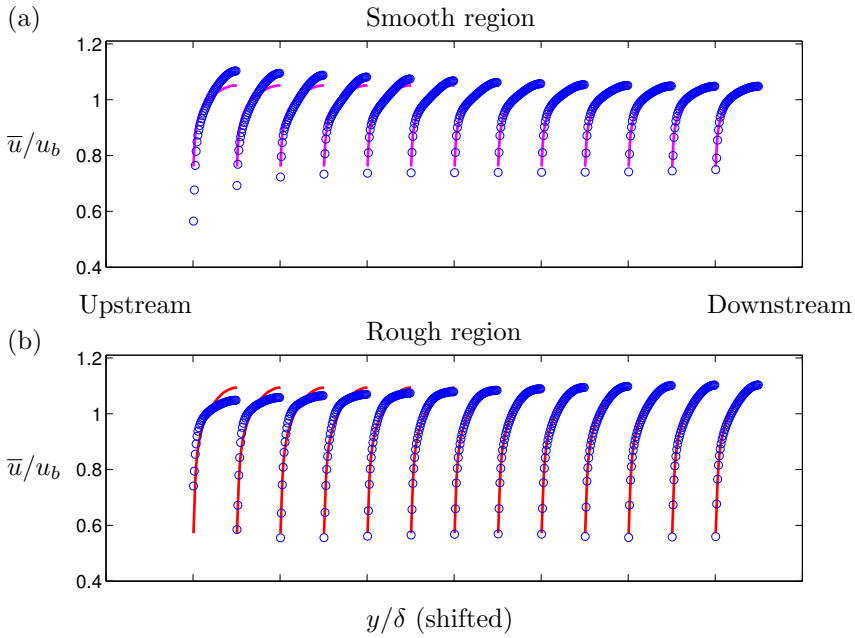

Figure 3.4: Transition of $\overline{u}(y)/u_b$ vs y/δ: (a) profiles over a smooth strip and (b) over a rough strips. Blue symbols: strip-roughness LES; magenta lines: reference profiles from a uniformly smooth channel LES; red lines: reference profiles from a uniformly rough channel LES, all of these have the same bulk velocity. Each profile is 5.3δ apart and shifted horizontally in the figure by one order of magnitude.

is because u_b is not affected by roughness transitions.

Velocity Profiles and Flow Phenomena in the Outer Region

A step change of surface roughness for a turbulent boundary layer (TBL) is characterized by slight deviations of mean streamlines throughout the flow's vertical extent, in keeping with mass conservation [5, 6, 34], but otherwise the mean velocity profile above the IBL of a TBL remains virtually unaffected. This is not the case for an internal geometry such as the present channel flow. To illustrate this, first consider a $S \rightarrow R$ transition in a TBL that abruptly experiences a velocity deficit near the wall as it passes over a roughness step change. To maintain continuity in an incompressible flow, this constitutes a loss of stream-wise mass flux near the wall that requires an equal increase of stream-wise flux further away from the wall. Since the canonical TBL has a semi-infinite vertical extent, such an increase in flux away from the wall is noted only as a slight increase in velocity. Contrast this with a steady channel flow with bulk velocity u_b independent of stream-wise location x. The confined and constant vertical extent then limits the vertical area available away from the wall for the required increase in stream-wise velocity flux. Thus, velocity increases in the outer region are expected to be correspondingly more significant in a channel than in a TBL as a result. We state that such an increase in near-centerline velocity is clearly noted in outer-scaled velocity profiles, which will be discussed in relation to Figure 3.5 below.

The velocity field in the region away from the wall is now discussed by examining contours of

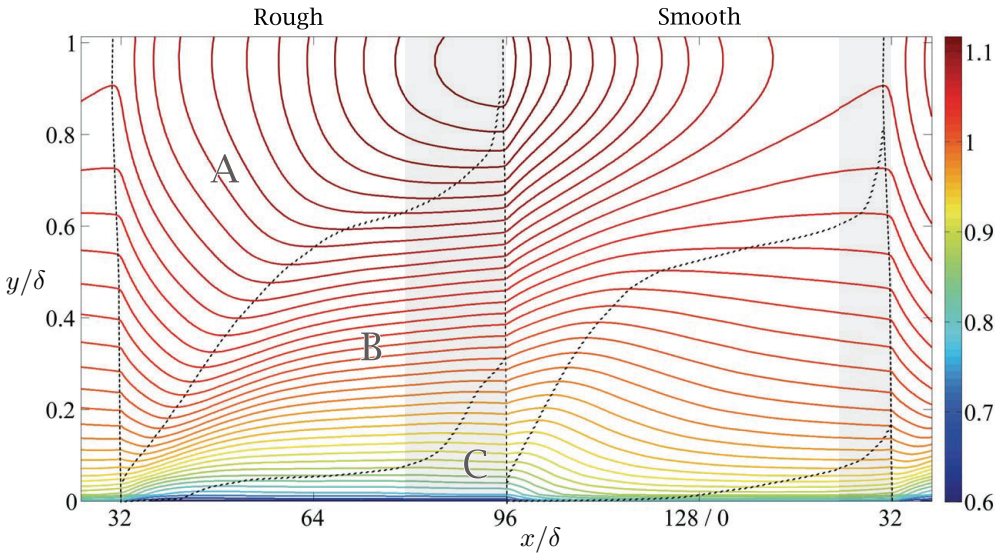

Figure 3.5: Contour of $\overline{u}(x,y)/u_b$ in the bottom half channel. $Re_\tau = 2 \times 10^6$ and $\epsilon = 1 \times 10^{-3}$.

the stream-wise velocity normalized by the bulk velocity, $\overline{u}(x,y)/u_b$, shown in Figure 3.5. The contour plot identifies regions of positive/negative/zero values of $\partial\overline{u}(x,y)/\partial x$ in the flow and illustrates the aforementioned velocity surplus near the centerline. Due to the sensitivity of the contour lines to very small velocity changes, even within the regions where the flow is identified as completely recovered from the view point of the mean velocities, very small flow accelerations and decelerations are still detectable.

In the flow above the rough wall, three regions, A, B, and C, are identified as follows. Region A is where the velocity increases in relation to the velocity at the same vertical location before the transition; Region B is where the velocity decreases; Region C is where the velocity gradient is zero. Dashed lines in the figure have been overlaid to demarcate the boundary between these three regions. We begin by defining the dashed lines marking region boundaries and discuss the phenomena in each region thereafter, noting that similar arguments to those that follow may be applied to the smooth wall case, with most conclusions being the converse.

There are three nearly vertical dashed lines in Figure 3.5 that originate at the wall, beginning at the step changes, $S \rightarrow R$ ($x = 32\delta$) and $R \rightarrow S$ ($x = 96\delta$), and following the start of noticeable "kinks" in the velocity contours. Kinks indicate sharp deviations of velocity, experienced as the flow nears the step. They are associated with high levels of average stream-wise flow gradients $\partial\overline{u}(x,y)/\partial x$ and define the left most boundary of region A. Region B is strictly below region A and separated by a dashed line that rises with distance downstream. It is identified as the locus of points where $\partial\overline{u}(x,y)/\partial x$ first becomes zero as we move downstream from the transition, thus joining the "troughs" in velocity contours over the rough wall. Note that the same definition of the dashed line between equivalent Region A and B applies in the smooth region, but the second

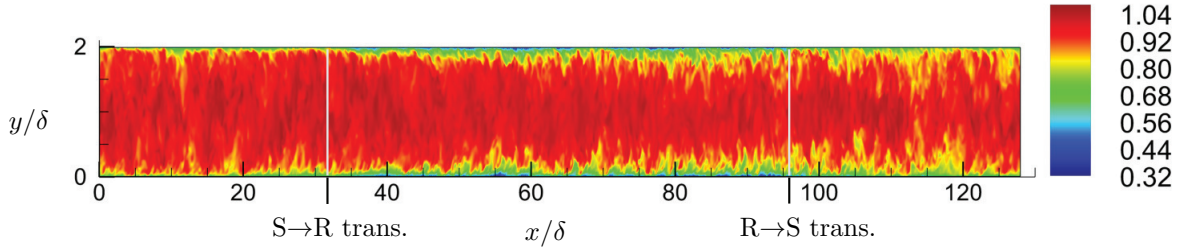

Figure 3.6: Instantaneous stream-wise velocity on a $x-y$ plane.

partial stream-wise derivative at the line is of opposite sign, i.e.

$$\begin{aligned} \frac{\partial \overline{u}(x,y)}{\partial x} &= 0, \quad \frac{\partial^2 \overline{u}(x,y)}{\partial x^2} < 0 \quad \text{for rough-wall region,} \\ \frac{\partial \overline{u}(x,y)}{\partial x} &= 0, \quad \frac{\partial^2 \overline{u}(x,y)}{\partial x^2} > 0 \quad \text{for smooth-wall region.} \end{aligned} \tag{3.4}$$

Region C is strictly below region B and separated by a dashed line that rises with downstream distance. It is defined as the locus of points for which $\partial \overline{u}(x,y)/\partial x$ becomes zero for a second time as we move downstream. The gray shaded regions are where the inner scaled mean velocity starts to be affected by the downstream change in surface condition as observed in Figure 3.2.

Returning to a discussion of phenomena in each region, in region B, the near-wall momentum carried from the smooth region is lost due to an abrupt increase in roughness. This begins locally near the wall but gradually fills the channel. Region C is where the flow has zero acceleration, indicated by the flat contour lines. Faced with an increasingly pronounced velocity deficit across region B and a zero acceleration in C, we are now able to directly observe the idea introduced at the start of the subsection that, by conservation of mass, region A contains a velocity surplus relative to the upstream state.

Velocity visualizations

A sample of instantaneous stream-wise velocity in the strip-roughness channel is shown on an $x-y$ plane in Figure 3.6. Here, the data is taken at $Re_\tau = 2\times10^6$ and $\epsilon = 1\times10^{-3}$ and normalized by the span-wise-averaged centerline velocity $u_c(x,t)$ in order to emphasize the velocity deficit near the wall relative to the centerline velocity due to roughness. That is, the instantaneous velocity ratio $u(x,y,t)/u_c(x,t)$ is plotted on an $x-y$ plane at a constant span-wise location z. Notable in the figure is the increased amount of the near-wall velocity deficit in the rough region, as expected of the rough surface condition. The plot reveals that the effect of the surface condition is convected away from the walls by the flow, forming a larger velocity deficit area in the process.

Relaxation length of the mean velocity

The mean velocity profiles, scaled on both inner and outer variables, reach full relaxation after both $S \rightarrow R$ and $R \rightarrow S$ transitions. Quantitatively, we define a length scale ξ to express

		$S \to R$	$R \to S$
Re_τ	ϵ	λ_1	λ_1
2×10^6	1×10^{-4}	28.5	25.0
2×10^6	5×10^{-4}	31.4	33.3
2×10^6	1×10^{-3}	32.3	34.7

Table 3.2: Relaxation length of mean velocity λ_1 at varying roughness level

		$S \to R$	$R \to S$
Re_τ	ϵ	λ_1	λ_1
2×10^4	1×10^{-3}	13.2	15.2
2×10^5	1×10^{-3}	25.8	27.6
2×10^6	1×10^{-3}	32.3	34.7

Table 3.3: Relaxation length of mean velocity λ_1 at varying Reynolds number

the deviation from the relaxed state by using a measure of the squared difference between the velocity and reference profiles,

$$\xi(x) = \int_0^\delta \left(\frac{\overline{u}(x,y) - u_{ref}(y)}{u_b} \right)^2 dy. \tag{3.5}$$

The quantity $\xi(x)$ should approach zero as the flow after a transition relaxes to a uniformly-rough or smooth condition. Its decay is shown in Figure 3.7, where the upstream and downstream smooth regions are again concatenated. We observe that in both the smooth and rough region the value of ξ decays to less than a few percent of unity right after the transition. Consequently, we introduce a characterisic relaxation length λ_1, defined as the stream-wise distance required for the value of $\xi(x)$ to fall to within a small error bound. Since the asymptotic value of $\xi(x) \to 0$ as $x \to \infty$ and that in addition the normalized velocity integrates to unity, i.e. $\int_0^\delta u_{ref}(y)/u_b dy = 1$, we regard the flow as fully-relaxed when $\xi(x)$ reaches zero with an error bound of 0.2% of unity.

The values of λ_1 are summarized for both smooth and rough regions in Table 3.2 and Table 3.3 at varying roughness level and Reynolds number, respectively. The flows after both $S \to R$ and $R \to S$ transitions show similar trends in their mean velocity relaxation length. The tabulated results indicate that the relaxation length is larger for larger roughness and Reynolds number. Additionally, in general, the relaxation length is longer after the $R \to S$ than $S \to R$ transition. Further, the relaxation lengths are more heavily dependent on Reynolds number than roughness, and across all the Reynolds number and roughness the relaxation lengths range between 10 to 40δ. These results validate our choice of the computational domain length – the stream-wise extent of 64δ for each roughness strip – for achieving full recovery. Any significantly smaller choice of a domain would result in incomplete recovery of the mean velocity within each strip, and thus each time the flow encountered a surface change it would not be from an undisturbed state. In fact, we have attempted to simulate flows encountering roughness strips of one half and one quarter of the current size, i.e. 32δ and 16δ. The flows in shorter domains indeed never reached a recovered state in terms of both the mean velocity and friction velocity.

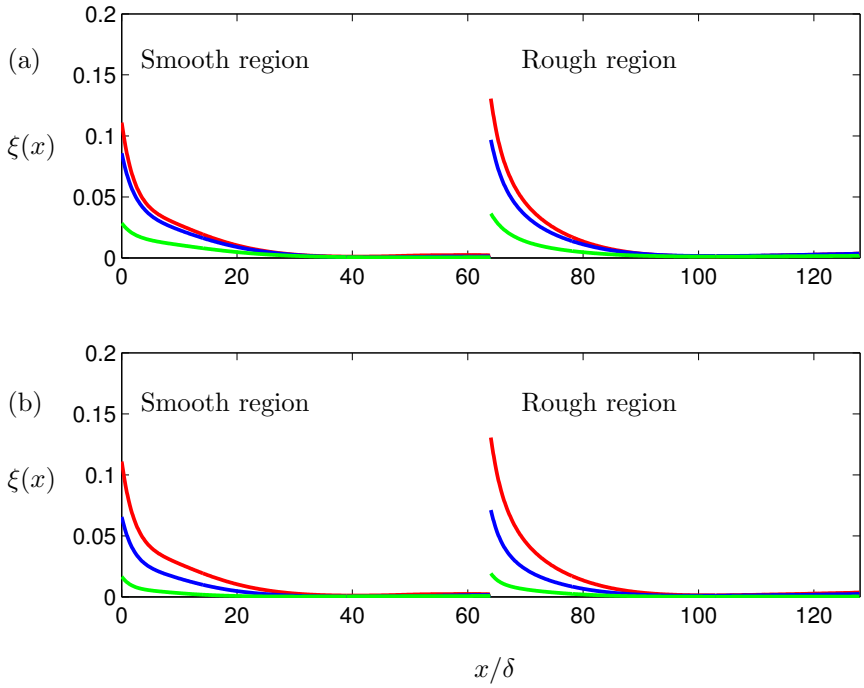

Figure 3.7: Transition of $\xi(x)$ across transitions. Top panel (a): Varying roughness. Red: $\epsilon = 1 \times 10^{-3}$, blue: $\epsilon = 5 \times 10^{-4}$, green: $\epsilon = 1 \times 10^{-4}$. Bottom panel (b): Varying Reynolds number. Red: $Re_\tau = 2 \times 10^6$, blue: $Re_\tau = 2 \times 10^5$, green: $Re_\tau = 2 \times 10^4$.

3.3.2 Friction velocity

The local friction velocity $u_\tau = u_\tau(x, z, t)$ over the smooth-rough-smooth surface is examined. The averaged friction velocity normalized by the bulk velocity $\overline{u_\tau}(x)/u_b$ is considered. As previously defined, the over-bar $\overline{(\,)}$ denotes combined time- and span-wise-averaging. The temporal averages are taken over some time period T, sufficiently long and typically 30-50 convection time units.

The advantage of normalizing the friction velocity by the bulk velocity is that the bulk velocity is constant throughout the channel regardless of the local surface conditions. Therefore, the choice of the normalization factor as u_b allows for isolating the behavior of the friction velocity. The behaviors of $\overline{u_\tau}(x)/u_b$ are discussed over the full range of Reynolds numbers and roughness levels.

First, in Figure 3.8, the profiles of $\overline{u_\tau}(x)/u_b$ are shown at various roughness levels, $\epsilon = 1 \times 10^{-4}, 5 \times 10^{-4}$ and 1×10^{-3}, keeping Re_τ constant at $Re_\tau = 2 \times 10^6$ (SRS.3.1-3). Also included in the figure are the data from the uniformly smooth or rough simulations (US.3.0 and UR.3.1-3) for reference at the corresponding Re_b and ϵ. In the smooth region, the profiles of $\overline{u_\tau}/u_b$ undershoot right after the $R \to S$ transitions, followed by relaxation to a plateaued state. The profiles above the smooth wall collapse well across different levels of roughness in the rough region except in the vicinity of transitions, because the flow is affected by the nearby (downstream) rough regions, each of which has a different roughness level and hence a different level of effect on the upstream flows. Upon encountering $S \to R$ transitions, the flows overshoot

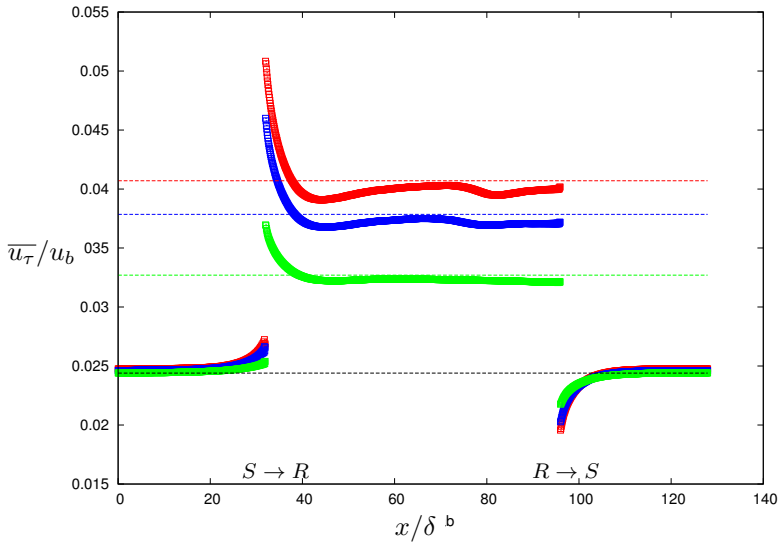

Figure 3.8: Ratio of friction velocity to bulk velocity at $Re_\tau = 2 \times 10^6$ with varying roughness level. Symbols: LES, dashed line: uniformly-smooth or uniformly-rough reference values. Different colors represents different roughness; green: $\epsilon = 1 \times 10^{-4}$, blue: $\epsilon = 5 \times 10^{-4}$, red: $\epsilon = 1 \times 10^{-3}$.

and relax to different values of $\overline{u_\tau}/u_b$ depending on roughness. The collapse that occurred for the smooth region is not observed for the rough region since the varying degrees of roughness naturally result in varying degrees of shear stress at the wall, which has a direct effect on the quantity $\overline{u_\tau}/u_b$.

The observed overshoot at the $S \to R$ transition and undershoot at the $R \to S$ transition are the results of respectively, decelerating and accelerating the flow due to the surface change. Overshoots of this nature at the $S \to R$ followed by gradual relaxation to the rough state are often observed in local wall shear stress measurements in experimental studies, as noted in Elliot[28], Panofsky & Townsend [93], Tani[128], Garratt[34], and Efros & Krogstad[27]. Pendergrass & Arya[95] support both overshoot and undershoot observations, not only in the wall shear stress but also the turbulent intensities. Measurements by Bradley [14] using drag plates indicate an initial overshoot in the wall shear stress of more than double the final equilibrium shear stress state in the S→R case, a result backed by the numerical data obtained by Rao *et al.* [108].

The profile of $\overline{u_\tau}/u_b$ provides behavioral insights into the relaxation of the shear at the wall. In Figure 3.8, a cursory investigation appears to indicate that a steeper gradient right after the $S \to R$ transition is associated with a higher level of roughness. In order to quantify these observations, we consider another length scale that characterizes the $\overline{u_\tau}/u_b$ profiles: characteristic length λ_2 for the immediate response of the flow to the step change. We investigate this quantity in both the cases of a $S \to R$ and $R \to S$ transition. In order to obtain the characteristic length scales, the data of $\overline{u_\tau}/u_b$ between the step and the plateaued state is fitted via least squares with an exponential equation given by

$$\frac{\overline{u_\tau}(x)}{u_b} \equiv S(x) = S_0 + (S_\infty - S_0)\left(1 - \exp\left(-\left(x - x_0\right)/\lambda_2\right)\right), \tag{3.6}$$

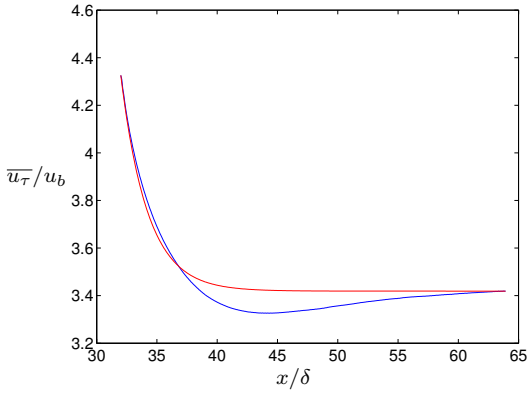

Figure 3.9: Sample fit (red) and LES profile (blue) at $Re_\tau = 2 \times 10^6$ and $\epsilon = 1 \times 10^{-3}$.

		$S \to R$	$R \to S$
Re_τ	ϵ	λ_2	λ_2
2×10^6	1×10^{-4}	2.86	3.85
2×10^6	5×10^{-4}	2.38	3.33
2×10^6	1×10^{-3}	2.17	3.13

Table 3.4: Constant of exponent λ_2 for the ratios, $\overline{u_\tau}(x)/u_b$ up on $S \to R$ transition and $R \to S$ transition at varying roughness levels

where the subscripts $(\ )_0$ and $(\ )_\infty$ denote the normalized friction velocity at the transitions and plateaued state, respectively. A sample fit line is shown along with the LES data line for the case at $Re_\tau = 2 \times 10^6$ and $\epsilon = 1 \times 10^{-3}$ in Figure 3.9. Although the exponential does not capture a secondary overshoot at the local minimum of the LES data, the initial descent of the profiles are in agreement between the fit and LES data, indicating that λ_2 is satisfactory to first order in capturing the length scale of the initial wall shear response upon encountering a $S \to R$ transition. Here, the constant exponent λ_2 is interpreted as the length scale for the initial response and hence a smaller value of this length scale suggests a fast initial response. The values obtained from our LES are tabulated in Table 3.4. The monotonic decrease of the value of λ_2 with roughness is consistent with the observation found in Figure 3.8. The same process has been applied to investigate the $R \to S$ case; decrease of λ_2 with roughness is consistent in our visual inspection of the plot as well as the quantified values in the table.

The results of the friction velocities, shown in Figure 3.8 are indicative of the wall friction's dependence on roughness level. A similar plot, Figure 3.10, is prepared to observe the Reynolds number-dependence, where the roughness is kept constant at $\epsilon = 1 \times 10^{-3}$ while the Reynolds

		$S \to R$	$R \to S$
Re_τ	ϵ	λ_2	λ_2
2×10^4	1×10^{-3}	1.85	2.22
2×10^5	1×10^{-3}	2.12	2.78
2×10^6	1×10^{-3}	2.17	3.13

Table 3.5: Constant of exponent λ_2 for the ratios, $\overline{u_\tau}(x)/u_b$ up on $S \to R$ transition and $R \to S$ transition at varying Reynolds number

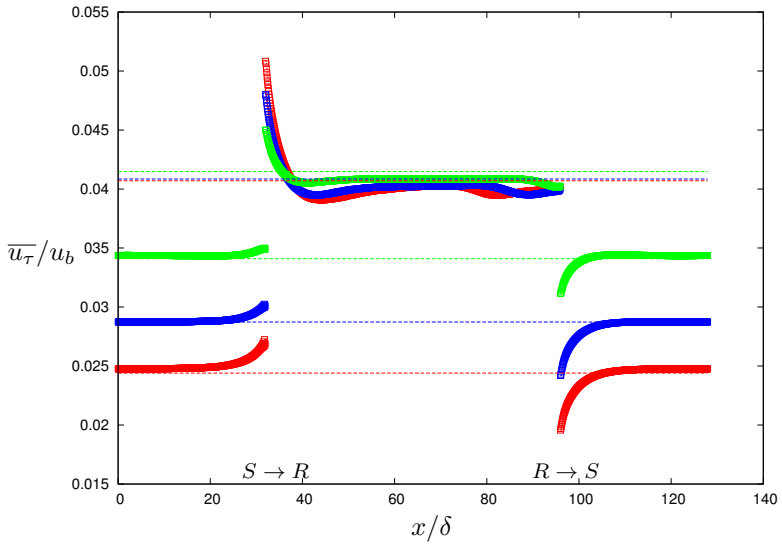

Figure 3.10: Ratio of friction velocity to bulk velocity at $\epsilon = 1 \times 10^{-3}$ with varying Reynolds number. Symbols: LES, dashed line: uniformly-smooh or uniformly-rough reference values. Different colors represents different Reynolds number; green: $Re_\tau = 2 \times 10^4$, blue: $Re_\tau = 2 \times 10^5$, red: $Re_\tau = 2 \times 10^6$.

number is varied over the range $Re_\tau = 2 \times 10^4, 2 \times 10^5$, and 2×10^6. The associated reference profiles are also included in the figure (US.1-3.0 and UR.1-3.3). While the friction velocity profiles depend on Reynolds number in the smooth region, they plateau to approximately the same value in the rough region. In Chapter 2, through LES studies of uniformly rough channel flows, we have observed that at sufficiently high $k^+_{s\infty}$, in particular at values of $k^+_{s\infty}$ considered in Figure 3.10, the flow reaches a fully rough state, exhibiting no Reynolds number dependence in the friction factor. Therefore, the collapse of the profiles in the plateaued rough region of Figure 3.10 suggests that the flow is exhibiting behavior that is characteristic of a fully rough state, and thus should be Reynolds number independent.

In Table 3.5, variations in the length scale, as Reynolds number is increased, appear monotonic for the given data and simulation conditions. For flow after both $R \to S$ and $S \to R$ transitions, a slower initial response is noted when Reynolds numbers increase.

3.3.3 Stream-wise turbulent intensity

The steamwise turbulent intensity $\overline{u'^2}$, span-wise-averaged and normalized by the square of bulk velocity u_b^2, is plotted in Figure 3.11 on $x - y$ plane. Each line represents the intensity at a constant wall normal height. The first three points from the wall are absent from the figure since the model does not capture the intensity accurately at points so close to the wall. The choice of normalizing by u_b rather than the local friction velocity $\overline{u_\tau}(x)$ is motivated by the drastic change that occurs in $\overline{u_\tau}(x)$ over the stream-wise extent that would dominate the $\overline{u'^2}$ field and mask relevant flow features.

Overall, at a given y/δ, much stronger stream-wise fluctuations relative to u_b are noted in the rough region than the smooth region, especially near the wall. This observation is consistent with

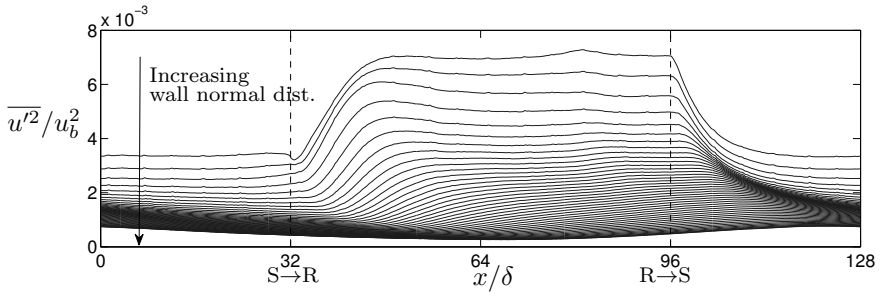

Figure 3.11: Stream-wise turbulent intensity $\overline{u'^2}(x,y)/u_b^2$, span-wise and temporally averaged. $Re_\tau = 2 \times 10^6$ and $\epsilon = 1 \times 10^{-3}$ in the rough region. Each line represents the intensity at a constant wall normal height. The arrow indicates increasing distance from the wall.

Antonia & Luxton [5]. The $\overline{u'^2}$ response to the new surface condition initiates near the wall and downstream of the step change and propagates towards the centerline with downstream distance. However, in each region, the characteristic level of fluctuations, i.e. increased fluctuations in the rough-wall region and decreased fluctuations in the smooth-wall region, becomes prominent only after several channel half-heights downstream of the step change. In comparison to the first order statistics, i.e. the mean velocity profiles, the turbulent intensities, which are a second order statistic, appear to experience a slower adjustment to the step change in surface condition. Similar observations are made by Andreopoulos & Wood [4], who use similar scaling, though a considerably shorter roughness strip.

3.3.4 Internal boundary layer

The development of the IBL has been a key interest among studies of turbulent flows over step changes in surface condition since it indicates the region of modified flow. While the IBL of a TBL is typically defined based on identifying when the mean velocity deviates significantly from upstream flow conditions, such a definition is not applicable for internal flows such as channels and pipes. As discussed in §3.3.1, the outer region of internal flows experiences an immediate velocity change above the step to maintain mass conservation, and the effect can be noted throughout the flow rather than concentrated near the wall. Therefore, the IBL in this study is defined using the stream-wise turbulent intensity $\overline{u'^2}/u_b^2$ by locating the start of the "knee" in the curve formed by the sudden and large change in intensity. The method bears some resemblance to the use of the stream-wise intensities by Efros & Krogstad[27] to locate the knee in their vertical profile. Referring back to Figure 3.11, we notice that beyond a certain height from the wall, the stream-wise intensity lines exhibit a minimum near the $S \rightarrow R$ transition. Observing the very gradual decrease of the intensity before the transition and sudden rise in the intensity after the transition, we can regard the minimum as occurring in the region where a rapid change of flow condition occurs and one which provides a measure of the height of the internal boundary layer. The reverse is true for the $R \rightarrow S$ transition with the knee identified as a maximum of the intensity. Hence we define the height of the IBL $\delta_i(x)$ as the wall normal height where

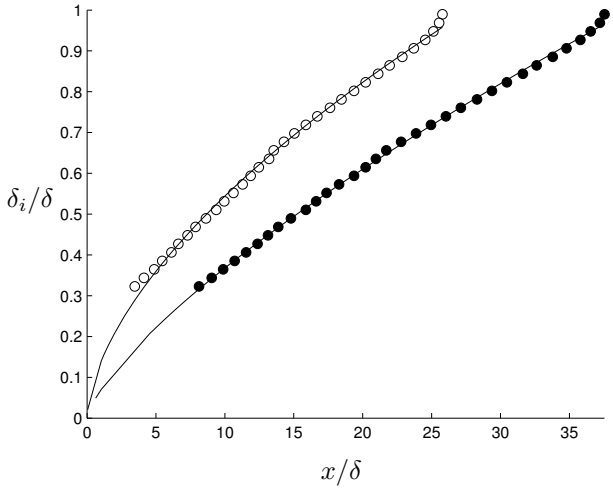

Figure 3.12: Growth of IBL height δ_i versus stream-wise distance from the step change for the case $Re_\tau = 2 \times 10^6$ and $\epsilon = 1 \times 10^{-3}$. Open symbols: after $R \to S$, Filled symbols: after $S \to R$, Lines: fitted power laws.

$$\begin{aligned} \frac{\partial}{\partial x}\left(\frac{\overline{u'^2}}{u_b^2}\right) &= 0 \text{ and } \frac{\partial^2}{\partial x^2}\left(\frac{\overline{u'^2}}{u_b^2}\right) > 0 \text{ for } S \to R \text{ transition}, \\ \frac{\partial}{\partial x}\left(\frac{\overline{u'^2}}{u_b^2}\right) &= 0 \text{ and } \frac{\partial^2}{\partial x^2}\left(\frac{\overline{u'^2}}{u_b^2}\right) < 0 \text{ for } R \to S \text{ transition}. \end{aligned} \tag{3.7}$$

In lieu of the fact that the entire $\overline{u'^2}(x, y)$ field is available to us, we calculate the wall-parallel gradient of the stream-wise intensity at each point in the domain. We then have that the first grid point where the gradient is zero defines the knee.

In the literature, we find experimental evidence that an internal boundary layer will grow proportionally with stream-wise distance raised to a constant power, i.e. $\delta_i/\delta \propto (x/\delta)^n$. Efros & Krogstad[27] report $\delta_i \propto x^{0.73}$ for turbulent boundary layers over an $S \to R$ transition. Antonia & Luxton[5] also report similar values for the growth rate, $\delta_i \propto x^{0.72}$. Here, we use IBL height data obtained by Equation (3.7) to obtain a best-fit power law of the form $\delta_i/\delta = A(x/\delta)^n$, where x is the stream-wise distance from the step, and where n and A are determined constants. In Figure 3.12, two IBLs based on our LES data at $Re_\tau = 2 \times 10^6$ and $\epsilon = 1 \times 10^{-3}$ are shown. We find that the growth of the IBL is approximated by $\delta_i \propto x^{0.70}$ over the $S \to R$ transition, a close agreement with the experimental studies of the aforementioned authors.

For the $R \to S$ transition, this slows to $\delta_i \propto x^{0.58}$. The exponent of the power law fit, $n = 0.58$, indicates that the $R \to S$ case grows less rapidly compared with the $S \to R$ as stream-wise distance grows asymptotically large, an observation that was also made by Antonia & Luxton[6]. Garratt[34] points out that the amount by which the $R \to S$ case is slower than the $S \to R$ case is less significant in atmospheric observations [47] and some semi-empirical observations [118] than that noted in Antonia & Luxton's data ($\delta_{i,R\to S} \propto x^{0.43}$). It is also noted here that the shorter distance for the IBL, which is based on the stream-wise intensities, to reach

		$S \to R$		$R \to S$	
Re_τ	ϵ	A	n	A	n
2×10^6	1×10^{-4}	0.074	0.70	0.16	0.55
2×10^6	5×10^{-4}	0.074	0.70	0.14	0.58
2×10^6	1×10^{-3}	0.070	0.72	0.15	0.58

Table 3.6: Constants A and n for the power law fit $\delta_i/\delta = A(x/\delta)^n$ of the internal boundary layer defined with the stream-wise turbulent intensity at varying roughness level

		$S \to R$		$R \to S$	
Re_τ	ϵ	A	n	A	n
2×10^4	1×10^{-3}	0.096	0.68	0.14	0.62
2×10^5	1×10^{-3}	0.084	0.69	0.14	0.60
2×10^6	1×10^{-3}	0.070	0.72	0.15	0.58

Table 3.7: Constants A and n for the power law fit $\delta_i/\delta = A(x/\delta)^n$ of the internal boundary layer defined with the stream-wise turbulent intensity at varying Reynolds number

the half channel height for the $R \to S$ is a reversed trend compared to the trend observed for the relaxation lengths based on the mean velocities.

The IBL profiles for the remainder of our LES data are presented in Figure 3.13. In order to highlight the Reynolds number and roughness dependence of the IBL growth, the left panel shows the data with constant roughness at varying Reynolds number, while the right panel shows the data with constant nominal Reynolds number and at varying roughness levels. Note that the first several points from the wall are absent from the case at $Re_\tau = 2 \times 10^6$ and $\epsilon = 1 \times 10^{-4}$, because the roughness level is so small that the change of the intensity is very gradual and thus a unique minimum is difficult to distinguish. The values of the leading constant A and exponent n associated with these results are tabulated in Table 3.6 and 3.7. From the plot, we observe a stronger dependence of the IBL profile on the Reynolds number than the roughness, while the table suggests that such a dependence is mainly due to the variation in the leading constant rather than the constant of the exponent.

Motivated by these observations, several scaling factors are investigated in an effort to find a collapse of the IBL profiles for $S \to R$ and $R \to S$ cases. It is found that a good collapse is observed when both the IBL thickness and stream-wise distance are scaled by $\delta/\log(Re_\tau^*)$, as shown in Figure 3.14. Here, the Reynolds number $Re_\tau^* \equiv (\delta u_{\tau,settled})/\nu$ denotes the local Reynolds number at a point where the friction velocity profile has settled. This scaling factor $\delta/\log(Re_\tau^*)$ captures not only the nominal Reynolds number information, which characterizes each simulation as a whole, but also the roughness variation, since $u_{\tau,settled}$ and hence the local Reynolds number in the rough region is dependent on the roughness level. The appearance of scaling on a logarithmic of Reynolds number is common in developing wall-layers and is possibly a dynamical consequence of near-wall structures whose size is roughly proportional to distance from the wall [87].

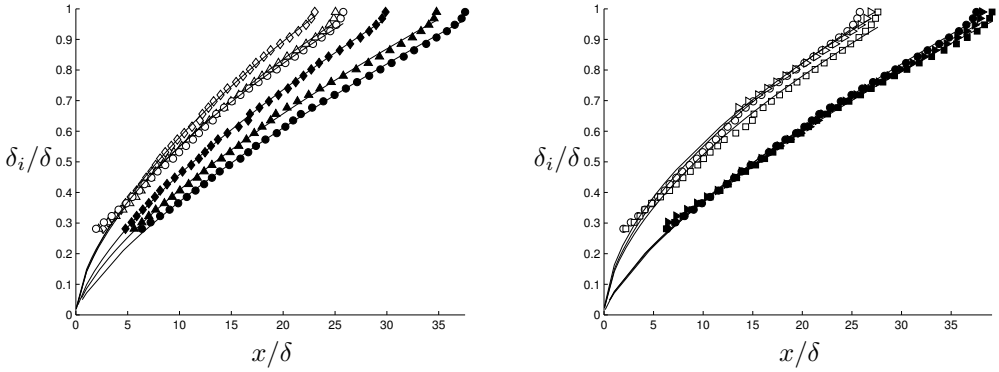

Figure 3.13: Remaining IBLs, open symbols: $R \to S$ and solid symbols: $S \to R$. Left: varying Reynolds numbers with a constant roughness level at $\epsilon = 1 \times 10^{-3}$, circle: $Re_\tau = 2 \times 10^6$, up-facing triangle: $Re_\tau = 2 \times 10^5$, diamonds: $Re_\tau = 2 \times 10^4$. Right: varying roughness levels at a constant Reynolds number at $Re_\tau = 2 \times 10^6$, circle: $\epsilon = 1 \times 10^{-3}$, square: $\epsilon = 5 \times 10^{-4}$, right-facing triangle: $\epsilon = 1 \times 10^{-4}$.

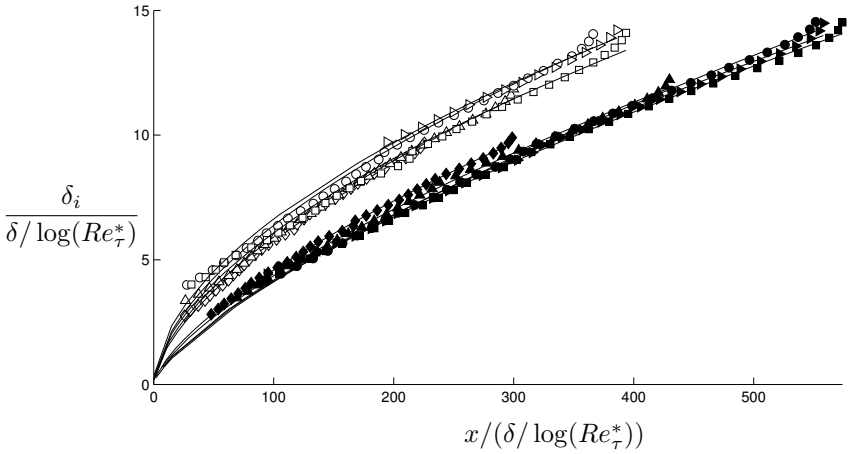

Figure 3.14: Collapse of IBL height δ_i scaled on $\delta/\log(Re_\tau^*)$. Symbols as in Figure 3.13

3.4 Summary and Discussion

We have used large-eddy simulation to examine high Reynolds number turbulent channel flows, up to $Re_\tau = 2.4 \times 10^6$, that encounter wall boundaries with repeated transverse strips of rough- and smooth-surface conditions. Measured stream-wise, strips are 64δ long in a 128δ long channel, which has been shown to be of sufficient length to allow full relaxation of flow parameters to their homogeneously smooth or rough values. Our numerical technique has comprised the stretched vortex model in the outer LES and the wall model near the wall, which are coupled; the outer LES provides the wall model with flow information and the wall model provides the outer LES with a slip boundary condition. The wall model is capable of capturing the dynamics of near wall anisotropic fine scales [19] and accounting for the surface roughness effects [113]. It operates point-wise across wall surfaces, and hence changes in the outer flow can be viewed as a natural response to any temporally and/or spatially variant roughness distribution specified at the wall. Through the wall model, friction velocity $u_\tau(x, z, t)$ is directly available from our computation without the need for typical fitting methods that infer the local wall shear.

Our LES results have indicated that both inner and outer scaled mean velocity profiles recover by approximately the middle of each strip with the recovery length ranging between 10 and 40δ, as obtained by the introduction of a characteristic recovery length scale λ_1. The effects of the downstream transition have been found less significant in the outer flow field, when compared to the region near the wall. Owning to the confined geometry, the present channel has been found to exhibit an initial response after a roughness step that is conditioned by the effect of mass conservation. It has also been found that the mean velocity deficit near the wall due to a rough surface is matched by a region of velocity surplus in the outer flow, and vice versa for the smooth wall.

In the local friction velocity immediately after the step change we have found an overshoot for $S \rightarrow R$ and an undershoot for $R \rightarrow S$ transitions, as noted in several previous studies [28, 93, 128, 34, 27]. An exponential fit of the friction velocity in the region of flow immediately after a step has been used to obtain a characteristic length scale λ_2, which measures the initial recovery rate of the friction velocity. The values of this length scale λ_2 have been observed to be 2-4 δ and to depend on Reynolds number and roughness.

One implication of a substantial velocity surplus away from the wall compared to the relatively small change in the stream-wise turbulent intensity in the same region is that using the mean velocity to define the boundary between modified and unmodified flow, i.e. the internal boundary layer, is inappropriate for internal flows. Using a definition of the internal layer based on the stream-wise changes in $\overline{u'^2}$, we have found for the $S \rightarrow R$ transition an excellent agreement with the power law growth rates of Antonia & Luxton [5] and Efros & Krogstad [27].

We have noted two main differences between the IBL profiles of the $S \rightarrow R$ and $R \rightarrow S$ transitions. First, the asymptotic growth rate is faster for the $S \rightarrow R$ transition than for the $R \rightarrow S$ transition, although within the region that is observed in this study, the effect of the leading constant in the power law fit dominates the growth rate and the IBL develops faster after the $R \rightarrow S$ transition. Second, the variance in the value of the asymptotic growth rate exponent for the $R \rightarrow S$ transition, though it is relatively small, is larger than the $S \rightarrow R$ transition. We have also shown that when the IBL profiles with different Reynolds numbers and roughness levels are scaled by $\delta / \log(Re_\tau^*)$, the profiles collapse well for each of $S \rightarrow R$ and $R \rightarrow S$ transitions.

The results of the present study thus lend support to the capability of the present LES framework to evaluate flows with increased complexity at the high Reynolds numbers encountered in the natural and industrial world. The ability of the wall model and stretched vortex SGS model to evaluate wall roughness locally and hence accurately capture sudden changes in subgrid roughness is a vital step towards realizing flows in generalized geometries. In the final chapter to follow, we initiate an investigation that takes a further step towards this general framework, by moving from a planar walled internal flow to one with cylindrical curvature.

Chapter 4

Large-Eddy Simulation of Fully Developed Turbulent Pipe Flow

4.1 Introduction

Thus far, our investigation of high Reynolds number turbulent flows has explored the effect of surface roughness effects that emerge in practice for flows above a certain Reynolds number, even for highly smoothed industrial surfaces. Here, our investigation takes a different direction; in the future we see the stretched vortex model, wall model, and roughness model being applied to high Reynolds number flows over arbitrary geometries in practice. As a first step towards LES in complex wall shape profiles, we first make the models compatible with a non-planar wall via appropriate coordinate transformations and subsequently introduce them into a pipe flow simulation.

Both smooth and rough-walled pipes have long remained a subject of study, originating in the seminal work of Osbourne Reynolds [110], who built a theoretical foundation for decomposing the mean and fluctuating properties of fluid motion in pipes. Later, in the smooth and rough pipe flow experiments of Nikuradse [88] and Moody [82], an empirical framework has been created for wall skin friction in the presence of turbulence. Since then, turbulent pipe flows have drawn continual attention from the experimental, theoretical, and computational fluid dynamics communities.

Among empirical efforts to understand turbulence, the strong attraction towards pipe geometry has led to much success in expanding knowledge in fully developed turbulent flows with smooth and rough walls. On the other hand, computational efforts have been met with mixed results; an accurate computation technique like direct numerical simulation is only capable of up to $Re_\tau = 2 \times 10^3$ (Hoyas & Jimenez [43]) due to a need for greater computing power, suggesting that DNS is years away from resolving more than a single decade of self-similar scaling behavior [122]. At Reynolds numbers that are three orders of magnitude higher than this, a well validated wall-modeled LES, such as that of Chung & Pullin [19], is one of the few alternatives to DNS and wall-resolved LES that can begin to operate on flows encountered in nature and engineering.

The Chung & Pullin model is successful in high Reynolds number environments, such as

the fully developed rough and smooth channel flow environments presented in Chapter 2 and fully developed boundary layer environments [46]. Presently we expand its applicability to the remaining canonical flow: the fully developed turbulent pipe flow. The model runs optimally at higher Reynolds numbers, and experimental data from the Superpipe facility is readily available in this regime for comparison. Furthermore, the local dynamic friction factor u_τ is directly available from the computation without any need for data fitting or measurement corrections. Drawing on the wall-modeled LES methodology introduced in Chapter 2, implementation of the LES is achieved in a pipe geometry. While the Cartesian-based code used in Chapter 2 and 3 is suitable for planar wall geometries like a channel and TBL, it it cannot be directly applied to pipes or more complex geometries without adaptation. In this chapter, the simulation platform chosen is based on the spectral element method due to superior handling of more general shape of wall-boundaries [56].

The discussion begins with a description of the simulation platform SEMTEX and its spectral element technique, §4.2. Subsequently, preliminary studies in turbulent channel flow in SEMTEX are provided in §4.4 as a proof of concept for the wall-modeled LES within SEMTEX's spectral element solver environment. Assisted by lessons learned in the channel simulations, we then map out our approach to solving the geometry of interest, a pipe flow in §4.5, with results given in §4.6.

4.2 Simulation Platform

Unlike channel flow and boundary layer geometries, which have used the finite difference method with spectral solvers in periodic directions, the pipe LES and wall model are now introduced into a spectral element Navier-Stokes solver, called SEMTEX developed by Blackburn & Sherwin [11].

Previously, Rudman & Blackburn [112] used the SEMTEX system for LES of a pipe flow at Reynolds number $Re_\tau = 1,920$. Its utility lies in its ability to piece together complex geometries that fall outside of the scope of many numerical solvers, all the while carrying low numerical diffusion and dissipation errors. The only requirement of the system is that the geometry contain at least one periodic direction to be used as the Fourier direction. SEMTEX also maintains advantage over some spectral element solvers by being amenable to parallel computation.

The building blocks of a spectral geometry are convex spectral elements that adopt standard Gauss-Lobatto-Legendre nodal basis expansions of n^{th} order. Elements are placed adjacent to one another in a single 2D flat plane [11]. To make up the third dimension, a number of these flat planes containing spectral elements are chosen and stacked equidistant along the Fourier direction.

The reader is referred to the present appendix and also to Blackburn & Sherwin [11] for technical detail on the numerical methods employed to solve the Navier-Stokes equations for spectral geometries. We note that our LES is distinct from theirs in that they use the Smagorinsky SGS

model [121] as well as mesh refinements near the wall that resolve the fine scales. Consequently, they require a van Driest damped turbulent mixing length model to restrict the effects of the SGS model near the wall model. This wall-resolved LES cannot be extended to large Reynolds number. In our LES, we use the stretched vortex SGS model on approximately uniform elements, requiring no empirical wall functions but rather the use of the wall model adapted to a pipe geometry. Further details are expounded in §4.5.1.

With current computing power, any practical implementation of LES at the high Reynolds numbers considered here and on a uniform grid runs under-resolved near the wall and is thus prone to non-negligible discretization errors. In particular, divergence errors are inherent in spectral element discretizations that are used to simulate under-resolved flows, because only C^0 continuity is enforced for field quantities at element edges. This means that, in general, C^1 or higher-order continuity is not guaranteed. Therefore, the derivatives of the field quantities may be discontinuous along element boundaries, an effect amplified at higher Reynolds numbers since the flow gradients in the turbulent flow fields are more intense. Due to low numerical dissipation in spectral element methods in general, oscillations are more intense at element boundaries than at finite difference grid points, and local Reynolds numbers can become artificially raised [11]. Rudman & Blackburn [112] have noted that this can induce spurious eddy viscosity or precipitate other unnatural phenomena. While the errors associated with the lack of C^1 continuity lessens as the flow is more fully resolved, it would defeat the purpose of LES; in LES, where full resolution is not achieved, the absence of C^1 continuity at element boundaries can lead to substantial divergence errors particularly near the wall region. We demonstrate the performance of our wall model and stretched vortex SGS model in the wake of these inevitable divergence errors.

Simulating turbulent pipe flow in practice has required several incremental development stages within the SEMTEX computational environment: in order to ensure the compatibility and validity of the models with the spectral element algorithm, turbulent channel flows have been simulated first, since the models have previously been well validated in this geometry. Subsequently, pipe flows simulation runs have been conducted. Conceptually speaking, the incorporation of the SGS model and the wall model is the same in both channel and pipe geometries, although their actual mathematical development in a pipe geometry differs markedly from that of a channel. While the primary focus of this chapter is turbulent pipe flows, one section is devoted to discussing relevant lessons learned from our channel flow simulations.

4.3 Extension of SEMTEX for LES using the Stretched Vortex SGS Model and Wall Model

The Navier-Stokes solver SEMTEX has been originally developed to conduct DNS and, although it has LES capability, the default configuration is limited to the Smagorinsky SGS model with temporally static boundary conditions. As such, the original code has been further developed to have dynamic boundary conditions that are imposed at the level of the virtual wall. The

stretched vortex SGS model and wall model calculations have been added. Changes to the original code therefore comprise three key modules: subgrid-scale stress calculation, slip velocity calculation and application of the resultant slip boundary conditions. In order to keep the software simultaneously compatible with both DNS and LES implementations, new classes have been created to calculate each of the SGS stresses and slip velocities, and in addition, a new boundary condition applicator class has been developed that is capable of updating boundary conditions at each time step and at any location along the wall surface. In this section, each of these modules is addressed in detail.

4.3.1 Class: Stretched Vortex Model

The stretched vortex SGS model calculation of subgrid stresses is independent of the underlying numerical method, as demonstrated in Chapter 2. A new class named *SGS* has been created to compute the stresses efficiently in a spectral fashion, without losing the capability of running DNS simulations.

An important step towards computing these stresses is to evaluate the second order structure functions by integrating across global coordinate information to obtain the group constant $\mathcal{K}_l$. While the implementation of the stretched vortex model requires global information, the spectral element method requires no such information to solve the Navier-Stokes PDE, and hence one is not by default provided access to global coordinates. The solver relies entirely on the information local to each element, and thus the global coordinate information must be acquired as an additional input to the simulation and it is done within the constructor to minimize computational overhead. Additionally, the constructor pre-defines all the other necessary vectors and matrices that do not change throughout the time-stepping, such as finding the indices of neighboring points. This operation adds particular complexity when pipe flow is implemented via Cartesian formulation, where the mesh is no longer structured. We address this point in detail in §4.5.1.

The remainder of the stretched vortex calculation is done at each time step to compute the subgrid stress matrix $\mathbf{T}(\mathbf{x})$ dynamically. The divergence of this matrix is incorporated into the nonlinear Navier-Stokes term, which results in the time-iterating scheme given by the following sub-steps:

$$r\mathbf{u}^* = -\sum_{q=1}^{J} \alpha_q r\mathbf{u}^{n-q} - \Delta t \sum_{q=0}^{J-1} \beta_q r \left(\mathbf{N}\left(\mathbf{u}^{n-q}\right) + \nabla \cdot \mathbf{T}\right) \tag{4.1}$$

$$r\nabla^2 p^{n+1} = \frac{\rho}{\Delta t} r\nabla \cdot \mathbf{u}^*, \tag{4.2}$$

$$r\mathbf{u}^{**} - r\mathbf{u}^* = -\frac{r\Delta t}{\rho}\nabla p^{n+1}, \tag{4.3}$$

$$r\nabla^2\mathbf{u}^{n+1} - \frac{r\alpha_0}{\nu\Delta t}\mathbf{u}^{n+1} = -\frac{r}{\nu\Delta t}\mathbf{u}^{**}, \tag{4.4}$$

where the pressure boundary condition is given by

$$r\partial_n p^{n+1} = -r\rho\mathbf{n}\cdot\sum_{q=0}^{J-1}\beta_q\left(\mathbf{N}\left(\mathbf{u}^{n-q}\right) + \nu\nabla\times\nabla\times\mathbf{u}^{n-q} + \partial_t\mathbf{u}^{n-q}\right). \tag{4.5}$$

Here, J is the order of accuracy of the scheme, and the constants α_q and β_q are the discrete weights associated with the current order of accuracy $J = 2$. The nonlinear terms are denoted as $\mathbf{N}(\mathbf{u})$ and defined as the skew-symmetric form, i.e. $\mathbf{N}(\mathbf{u}) = (\mathbf{u}\cdot\nabla\mathbf{u} + \nabla\cdot\mathbf{uu})/\mathbf{2}$. A complete discussion of the numerical methods for DNS cases is given in Blackburn & Sherwin [11], as well as in the appendices of Chapter 6.

4.3.2 Class: Wall Model

A new class *Wall Model* houses the computation of slip velocities using the wall model ODE and log-relation. Presently we use the same local wall model, Equations (2.17) and (2.21), used for the previous channel flow LES but without the roughness correction, and adapted here for the pipe-flow geometry. Rather than the formulation for the ODE (2.17) for u_τ, however, it is presently convenient to utilize the equivalent ODE form originally used by Chung & Pullin [19] in terms of the wall-normal shear stress at the wall.

$$\frac{\widetilde{u}|_h}{2\eta_0}\frac{\partial\eta_0}{\partial t} + \frac{\partial\langle\widetilde{uu}\rangle}{\partial x}\bigg|_h + \frac{\partial\langle\widetilde{uw}\rangle}{\partial z}\bigg|_h + \frac{1}{h}\widetilde{uv}|_h = -\frac{\partial\widetilde{P}}{\partial x}\bigg|_h + \frac{\nu}{h}\left(\frac{\partial\widetilde{u}}{\partial y}\bigg|_h - \eta_0\right), \tag{4.6}$$

$$\widetilde{u}\,|_{h_0} = u_\tau\left(\frac{1}{\mathcal{K}_1}\log\left(h_0^+\right) + B\right), \tag{4.7}$$

where we recall that $u_\tau^2 = \nu\eta_0$. Here, the stream-wise, wall-normal, and span-wise directions are set as $x-, y-, z-$directions, which reflects the actual implementation of channel flow in SEMTEX. In the channel flow simulations of Chapter 2 and 3, the wall model is implemented in a synchronized manner with the Navier-Stokes time-stepping because it uses the third-order Runge Kutta method for time-integration, thus providing complete flow information at three sub-steps within each time increment. This allows for integrating the wall model ODE numerically with third-order accuracy. In contrast, the time-stepping scheme used in SEMTEX provides flow information only once in each time-step, resulting in a first order approximation to the ODE if solved numerically. Due to highly fluctuating behaviors of the near-wall flows, the use of this first order numerical solution to solve the ODE has caused unstable behaviors to emerge in solutions. Therefore, we have used an approximate analytic solution of first order to the wall ODE [19]. For the Cartesian coordinate system, the ODE in Equation (4.6) can be rewritten in the form:

$$\frac{\partial \eta_0}{\partial t} = \Lambda \eta_0 \left(\gamma - \eta_0\right), \tag{4.8}$$

where $\Lambda(t)$ and $\gamma(t)$ are defined as

$$\Lambda(t) = \frac{2\nu}{hw|_h}, \tag{4.9}$$

$$\gamma(t) = -\frac{h}{\nu}\left(\left.\frac{\partial\langle\widetilde{uu}\rangle}{\partial x}\right|_h + \left.\frac{\partial\langle\widetilde{uw}\rangle}{\partial z}\right|_h + \frac{1}{h}uv|_h + \left.\frac{\partial\widetilde{P}}{\partial y}\right|_h\right) - \left.\frac{\partial u}{\partial y}\right|_h. \tag{4.10}$$

The formal analytic solution to Equation (4.8) is (Chung & Pullin, 2009)

$$\frac{1}{\eta_0(t)} = \frac{I(t)}{\eta_0(0)} + I(t)\int_0^t \frac{\Lambda(s)}{I(s)}ds, \tag{4.11}$$

where

$$I(t) = \exp\left(-\int_0^t \Lambda(s)\gamma(s)ds\right). \tag{4.12}$$

For the purposes of solving the ODE, the function $\Lambda(t)$ and $\gamma(t)$ can be considered functions of time sourced from information supplied by the LES at y=h. Equation (4.11) is approximated to first order to obtain Equation (4.13) in the implementation:

$$\frac{1}{\eta_0(t)} = \frac{1}{\eta_0(0)}e^{-t\Lambda(0)\gamma(0)} - \frac{1}{\gamma(0)}\left(1 + e^{-t\Lambda(0)\gamma(0)}\right). \tag{4.13}$$

4.3.3 Adaption of Wall Model to Cylindrical Geometry

For the cylindrical coordinate system, the wall model ODE, as well as the analytic solution, must be modified through coordinate transformation. This involves calculating the wall-normal components and wall-normal derivatives of variables at each wall point. Since the transformation takes place at each wall point and at each time step, and evaluates many trigonometric functions, it increases the computational cost substantially. However, all the multiplication factors associated with the transformation are computed only once when objects are constructed and stored as a private member of the class before time stepping begins.

As will be introduced in §4.5.1, we implement the turbulent pipe flow simulation with the stream-wise direction being the Fourier direction, making the pipe transverse-cross-section the Fourier plane. Fourier planes are meshed in Cartesian coordinates, and hence the ODE must be rewritten in cylindrical coordinates. First, wall-parallel filtering and wall-normal averaging are re-defined in cylindrical coordinates as,

$$\widetilde{\phi}\left(z, r, \theta, t\right) = \int\int \phi\left(z', r, \theta', t\right) G\left(z - z'; \Delta_f\right) G\left(\theta - \theta'; \Delta_f\right) dx' d\theta', \tag{4.14}$$

$$\langle\widetilde{\phi}\rangle\left(z, \theta\right) = \frac{1}{h}\int_{R-h}^{R} \widetilde{\phi}\left(z, r, \theta\right) dr. \tag{4.15}$$

Here, the stream-wise, radial, and azimuthal directions are denoted by $z-, r-, \theta-$ directions, again to be consistent with the coordinate system used in the current pipe flow simulation.

Applying the above filtering and averaging processes to the stream-wise momentum equation in cylindrical coordinates, the following ODE of the stream-wise velocity is obtained:

$$\frac{\partial\langle\widetilde{w}\rangle}{\partial t}+\frac{\partial\langle\widetilde{ww}\rangle}{\partial z}\bigg|_{R-h}+\frac{1}{R}\frac{\partial\langle\widetilde{wu_\theta}\rangle}{\partial\theta}\bigg|_{R-h}+(\frac{1}{R}-\frac{1}{h})wu_r|_{R-h}=-\frac{\partial\widetilde{p}}{\partial z}\bigg|_{R-h}+\frac{\nu}{h}\left(\frac{\partial\widetilde{w}}{\partial r}\bigg|_{R}-\frac{\partial\tilde{w}}{\partial r}\bigg|_{R-h}-\frac{1}{R}w|_{R-h}\right). \tag{4.16}$$

Note that since the outer LES runs on Cartesian coordinates, most terms in Equation (4.16) must be transformed from Cartesian to cylindrical coordinates. Through several stages of algebra, we obtain the wall model ODE in cylindrical coordinates,

$$\begin{aligned}\frac{\partial\eta_0}{\partial t}=&\frac{2\eta_0}{u|_{R-h}}\left[-\frac{\partial\langle\widetilde{ww}\rangle}{\partial z}\bigg|_{R-h}\right.\\&-\frac{1}{R}(r\sin^2\theta\frac{\partial wu}{\partial x}-r\sin\theta\cos\theta\frac{\partial wu}{\partial y}-r\sin\theta\cos\theta\frac{\partial wv}{\partial x}+r\cos^2\theta\frac{\partial wv}{\partial y})\bigg|_{R-h}\\&+\frac{1}{h}(wu\cos\theta+wv\sin\theta)\bigg|_{R-h}\\&-\frac{\partial\widetilde{p}}{\partial z}\bigg|_{R-h}\\&\left.+\frac{\nu}{h}\left(-\eta_0-(\frac{\partial w}{\partial x}\cos\theta+\frac{\partial w}{\partial y}\sin\theta)\bigg|_{R-h}-\frac{w|_{R-h}}{R}\right)\right].\end{aligned} \tag{4.17}$$

The ODE can be written as in Equation (4.18) by defining $\Lambda(t)$ and $\gamma(t)$ as Equation (4.19) and (4.20) respectively.

$$\frac{\partial\eta_0}{\partial t}=\Lambda\eta_0\left(\gamma-\eta_0\right), \tag{4.18}$$

where

$$\Lambda(t)=\frac{2\nu}{hw|_{R-h}}, \tag{4.19}$$

$$\gamma(t)=-\frac{h}{\nu}\left(\frac{\partial\langle\widetilde{ww}\rangle}{\partial z}\bigg|_{R-h}+\frac{1}{R}\frac{\partial\langle\widetilde{wu_\theta}\rangle}{\partial\theta}\bigg|_{R-h}+(\frac{1}{R}-\frac{1}{h})wu_r|_{R-h}+\frac{\partial\widetilde{P}}{\partial z}\bigg|_{R-h}\right)-\frac{\partial w}{\partial r}\bigg|_{R-h}-\frac{w|_{R-h}}{R}. \tag{4.20}$$

The approximated analytic solution to this ODE is obtained via first order approximations.

$$\frac{1}{\eta(t)}=\frac{1}{\eta(0)}e^{-t\Lambda(0)\gamma(0)}+\frac{1}{\gamma(0)}(1-e^{-t\Lambda(0)\gamma(0)}). \tag{4.21}$$

4.3.4 Temporally and Spatially Varying Dirichlet Boundary Conditions

The slip velocity is calculated locally and dynamically, which requires the ability to apply the time- and space-varying Dirichlet boundary conditions. While the original implementation of

SEMTEX allows various boundary conditions, such as constant Neumann or Dirichlet boundary conditions, a new boundary applicator to allow for variations in time and space has been developed for the purpose of implementing the wall model. To achieve this, we have created a new boundary condition type as well as a new boundary condition manager.

The boundary condition type, such as Neumann and Dirichlet boundary conditions, is specified for each element adjacent to the boundaries in the session file; for a complete description of the session file, the readers are referred to the SEMTEX documentation. With the original platform, based on input information about boundary condition type and values, the boundary conditions are specified at the beginning of the simulation since there is no mechanism for updating the boundary conditions during the time-stepping. With the modified platform, if the boundary condition type is specified as type "T" for "time and space varying," the boundary value assignment takes place during the simulation via"Slip Velocity Boundary Condition Manager," which is responsible for taking in the slip velocity to be applied, updating the boundary condition storage and assigning each element with the updated slip velocity. The utility of the temporally and spatially varying boundary conditions is not limited to a particular type of wall modeling or the use of wall modeling at all. For example, if the wall model is replaced with another model, only the class *Wall Model* must be altered; the resultant slip velocity can be fed into the slip velocity boundary condition manager and application of the slip velocity is correctly carried out. As we have demonstrated in Chapter 3, the user may wish to have spatially and/or temporally varying boundary conditions built into the design, in which case such changes can be easily reflected via the new boundary condition type.

4.4 Test Case: Fully Turbulent Channel Flow in SEMTEX

4.4.1 Channel Flow Simulation Conditions

We have simulated fully developed smooth wall turbulent channel flow with the stretched vortex model and wall model in SEMTEX using the same formulation as presented in Chapter 2. This provides the opportunity to verify that the models function well when used with the spectral element method. Results are presented for $Re_\tau = 2 \times 10^3 - 2 \times 10^6$. The domain size is $(l_x, l_y, l_z) = (15, 2, 8)\delta$, where δ is the half channel height and $x, y, z-$directions are the stream-wise, wall-normal, and span-wise directions, respectively. The Fourier direction is chosen as the span-wise direction and in contrast with regular grid-based methods, the resolutions are characterized not simply by the number of grid points, but firstly via the number of planes in the Fourier direction, secondly by the number of elements in each $x - z$-plane, and finally on the chosen order of polynomials basis functions. We have used 48 Fourier planes, each with four elements in the wall-normal direction and 30 elements in the stream-wise direction. Each element is represented in both wall normal and stream-wise directions with a 9^{th} order polynomial basis.

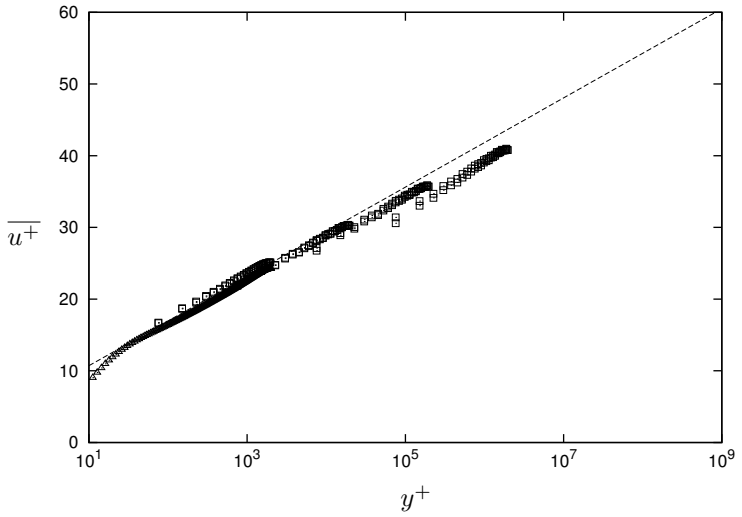

Figure 4.1: Mean velocity profiles of channel flow with SEMTEX. Squares: LES, triangles: DNS of Hoyas & Jimenez [43], dashed line: log-law with $\kappa = 0.37$ and $B = 4.5$, obtained from Chapter 2.

4.4.2 Channel Flow Results

The mean velocity profiles obtained at Reynolds number $Re_\tau = 2 \times 10^3 - 2 \times 10^6$ are shown in Figure 4.1. An agreement is observed between LES and DNS results, while the log-law also supports our LES results. For the log-law reference profile, the values of the Kármán constant κ and additive constant B are $\kappa = 0.37$ and $B = 4.5$, which have been obtained from Chapter 2. At $Re_\tau = 2 \times 10^6$, we start to see a deviation of the LES profiles from the log-law, suggesting the onset of non-negligible effects from divergence errors.

The stream-wise turbulent intensities over the same range of Reynolds number are shown in Figure 4.2. The scolloping effect observed in the profiles coincides with the locations of element edges and is believed to be an effect of divergence error, to be discussed subsequently. Although there are some variations across different Reynolds numbers, overall the profiles agree well with the experimental results of Hoyas & Jiménez [43].

A crucial finding of this high Reynolds number channel simulation test case is the significant effect of domain size. Initially, a domain size of $(l_x, l_y, l_z) = (2\pi, 2, \pi)\delta$ had been used. However, the flow fields developed an asymmetry in the mean profiles when the expectation was for them to be symmetrical across the centerline. In such cases, we found a large spike in the pressure field at the "highest pressure node." Its presence may be understood by recalling that one of the fundamental flow assumptions here is that of incompressibility. The continuity condition in incompressible flow sets up the pressure Poisson equation with Neumann boundary conditions, and solutions of such problems are generally non-unique. Consequently, the local value of the pressure is undetermined and only the local pressure gradient has meaning. In order to resolve this non-uniqueness of the pressure, a small amount of Dirichlet boundary condition is introduced by fixing the pressure at one point in the domain boundary, the "highest pressure node." It is thought that pinning the pressure at the highest pressure node and imposing periodicity within

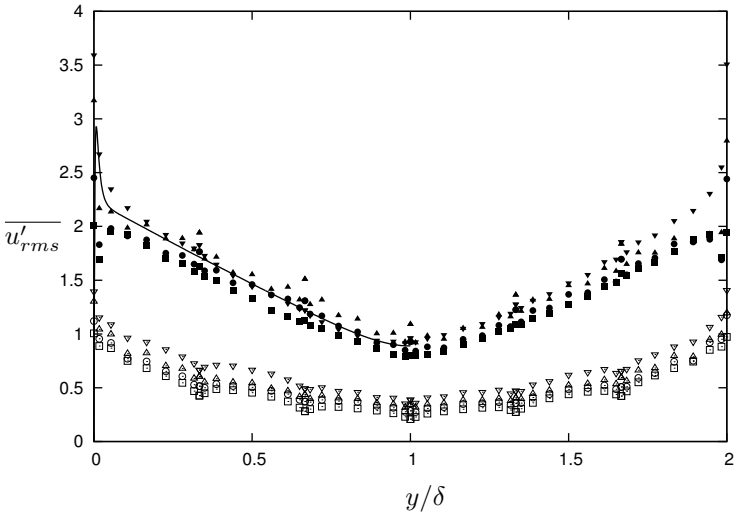

Figure 4.2: Turbulent statistics normalized by u_τ and δ. Solid symbols: total component, open symbols: subgrid component, line: DNS data of Hoyas and Jiménez 2006. Square: $Re_\tau = 2 \times 10^3$, circle: $Re_\tau = 2 \times 10^4$, up-pointing triangle: $Re_\tau = 2 \times 10^5$, and down-pointing triangle: $Re_\tau = 2 \times 10^6$.

such a small domain resulted in unphysical phenomena, ultimately manifesting in an asymmetric profile across the centerline, although the exact mechanism of it is not clear. This observation has formed the basis for choosing a longer domain for both the channel and pipe flow, which immediately resolved the issue.

As a final diagnostic step, the divergence within the computational domain is examined by defining the normalized divergence as Equation (4.22). A detailed discussion of this quantity associated with C^1 discontinuity is given in the discussion of the pipe flows in §4.6.5.

$$\mathcal{D} = \frac{S_{ii}}{\sqrt{S_{ij}S_{ji}}}, \tag{4.22}$$

where S_{ij} denotes the strain rate tensor. Note that the normalizing factor $\sqrt{S_{ij}S_{ji}}$ is invariant under coordinate transformations. This quantity is calculated locally and dynamically, and is then averaged over time and the stream-wise direction. Consequently, the distribution of the divergence over the channel cross-section is obtained as shown in Figure 4.3. The plot has a limited colormap legend range to elucidate the divergence error along the wall, of which the maximum divergence is found to be 4×10^{-4}. Although we observe elevated levels of the divergence error along element edges, the maximum value of the normalized divergence is $O(10^{-4})$ and hence the error should not largely affect the computational results.

4.5 Pipe Flow LES with SEMTEX

Our pipe LES requires several modifications to fit with the spectral formulation used in SEMTEX and the pipe geometry. We begin with a discussion of the appropriate choice of the Fourier direction, which finalizes the geometry and coordinate system for the simulation. We then

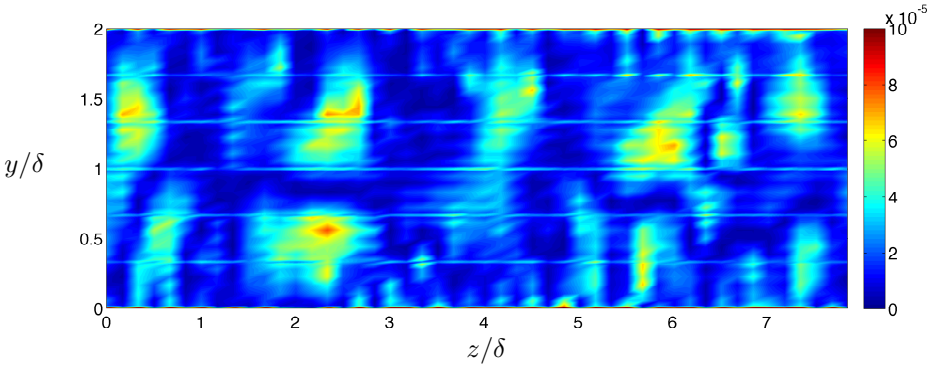

Figure 4.3: Distribution of divergence error on channel cross-section. The maximum level of the divergence is 4×10^{-4} while the colormap is limited to elucidate the element edge behaviors.

continue on to discuss the mathematical adjustments necessary for the stretched vortex SGS model and wall model to conform to a spectral element simulation platform. Finally, a summary of simulation conditions is presented before leading into the results of the numerical study in §4.6.

4.5.1 Cylindrical Formulation and Cartesian Formulation

SEMTEX implements spectral element methods to solve the Navier-Stokes equations on geometries that have at least one periodic direction. In the case of fully developed turbulent pipe flow, this can be either the azimuthal or stream-wise direction. Here, we will consider each formulation separately.

Cylindrical Formulation

The choice of azimuthal direction as the Fourier direction corresponds to solving the Navier-Stokes equations in cylindrical coordinates, and henceforth we refer to the pipe-domain setting with an azimuthal Fourier direction as the "cylindrical formulation." The global coordinates of the cylindrical formation are defined by the radial, azimuthal, and stream-wise directions, which are denoted by r, θ, and z, respectively. Choosing the azimuthal direction as the Fourier direction necessarily results in having the $r-z$ plane as the Fourier plane. These Fourier planes are rectangular-shaped with a rectangular mesh, which is preferred for the stretched vortex model because the neighboring points used to calculate the structure functions, an essential part of the SGS stress calculations, are well defined. Furthermore, the wall normal direction coincides with one of the global axes ($r-$direction) and hence, it requires no coordinate transformations when implementing the wall model. However, in the end the azimuthal Fourier direction has not been not selected since the resulting simulation outputs for mean velocity have shown that profiles are systematically underestimated near the centerline. It is thought that having an increasingly small azimuthal spacing towards the centerline is an issue because of the observed sensitivity of the near-center velocity to how we take the azimuthal contribution to the structure function.

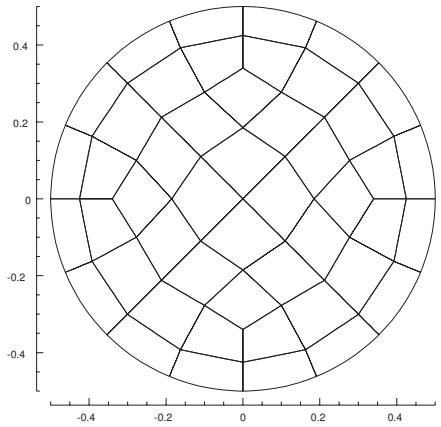

Figure 4.4: Meshed cross section with Cartesian formulation. Currently, forty-eight elements comprise the plane.

Cartesian Formulation

If we instead choose the stream-wise direction as the Fourier direction, the Navier-Stokes equations are solved in Cartesian coordinates, and hence this setup is referred to as Cartesian formulation. With the stream-wise direction chosen as the Fourier direction, the Fourier planes on which the spectral-element methodology is implemented lie in the $r - \theta$ plane and the flow domain is then bounded by the circle $r = R$. The organization of the elements within a Fourier plane is shown in Figure 4.4. This formulation avoids the issue of diminishing angular grid spacing in the cylindrical formulation. The aforementioned under-estimating behavior of the mean velocities associated with the cylindrical formulation is absent, although some additional changes to the stretched vortex SGS model arise, two of which are discussed below.

(A) Neighboring Points: an advantage associated with the cylindrical formulation is the aforementioned rectangular geometry of the Fourier planes, since the local coordinates defined in each element (i, j) are aligned with the global (r, z) coordinates in physical space. Therefore, this geometry has well defined neighboring points that make calculating the structure functions in global coordinates for the SGS model simple. In the Cartesian formulation, this simple calculation is no longer available as elements are no longer structured. Instead of calculating neighboring points in the global system (x, y) similar to the cylindrical formulation, they are evaluated in the local (i, j) coordinate system of each element. An illustration of an element under the Cartesian formulation is given in Figure 4.5, indicating the local coordinate system. In spite of the complexity of finding the indices for each neighboring point among all elements, this is done only once before the simulation begins stepping forward in time, therefore causing little computation overhead.

(B) Cutoff Length Δ_c: The definition of the cutoff length Δ_c also requires modification. The following definition is arrived at.

$$\Delta_{c,ijk} = \left(r_{i+1} r_{i-1} r_{j+1} r_{j-1} r_{k+1} r_{k-1}\right)^{1/6}, \tag{4.23}$$

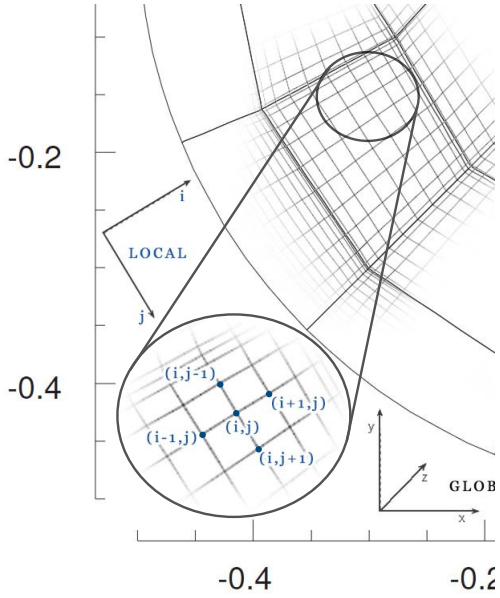

Figure 4.5: Local and global coordinates within the Fourier plane for the Cartesian formulation.

$$\begin{aligned} \text{where } r_{i+1} &= \left((x_{i+1,jk} - x_{ijk})\,(y_{i+1,jk} - y_{ijk})\,(z_{i+1,jk} - z_{c,ijk})\right)^{1/3} \\ r_{j+1} &= \left((x_{i,j+1,k} - x_{ijk})\,(y_{i,j+1,k} - y_{ijk})\,(z_{i,j+1,k} - z_{ijk})\right)^{1/3} \\ r_{k+1} &= \left((x_{ij,k+1} - x_{ijk})\,(y_{ij,k+1} - y_{ijk})\,(z_{ij,k+1} - z_{ijk})\right)^{1/3}. \end{aligned}$$

Other definitions of Δ_c include one based on the volume of an equivalent cube. In a uniform grid, this is defined as $\Delta_c = (r_x r_y r_z)^{1/3}$. Here, r_x, r_y, and r_z are the grid spacings in x, y, and z coordinates, respectively. Note that a cube with each side having length Δ_c would have the same volume as that of each grid, $r_x \times r_y \times r_z$. This definition is used in the channel flows discussed in Chapter 2 and 3. Note that this volume-based definition produces the same equation for Δ_c as Equation (4.23) in the case of uniform grids. It is possible to use a similar definition of Δ_c in nonuniform grids. The corresponding expression for Δ_c in a nonuniform grid is

$$\Delta_{c,ijk} = \left(\frac{r_{i+1} + r_{i-1}}{2}\frac{r_{j+1} + r_{j-1}}{2}\frac{r_{k+1} + r_{k-1}}{2}\right)^{1/3}, \tag{4.24}$$

where the definition of r_{i+1} and the others follow that of Equation (4.23) . However, in this definition, the flow field information from the difference in grid spacings on either side of the node is blurred because of averaging. Nonetheless, we have run some simulations with this definition and found no significant difference in results.

4.5.2 Simulation Conditions for Pipe Flow

We consider a relatively long pipe of roughly the same dimensions as those of the channel flow presented in Chapter 2 and 3. The present domain is set to have dimensions $(R, \theta, l_z) =$

$(0.5, 2\pi, 2\pi/0.4 \approx 15.7)$ and uses approximately 1,500,000 node points. Using the Cartesian formulation, we take the stream-wise $(z-)$ direction as the Fourier direction and use 320 $z-$planes. Each plane consists of 48 elements, as shown in Figure 4.4. Elements are organized into four layers in the radial $(r-)$ direction, with the two outer-most layers having 16 elements around the circumferential $(\theta-)$ direction. Along with the 320 $z-$planes and 10^{th} order polynomials, we aim to have an effective grid size ratio of $dr : dz = 1 : 4$, based on our previous experience in using the stretched vortex SGS model and wall model.

The simulation conditions of pipe LES are summarized in Table 4.1. The Reynolds number based on the pipe radius and friction velocity is varied from approximately $Re_\tau = 2 \times 10^3$ to $Re_\tau = 2 \times 10^6$. Defining the $Re_D = u_b D/\nu$, where D denotes the pipe diameter, the corresponding values are from $Re_D = 9.18 \times 10^4$ and 1.65×10^8, respectively, according to the Blasius correlation. The mean pressure gradient in the stream-wise direction is denoted dp/dz in the table. Also, in the table, the mesh and resolution combination described above is called "regular," while the one with Laplacian smoothing for improved uniformity of the mesh is called "Laplacian Smoothing." This Laplacian smoothing is applied to the mesh, aiming to make the elements more uniform. It acts on the interior vertices of the mesh while leaving the boundary vertices as is. The algorithm re-locates each interior vertex at the average location of the neighboring vertices. The re-location process is repeated iteratively until a satisfactory mesh is achieved.[133] Finally, the case with additional elements near the wall to improve mesh refinement is called "High Resolution."

	Re_τ	ν	dp/dz	Mesh/Resolution
R1	2×10^3	1.09×10^{-5}	7.59×10^{-3}	Regular
R2	2×10^4	8.27×10^{-7}	4.37×10^{-3}	Regular
R3	2×10^5	7.04×10^{-8}	3.17×10^{-3}	Regular
R4	2×10^6	6.06×10^{-9}	2.34×10^{-3}	Regular
L1	2×10^4	8.27×10^{-7}	4.37×10^{-3}	Laplacian Smoothing
H1	2×10^4	8.27×10^{-7}	4.37×10^{-3}	High Resolution

Table 4.1: Simulation conditions for turbulent pipe flows

4.5.3 Element Edge Treatment in the Wall Model

The aforementioned divergence error develops along element edges, which affects both the resolved-scale LES and, indirectly, the solution of the ODE at the wall to obtain u_τ. This tendency is particularly notable at Reynolds numbers above $Re_\tau = 2 \times 10^5$. It is expected that azimuthal distributions of u_τ should be uniform, with both time-wise and $z - \theta$ fluctuations superimposed. While the distributions of friction velocity at $Re_\tau = 2 \times 10^3$ and 2×10^4 have been found to be relatively uniform across the wall surface, at $Re_\tau = 2 \times 10^5$ the distribution has shown that the values of friction velocity along element edges are much smaller than the interior points of each element. When the Reynolds number is 2×10^6, the element edge points have larger values of u_τ compared to those at the interior points. Although this behavior is

rather non-systematic, it is believed to be a consequence of large divergence errors produced by SEMTEX at the wall as the Reynolds number increases. To correct this within SEMTEX itself would require developing a version of SEMTEX that guarantees C^1-continuity at element edges. This is beyond the scope of the present work. As an alternative, we explore strategies for the treatment of the SGS model at element edges that alleviate the divergence-error effect. Three possible techniques to address this issue are discussed here:

(a) No treatment. The wall ODE for u_τ at element-edge nodes are treated the same as any other point along the wall.

(b) The inputs to the wall model at element edge nodes are taken as the average of the interior nodes on the either side of the edge.

(c) A combination of (a) and (b), where the simulations up to $Re_\tau = 2 \times 10^4$ use (a) and those beyond that level use (b).

The results from these three techniques are given in §4.6.2 and a relevant discussion of divergence errors is given in §4.6.5.

4.6 Pipe Flow Results in SEMTEX

4.6.1 Friction Factor in Pipe

The friction factor in turbulent pipe flow is defined in terms of the pressure gradient and dynamic pressure based on the bulk velocity, as shown in Equation (4.25), which can also be expressed in terms of friction velocity [103, 74].

$$f = \frac{-\overline{dp/dz}\, D}{1/2\rho u_b^2} = 8\, \frac{u_\tau^2}{u_b^2}, \tag{4.25}$$

where $\overline{dp/dz}$ is the mean pressure gradient in the axial direction and D is the pipe diameter. Over the full-range of Reynolds number from $Re_\tau = 2 \times 10^3$ to 2×10^6 (R1-R4), the friction factor is plotted against the Reynolds number based on the bulk velocity in Figure 4.6. We find a close agreement of our LES results with empirical evidence.

Using the estimate of u_τ/u_b based on the log-law (see Chapter 2, Equation (2.44)) and Equation (4.25), we can obtain an expression for friction factor. In order to calculate the Kármán constant and additive constant of the log-law, the friction factor data is fit via least squares. We find the values of Karman constant κ and B to be $\kappa = 0.43$ and $B = 5.5$. These values are comparable to values obtained by McKeon *et al.* (2004A)[71], who report $\kappa = 0.42$ and $B = 5.6$.

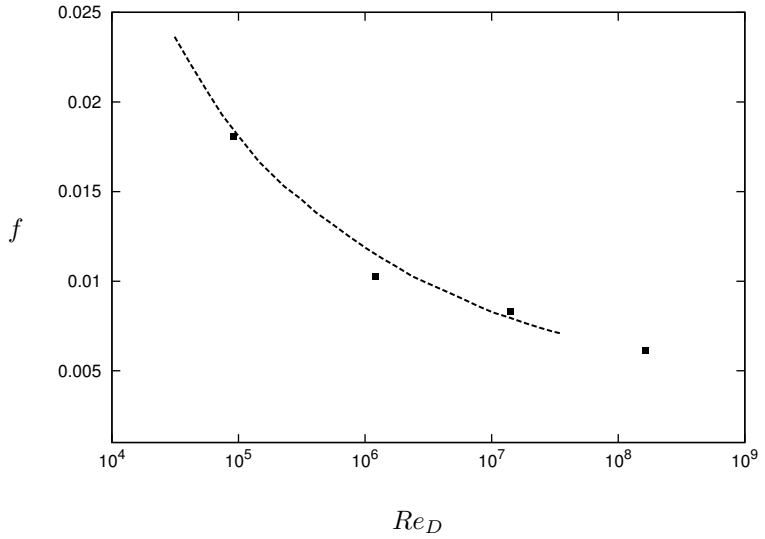

Figure 4.6: Friction factor with Reynolds number based on bulk velocity, based on Method (b). Squares: LES; dashed line: experimental result of McKeon *et al.* (2004B)[74].

4.6.2 Mean Velocity Profiles

The mean velocity profiles of pipe flow simulations at $Re_\tau = 2 \times 10^3$, 2×10^4, 2×10^5, and 2×10^6 (R1-R4) are shown in Figure 4.7, using method (b) from §4.5.3 for the wall model calculation, since it demonstrates good performance. In order to obtain each profile, raw data is first averaged over the stream-wise direction (Fourier direction). Then, the stream-wise-averaged data is sampled at 40 evenly spaced points from the pipe center to the virtual wall. Should one of these sample points not coincide with a knot point of the Gauss-Lobatto-Legendre basis functions, a two-dimensional interpolation is carried out using the polynomials. This sample is referred to as a "ray." Sixteen of such rays are sampled around the circumferential direction with equal angular spacing, and subsequently averaged to obtain the final profile. Recall that there are sixteen elements along the circumference of the pipe and thus the sixteen sample rays can be made to coincide with the center of each of the elements in order to minimize any spurious element edge phenomena along their radial sides. The slip velocity at the virtual wall, which is the lowest data point of the profile in the figure, is exempt from inclusion in the sample rays. Rather than relying on interpolated data based on the basis polynomials, as above, the average of the slip velocity data is taken using samples from the raw wall model output. Samples are taken at the center of each element. This special treatment of the slip velocity attempts to show the available results closest to the wall while avoiding over-interpolation of the data and the over-active behavior at element edges.

Our LES indicates that the Kármán constant is $\kappa = 0.43$, as discussed in §4.6.1, resulting in a good log-law fit for LES data. Although our LES data shows inconsistency at $Re_\tau = 2 \times 10^4$, it captures the overall trend of the mean velocity profile as shown in Figure 4.7.

As discussed in §4.5.3, without any corrections, i.e. method (a), the element edge behaviors on the wall remain largely affected by divergence error. To see why Method (b) is advocated in

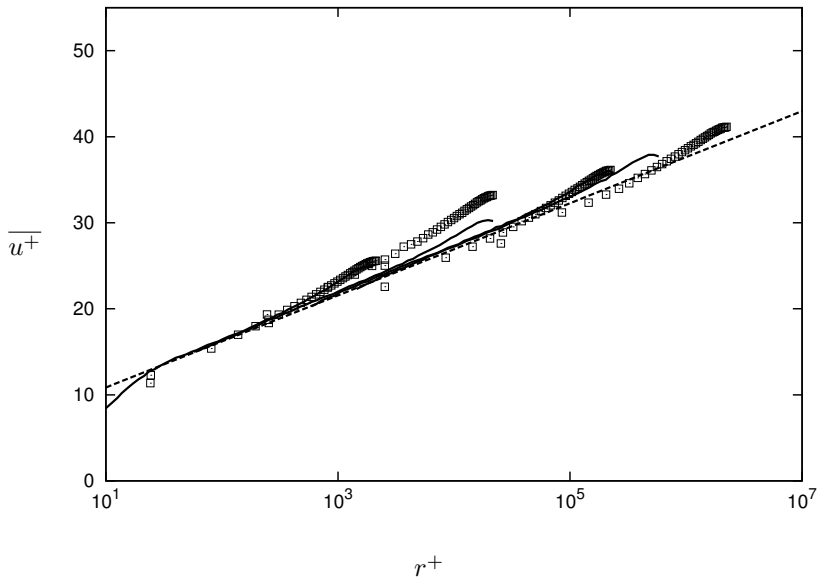

Figure 4.7: Pipe flow mean velocity profiles. Squares: LES using (b); solid line: experiment McKeon *et al.* [71] at $Re_\tau = 1.8 \times 10^3, 2.0 \times 10^4, 2.2 \times 10^5, 5.3 \times 10^5$; dashed line: log-law with $\kappa = 0.43$ and $B = 5.5$, obtained from LES.

the results presented above, Figures 4.8 and 4.9 are given for comparison, which show the mean velocity profiles produced by methods (a) and (c), respectively. When using (a), the profiles are uniformly overestimated, while using (c), they are nearly identical to (b). Because using the same method across different Reynolds numbers is preferred, we have chosen our primary data source for the results as (b), although the results based on (a) are also presented in the rest of this chapter.

4.6.3 Flow Visualizations of Stream-wise Velocity

The instantaneous stream-wise velocity on a representative pipe cross-section is shown in Figure 4.10 at Reynolds numbers $Re_\tau = 2 \times 10^3 - 2 \times 10^6$. It is observed that with increasing Reynolds number, the velocity profiles flatten, as expected of turbulent flow. Note that the mesh does not change with Reynolds number, and hence increasing Reynolds number corresponds to under-resolving the flow more. Consequently, the solution experiences stronger effects of errors associated C^1 discontinuity; evidentially, we observe clearer signs of numerical artifacts along element edges with increasing Reynolds number.

4.6.4 Turbulent Intensities

The stream-wise turbulent intensities at all Reynolds numbers are compiled in Figure 4.11 using method (b). Intensity profiles use the same averaging and uniformly distributed interpolation points as the mean velocity profiles, with the only exception being for data points near the wall. Due to large fluctuations in the turbulent intensities near the wall, the data is not interpolated within the elements adjacent to the wall. Instead, the data at computational nodes are averaged

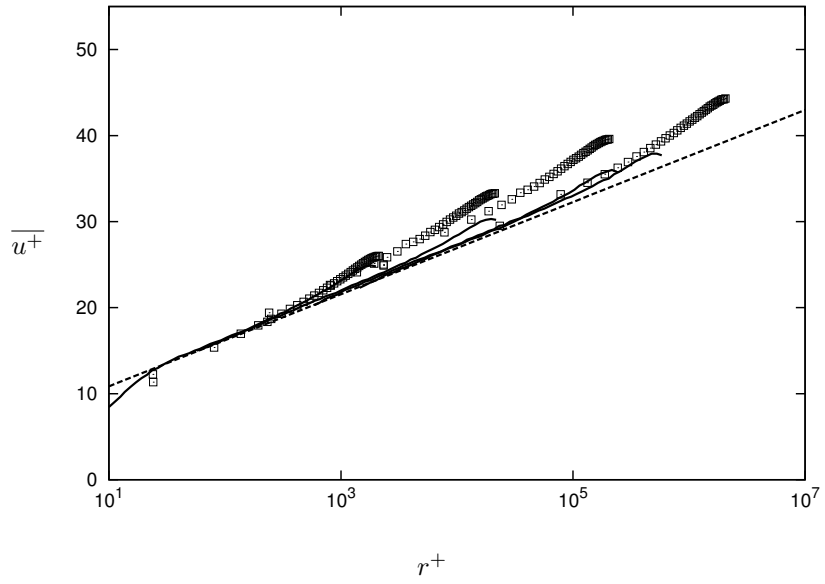

Figure 4.8: Pipe flow mean velocity profiles. Squares: LES using (a); solid line: experiment McKeon *et al.* [71] at $Re_\tau = 1.8 \times 10^3, 2.0 \times 10^4, 2.2 \times 10^5, 5.3 \times 10^5$; dashed line: log-law with $\kappa = 0.43$ and $B = 5.5$, obtained from LES.

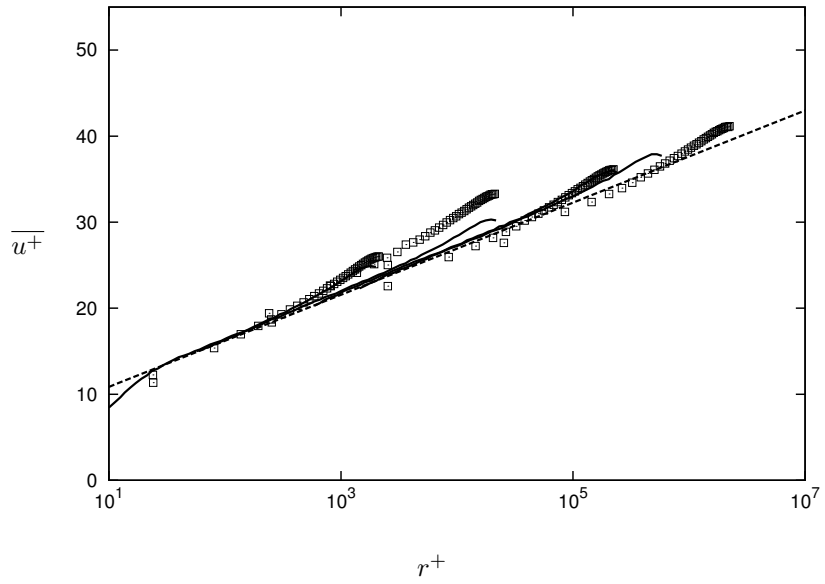

Figure 4.9: Pipe flow mean velocity profiles. Squares: LES using (c); solid line: experiment McKeon *et al.* [71] at $Re_\tau = 1.8 \times 10^3, 2.0 \times 10^4, 2.2 \times 10^5, 5.3 \times 10^5$; dashed line: log-law with $\kappa = 0.43$ and $B = 5.5$, obtained from LES.

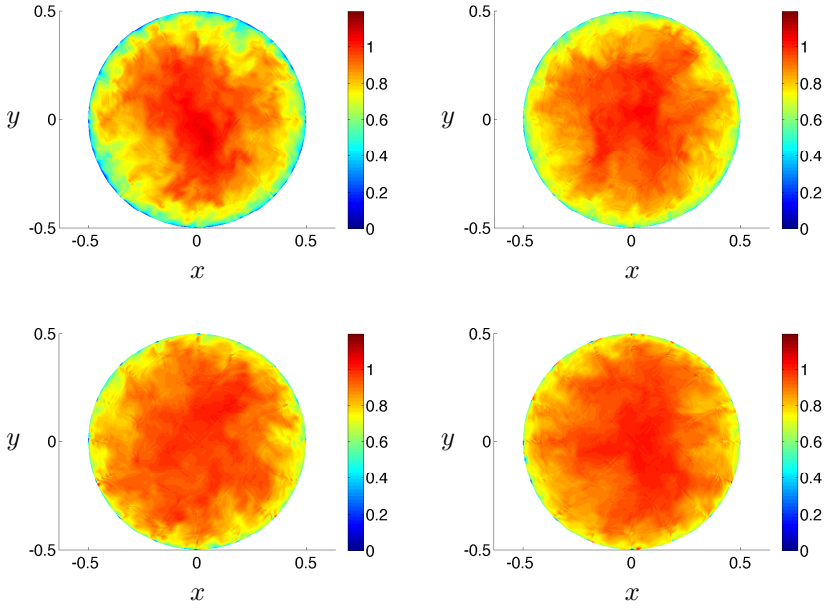

Figure 4.10: Flow visualization of instantaneous stream-wise velocity at $Re_\tau = 2 \times 10^3, 2 \times 10^4, 2 \times 10^5, 2 \times 10^6$

over the azimuthal direction while avoiding the element edges. A reasonable agreement with the experimental results of Hultmark *et al.* [44] at $Re_\tau = 20,251$ is observed, although all of the profiles are slightly lower than the experimental results. When we use the wall model with method (a), the turbulent intensity profiles are closer to the experimental results, as shown in Figure 4.12.

4.6.5 Divergence Error and Reynolds Number

In order to examine the significance of the C^1 discontinuity, we analyze the behavior of the strain rate tensor S_{ij} since it is one of the most directly affected quantities due to C^1 discontinuity, and yet it is an important variable that is included in the SGS stress calculation. Although the true values of S_{ij} are unavailable unless we perform a corresponding DNS simulations, the computational requirement of which is unfeasibly high, we can infer the exact value of an invariant property within the matrix, that the trace of S_{ij} should be always zero due to incompressibility. Therefore, while the error associated with C^1 discontinuity is not confined to the trace, but rather exists in all components of S_{ij}, the analysis proceeds using the trace, which is also known as the divergence error in the context of incompressible flow. In order to study the development of divergence error, the normalized divergence as defined in Equation (4.22) is examined across the pipe cross section. The distribution is shown in Figure 4.13 for the case of $Re_\tau = 2 \times 10^6$; the maximum level of divergence error was 0.18. Again, the figure limits the color legend scale to show the effect at element edges. The divergence error is prominent near the element edges especially along the wall.

The maximum value of the normalized divergence error is tabulated in Table 4.2. We observe

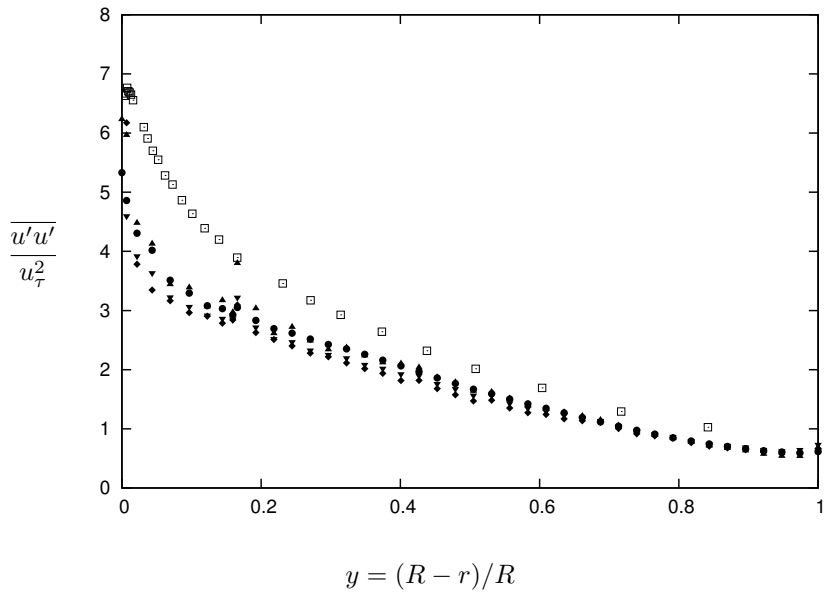

Figure 4.11: Turbulent intensity profiles using method (b). Solid symbols: LES data; circle: $Re_\tau = 2 \times 10^3$, up-pointing triangle: $Re_\tau = 2 \times 10^4$, down-pointing triangle: $Re_\tau = 2 \times 10^5$, star: $Re_\tau = 2 \times 10^6$. Open square: experimental data of Hultmark *et al.* [44] at $Re_\tau = 20,251$.

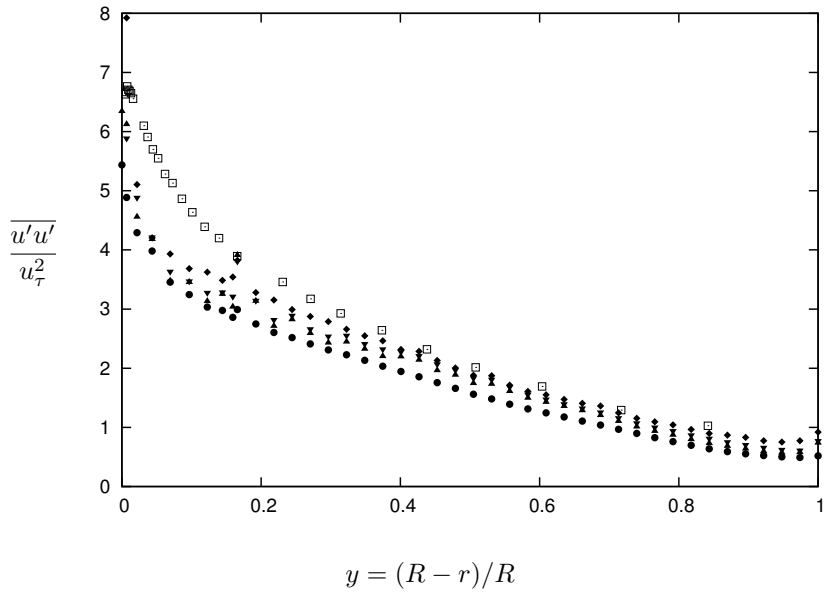

Figure 4.12: Turbulent intensity profiles using method (a). Solid symbols: LES data; circle: $Re_\tau = 2 \times 10^3$, up-pointing triangle: $Re_\tau = 2 \times 10^4$, down-pointing triangle: $Re_\tau = 2 \times 10^5$, star: $Re_\tau = 2 \times 10^6$. Open square: experimental data of Hultmark *et al.* [44] at $Re_\tau = 20,251$

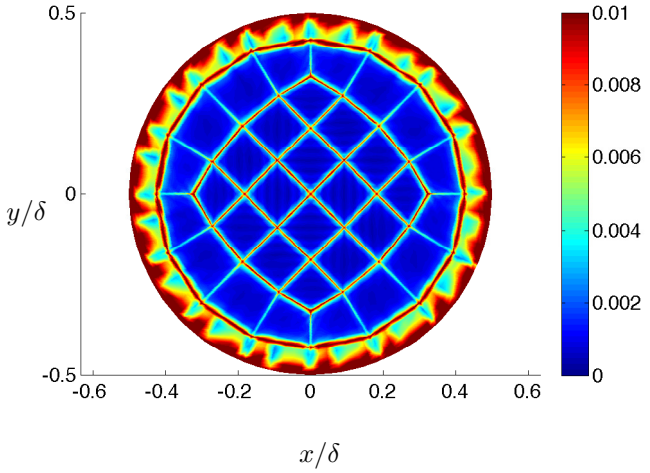

Figure 4.13: Distribution of divergence on pipe cross-section at $Re_\tau = 2 \times 10^6$. The maximum level of the divergence is 0.18 while the colormap shown in the plot is limited to elucidate the element edge behaviors.

a trend of increasing divergence errors with increasing Reynolds numbers except at the lowest Reynolds number, where the error might also be affected by the less than optimal Reynolds number. Compared to the magnitude of the divergence error in the channel flow case, the error in the current pipe geometry is significant. Several attempts have been made to compensate for this error, such as considering dynamic calculation of the cutoff wavelength. We have also increased the near-wall resolution (H1 simulation) and tried to mesh with more uniform elements via Laplacian smoothing (L1 simulation). These strategies, however, have produced no significant improvements in the near-wall divergence error. The observed trend of the divergence error offers possible explanations for the departure of the statistics from the empirical results, although the extent to which it can be attributed to the divergence error is unquantifiable.

Geometry	Re_τ	$\mathcal{D}$
Channel	2×10^6	4.2×10^{-4}
Pipe	2×10^3	0.022
Pipe	2×10^4	0.018
Pipe	2×10^5	0.11
Pipe	2×10^6	0.19

Table 4.2: Maximum divergence error, averaged and normalized.

4.7 Summary and Discussion

In the final chapter of this work, we have used the high Reynolds number LES framework of Chung & Pullin [19], comprising the stretched vortex model and wall model, within a spectral element software platform called SEMTEX, with a view of extending these models in the future to more general geometries. Its numerical scheme has been selected for the advantage it extends in having spectral accuracy when fully resolved and for accommodating complex wall boundaries.

The Navier-Stokes solver that is internal to SEMTEX has been modified in two incremental stages to initially certify the compatibility of the models with the numerical method by simulating a channel flow in Stage 1 and thereafter to approach the full pipe flow problem in Stage 2. The first stage of development has successfully shown agreement of our channel flow results from SEMTEX with those of DNS [43]. Both the SGS model and wall model have performed according to expectations driven by our prior studies of channel flow LES built on finite difference and spectral methods in Chapter 2. The present channel mean velocity profiles have correctly postdicted the log-law profiles and favorably agreed with DNS [43], and the turbulence statistics, scaled on u_τ, have shown collapse across Reynolds numbers and agreement with DNS. A negligibly low level of divergence error has been detected throughout the channel.

The second stage of development has simulated pipe flow in a Cartesian coordinate system, which eliminates pole singularities. The conversion from planar to curvilinear wall boundaries has been presented and wall treatment has been covered. The performance of the spectral element method in under-resolved conditions has initially caused mean velocity profiles to be under-predicted by several percent when compared to the theoretically based log-law; turbulence statistics have been shown to be systematically downward biased. By applying a special treatment to the spectral element edge-nodes at the wall, this issue has been addressed and only partly remedied. Nonetheless, in spite of these errors, the friction factors obtained from the LES have shown agreement with those obtained in the experimental study of McKeon *et al.* [74] and have been used to calculate the Kármán constant and additive constant as $\kappa = 0.43$ and $B = 5.5$. Other possible improvements have been attempted, such as the various ways to calculate the LES cutoff wavelength, Laplacian smoothing of the grid spacing, and near-wall grid refinement, although no entirely satisfactory and systematic solution has been found through these approaches. An alternative appears to be grid refinement up to the level at which the flow is fully resolved and hence the SGS model can be turned off near the wall. This would clearly defeat the point of LES and hence is not pursued.

Looking forward, an alternative numerical method that is easily applied to complex geometries and does not have C^1 discontinuity would hold promise. Alternatively, the models can be improved to handle flows with finite divergence errors. With either of these being achieved, the stretched vortex model and wall model, as well as the roughness model, will see their potential realized in broader application. It is hopeful they will recreate real fluid flow environments with the necessary accuracy to capture roughness effects on complex wall profiles at the high Reynolds numbers that are so prevalent in our world and yet still so inaccessible.

Chapter 5

Conclusions

In Chapter 2, we have established a high Reynolds number roughness model that is incorporated into the LES framework comprising the stretched vortex SGS model coupled to the wall model [19]. Our current modeling framework is capable of handling a wide range of Reynolds numbers and roughness levels, which are specified in terms of equivalent sand roughness within the subgrid range. In the sense that our approach is capable of using any roughness function of the form of Hama's roughness function, i.e. $\Delta U^+ = \Delta U^+(k_{s\infty}^+)$, the roughness function can be considered a model input. Presently, the semi-empirical roughness model has employed the Colebrook formula, directly modifying the wall model while the outer LES is affected only through the information propagated from the slip boundary conditions. By way of a fourth-order central difference and pseudo-spectral method in space and third-order Runge-Kutta method in time, roughness corrected LES has been applied to fully turbulent channel flow over the range of Reynolds number from $Re_\tau = 650 - 2 \times 10^8$.

When used in large-eddy simulation, the roughness model has captured the transitionally rough regime as well as the fully rough regime, giving us an insight into both Reynolds number dependent and independent behaviors in these flows. The gradual plateauing of the flow from the transitionally rough state to fully rough state has been most clearly observed in the friction factor as both Reynolds number and roughness vary, which we have compiled into a chart for channel flow that is analogous to the Moody diagram for a pipe flow. The inner scaled mean velocity profiles have displayed the correct momentum deficit/downward shift due to roughness. When plotted in the deficit form, the velocity profiles have demonstrated support of Townsend's hypothesis and we have detailed another way of finding the equivalent sand roughness given such velocity data. In addition, the collapse of the turbulent statistics has appeared to vary depending on the Reynolds number and roughness; improved collapse has been observed for higher Reynolds numbers and in fully rough cases. These scaling properties for the turbulence statistics and velocity profiles have provided the basis for a theoretical extension in our analysis that examines the infinite Reynolds number limit. As the Reynolds number grows, smooth-walled channel flows tend to plug-flow and rough-walled flows show a universal, roughness corrected mean-velocity deficit profile, together with stream-wise turbulence intensities and total energy dissipation that all scale on the friction factor, which is equivalent to inner scaling. In particular, for smooth-wall

flow the LES has indicated that the second-order turbulent fluctuations over almost all of the channel decline relative to the centerline or bulk velocity with increasing Reynolds number. This is in broad agreement with the LES of a turbulent boundary layer by Inoue & Pullin [46]. While the source of this attenuation from the very-near-wall flow physics cannot be directly captured by the present LES methodology, we note that some progress in this direction can be made by combining LES with near-wall flow models; see Inoue *et al.* [45].

In Chapter 3, our roughness corrected LES has been applied to a dynamic flow scenario where the flow travels over repeated transitions between smooth and rough surface conditions, hence taking advantage of the fact that the wall model operates point-wise across wall surfaces, and so changes in the outer flow can be viewed as a natural response to any temporally and/or spatially variant roughness distribution specified at the wall. The flow recovery to a completely-smooth or -rough state has been shown to vary depending on the quantity of interest, wall normal distance, and type of transition (i.e. smooth to rough or rough to smooth). The mean velocity, as well as friction velocity, have reached full recovery within each strip of length 64δ. The internal boundary layer, defined as the boundary between modified and unmodified flow, has been found using stream-wise turbulent intensity. The growth rate of the internal layer for a $S \to R$ transition has shown an excellent agreement with the power law growth rates of Antonia & Luxton [5] and Efros & Krogstad [27]. We note two main differences in the IBL profiles of $S \to R$ and $R \to S$ transitions. First, the asymptotic growth rate is faster for the $S \to R$ transition than the $R \to S$ transition, although within the region that is observed in this study, the effect of the leading constant in the power law fit dominates the growth rate, and consequently, the IBL reaches the channel centerline after the $R \to S$ transition after than the $S \to R$ transition. Second, the variance in the exponent for the $R \to S$ transition, though it is relatively small, is larger than the $S \to R$ transition. We have also demonstrated the profiles collapse well for each of $S \to R$ and $R \to S$ transitions, when the IBL profiles with different Reynolds numbers and roughness levels are scaled by $\delta / \log(Re_\tau^*)$.

Chapters 2 and 3 have demonstrated that our LES approach is capable of capturing the main outer-flow features of turbulent wall-bounded flow past rough walls, where the length-scale of the roughness is small compared with the outer length scale. Its application to more complex flows – that may include flow transition, body curvature, and separation – remains an area for future research.

The fourth chapter has represented our first step towards extending the models to run in more complex geometry than simple channel flow. In doing so, we have first revisited the numerical method, and in recognizing the flexibility of spectral element method to simulate flows in nearly any geometry, the smooth wall turbulent channel flow results have been reproduced by using the spectral element platform SEMTEX. After confirming the compatibility of the models with the spectral element method in a channel, we have approached the fully developed smooth wall turbulent pipe flow problem. Simulations have realized Reynolds numbers up to $Re_\tau = 2 \times 10^6$. To the best of our knowledge this is the first LES of turbulent pipe flow to make

direct contact with Superpipe data at high Reynolds number. The friction factor has shown favorable agreement with empirical results of McKeon *et al.* [74] while the mean velocity and turbulent statistics have captured the general trend, and yet the simulations have encountered an unsolved C^1 discontinuity error due to the very nature of LES, under-resolvedness in the context of the present spectral-element numerical method. The analysis has revealed that the amount of divergence error is especially pronounced near the element edges and along the wall. Despite the numerous attempts to circumvent the error, the mean velocity profile and turbulent statistics at the highest Reynolds numbers have shown some departure from the empirical results of McKeon *et al.* and Hultmark *et al.* [71, 44]. One conclusion that can be drawn from this work is that a numerical method that guarantees only C^0 continuity is not optimal for the present LES and wall-modeling methodology. In view of realizing the LES of wall-bounded flows in geometries of intermediate complexity, such as pipes and airfoils, it seems clear that a numerical method that provides at least C^1 continuity for under-resolved numerical simulation typical of LES, and that can handle complex geometry, is required.

Chapter 6

Appendix

SEMTEX implements the Galerkin spectral element method to solve the incompressible Navier-Stokes equations. The details are demonstrated in Blackburn & Sherwin [11], but here, we go over the major features of this numerical scheme.

6.1 PDE Setup

The incompressible Navier Stokes equations and continuity equation are given by

$$\frac{\partial \mathbf{u}}{\partial t} + \mathbf{N}(\mathbf{u}) = -\frac{1}{\rho}\nabla p + \nu \nabla^2 \mathbf{u}, \tag{6.1}$$

$$\nabla \cdot \mathbf{u} = 0 \tag{6.2}$$

where the nonlinear term $\mathbf{N}(\mathbf{u})$ employs the skew-symmetric form:

$$\mathbf{N}(\mathbf{u}) \quad = \quad (\mathbf{u} \cdot \nabla \mathbf{u} + \nabla \cdot \mathbf{u}\mathbf{u})/2. \tag{6.3}$$

Although we have implemented the filtered Navier-Stokes equations with the subgrid-scale stress tensor term in place, for simplicity, the description of the numerical methods is given for the original Navier-Stokes equations as above.

When a problem is solved in cylindrical coordinates, the nonlinear term is diagonalized and symmetrized such that the pole singularity is removed, except for the $1/r$ terms. In order to see the consequence of these processes, the nonlinear term is first expressed explicitly as

$$\begin{aligned}
\mathbf{N}(\mathbf{u}) &= (\mathbf{u} \cdot \nabla \mathbf{u} + \nabla \cdot \mathbf{u}\mathbf{u})/2 \qquad (6.4)\\
&= \left(u\frac{\partial u}{\partial z} + u_r\frac{\partial u}{\partial r} + \frac{\partial u u}{\partial z} + \frac{\partial u u_r}{\partial r} + \frac{1}{r}\left(u_\theta \frac{\partial u}{\partial \theta} + \frac{\partial u u_\theta}{\partial \theta} + u u_r\right)\right),\\
&\quad \left(u\frac{\partial u_r}{\partial z} + u_r\frac{\partial u_r}{\partial r} + \frac{\partial u u_r}{\partial z} + \frac{\partial u_r u_r}{\partial r} + \frac{1}{r}\left(u_\theta \frac{\partial u_r}{\partial \theta} + \frac{\partial u_r u_\theta}{\partial \theta} + u_r u_r - 2u_\theta u_\theta\right)\right),\\
&\quad \left(u\frac{\partial u_\theta}{\partial z} + u_r\frac{\partial u_\theta}{\partial r} + \frac{\partial u u_\theta}{\partial z} + \frac{\partial u_r u_\theta}{\partial r} + \frac{1}{r}\left(u_\theta \frac{\partial u_\theta}{\partial \theta} + \frac{\partial u_\theta u_\theta}{\partial \theta} + 3u_r u_\theta\right)\right).
\end{aligned}$$

In cylindrical coordinates, the azimuthal direction is 2π periodic and hence the azimuthal velocity

can be expressed in Fourier frequency space as

$$\mathbf{u}\left(z,r,\theta,t\right)=\sum_{k=-\infty}^{\infty}\hat{\mathbf{u}}_{k}\left(z,r,t\right)e^{ik\theta}, \tag{6.5}$$

where $\hat{(\ )}$ denotes a quantity in the Fourier space. If the geometry is in Cartesian coordinates, the independent variable θ should be replaced by a relevant parameter that is periodic in the domain of interest. Accordingly, the Navier-Stokes equations in Equation (6.1) can be rewritten in Fourier space, which are subsequently diagonalized and symmetrized to arrive at

$$\partial_t r\hat{u}_k + r[\mathbf{N}\left(\mathbf{u}_z\right)]_{\hat{k}} = -\frac{1}{\rho}r\partial_z\hat{p}_k + \nu\left(\partial_z r\partial_z + \partial_r r\partial_r - \frac{k^2}{r}\right)\hat{u}_k \tag{6.6}$$

$$\partial_t r\tilde{u}_{rk} + r[\mathbf{N}\left(\mathbf{u}_r\right)]_{\tilde{k}} = -\frac{1}{\rho}\left(r\partial_r - k\right)\partial_z\hat{p}_k + \nu\left(\partial_z r\partial_z + \partial_r r\partial_r - \frac{\left(k+1\right)^2}{r}\right)\tilde{u}_{rk} \tag{6.7}$$

$$\partial_t r\tilde{u}_{\theta k} + r[\mathbf{N}\left(\mathbf{u}_z\right)]_{\tilde{k}} = -\frac{1}{\rho}\left(r\partial_r + k\right)\partial_z\hat{p}_k + \nu\left(\partial_z r\partial_z + \partial_r r\partial_r - \frac{\left(k-1\right)^2}{r}\right)\tilde{u}_{\theta k} \tag{6.8}$$

$$\partial_z r\hat{u}_k + \partial_r r\hat{u}_{rk} + ik\hat{u}_{\theta l} = 0. \tag{6.9}$$

Here, $\widetilde{(\ )}$ denotes the changes of variables associated with diagonalization [11]. The above equations are free of pole singularities except for $1/r$ terms. Residual $1/r$ terms impose constraints in choosing the expansion bases; the expansion bases must have the property of being zero at the axis for some variables and modes, but they must also have support along the axis whenever the Fourier constant is zero. Currently, SEMTEX utilizes Gauss-Lobatto-Legendre polynomials, although alternatives are available.

6.2 Time-integration scheme

The Navier-Stokes equations can be solved either as is or via a splitting method. By initially separating the pressure contribution from the velocity and correcting the solution thereafter, the splitting method leads to a unique solution for the pressure, given an appropriate boundary condition. This method offers some advantages, including resilience against pressure decoupling. Such an advantage becomes especially relevant at high Reynolds number, where, without splitting, a staggered grid may also offer a way around the issue but for increased computational cost. Thus, the use of a splitting method keeps computational requirements relatively lower and proves to be suitable for our implementation of high Reynolds number LES [55].

The incompressible Navier-Stokes equations and continuity equation are given by

$$\frac{\partial\mathbf{u}}{\partial t} = -\frac{1}{\rho}\nabla p + \nu\mathbf{L}(\mathbf{u}) + \mathbf{N}(\mathbf{u}), \tag{6.10}$$

$$\nabla\cdot\mathbf{u} = 0, \tag{6.11}$$

where the nonlinear and Laplacian terms are denoted by $\mathbf{N}(\mathbf{u})$ and $\mathbf{L}(\mathbf{u})$, respectively. The

time integration employs a stiffy-stable scheme for improved stability. By the use of backward-differentiation, the time derivative at the new time level $(n+1)$ is approximated to Jth order as

$$\frac{\partial \mathbf{u}}{\partial t} = \frac{1}{\Delta t}\sum_{q=0}^{J-1} \alpha_q \mathbf{u}^{n-q+1} + \mathcal{O}(\Delta t^{J+1}), \tag{6.12}$$

The explicit contribution at the new time level is approximated from the previous steps via

$$\mathbf{N}(\mathbf{u}^{n+1}) = \sum_{q=0}^{J-1} \beta_q \mathbf{N}(\mathbf{u}^{n-q}) + \mathcal{O}(\Delta t^{J}), \tag{6.13}$$

where α_q are the discrete weights associated with the implicit stiffy stable scheme, and β_q are the weights associated with the explicit scheme. The values of the weights are given in Karniadakis *et al.*, Table IV [55]. Through these approximations, the Navier-Stokes equations can be expressed as

$$\frac{\alpha_0 \mathbf{u}^{n+1} - \sum_{q=1}^{J-1} \alpha_q \mathbf{u}^{n-q+1}}{\Delta t} = -\frac{1}{\rho}\nabla p + \sum_{q=0}^{J-1} \beta_q \mathbf{N}(\mathbf{u}^{n-q}) + \mathbf{L}(\mathbf{u}^{n+1}), \tag{6.14}$$

where the signs of α_q is inverses for $q > 0$. We define two intermediate velocities, u^* and u^{**} and split Equation (6.14) into three substeps:

$$r\mathbf{u}^* - \sum_{q=1}^{J} \alpha_q r\mathbf{u}^{n-q} = \Delta t \sum_{q=0}^{J-1} \beta_q r\mathbf{N}\left(\mathbf{u}^{n-q}\right) \tag{6.15}$$

$$r\mathbf{u}^{**} - r\mathbf{u}^* = -\frac{r\Delta t}{\rho}\nabla p^{n+1}, \tag{6.16}$$

$$r\nabla^2 \mathbf{u}^{n+1} - \frac{r\alpha_0}{\nu \Delta t}\mathbf{u}^{n+1} = -\frac{r}{\nu \Delta t}\mathbf{u}^{**}. \tag{6.17}$$

Note that we have not thus far used the continuity condition yet. By requiring that the intermediate velocity u^{**} satisfies the continuity as well as the Dirichlet boundary conditions in the direction normal to the boundary, we obtain the pressure Poisson equations:

$$r\nabla^2 p^{n+1} = \frac{\rho}{\Delta t} r\nabla \cdot \mathbf{u}^*, \tag{6.18}$$

$$r\partial_n p^{n+1} = -r\rho \mathbf{n} \cdot \sum_{q=0}^{J-1} \beta_q \left(\mathbf{N}\left(\mathbf{u}^{n-q}\right) + \nu \nabla \times \nabla \times \mathbf{u}^{n-q} + \partial_t \mathbf{u}^{n-q}\right). \tag{6.19}$$

Note that if the problem is solved in Cartesian coordinates, such as in the case of channel flows, the equations are identical except that the computations in Equations (6.15) - (6.19) are performed without the factor of r on either side of the equations.

Bibliography

[1] P. H. Alfredsson, A. Segalini, and R. Örlü. A new scaling for the streamwise turbulence intensity in wall-bounded turbulent flows and what it tells us about the outer peak. *Physics of Fluids*, 23:041702, 2011.

[2] J. J. Allen, M. a Shockling, G. J. Kunkel, and A. J. Smits. Turbulent flow in smooth and rough pipes. *Philosophical transactions. Series A, Mathematical, physical, and engineering sciences*, 365(1852):699–714, March 2007.

[3] W. Anderson and C. Meneveau. Dynamic roughness model for large-eddy simulation of turbulent flow over multiscale, fractal-like rough surfaces. *Journal of Fluid Mechanics*, 679:288–314, May 2011.

[4] J. Andreopoulos and DH Wood. The response of a turbulent boundary layer to a short length of surface roughness. *Journal of Fluid Mechanics*, 118(1):143, 1982.

[5] R. A. Antonia and R. E. Luxton. The response of a turbulent boundary layer to a step change in surface roughness. Part 1. Smooth to rough. *Journal of Fluid Mechanics*, 48(4):721–761, 1971.

[6] R. A. Antonia and R. E. Luxton. The response of a turbulent boundary layer to a step change in surface roughness. Part 2. Rough to smooth. *Journal of Fluid Mechanics*, 53(4):737–757, 1972.

[7] Pal S. Arya. *Introduction to Micrometeorology*, volume 79. Academic Press, 2001.

[8] S. C. C. Bailey, M. Hultmark, J. P. Monty, P. H. Alfredsson, M. S. Chong, R. D. Duncan, J. H. M. Fransson, N. Hutchins, I. Marusic, B. J. McKeon, H. M. Nagib, R. Örlü, A. Segalini, A. J. Smits, and R. Vinuesa. Obtaining accurate mean velocity measurements in high Reynolds number turbulent boundary layers using Pitot tubes. *Journal of Fluid Mechanics*, 2013.

[9] G. I. Barenblatt. Scaling laws for fully developed turbulent shear flows. Part 1. Basic hypothesis and analysis. *Journal of Fluid Mechanics*, 1993.

[10] D. W. Bechert, M. Bruse, W. Hage, J. G. T. Van Der Hoeven, and G. Hoppe. Experiments on drag-reducing surfaces and their optimization with an adjustable geometry. *Journal of Fluid Mechanics*, 338:59–87, 1997.

[11] H. M. Blackburn and S. J. Sherwin. Formulation of a galerkin spectral element-fourier method for three-dimensional incompressible flows in cylindrical geometries. *Journal of Computational Physics*, 2004.

[12] J. P. Bons. A review of surface roughness effects in gas turbines. *Journal of Turbomachinery*, 132(2):021004, 2010.

[13] R. J. Boyle and R. G. Senyitko. Measurements and predictions of surface roughness effects on turbine vane aerodynamics. *ASME paper GT–2003–38580*, 2003.

[14] E. F. Bradley. A micrometeorological study of velocity profiles and surface drag in the region modified by a change in surface roughness. *Quarterly Journal of the Royal Meteorological Society*, 94(401):361–379, 1968.

[15] P. Bradshaw. A note on "critical roughness height," and "transitional roughness". *Physics of Fluids*, 12(6), 2000.

[16] I. P. Castro. Rough-wall boundary layers: mean flow universality. *Journal of Fluid Mechanics*, 585:469, August 2007.

[17] T. Cebeci and P. Bradshaw. *Momentum Transfer in Boundary Layers*. Hemisphere Publishing Corporation, 1977.

[18] H. Cheng and I.P. Castro. Near-wall flow development after a step change in surface roughness. *Boundary-Layer Meteorology*, 105(3):411–432, 2002.

[19] D. Chung and D. I. Pullin. Large-eddy simulation and wall-modeling of turbulent chanel flow. *Journal of Fluid Mechanics*, 631:281–309, 2009.

[20] F. H. Clauser. Turbulent boundary layers in adverse pressure gradients. *Journal of the Aeronautical Sciences*, 21(2):91–108, 1954.

[21] F. H. Clauser. The turbulent boundary layer. *Advances in Applied Mechanics*, (56):1–51, 1956.

[22] C. F. Colebrook. Turbulent flow in pipes, with particular reference to the transition region between the smooth and rough pipe laws. *Journal of the Institution of Civil Engineers (London, England)*, 11:133–156, 1939.

[23] D. E. Coles. The law of the wake in the turbulent boundary layer. *Journal of Fluid Mechanics*, 1(02):191–226, 1956.

[24] D. E. Coles and E. A. Hirst. Computation of turbulent boundary layers. *Proceedings of AFOSR-IFP Stanford Conference*, II(56):1–51, 1969.

[25] J. Counihan. Adiabatic atmospheric boundary layers: A review and analysis of data from the period 1880–1972. *Atmospheric Environment (1967)*, 9(10):871 – 905, 1975.

[26] J. W. Deardorff. A numerical study of three-dimensional turbulent channel flow at large Reynolds numbers. *Journal of Fluid Mechanics.*, 41:453–480, 1970.

[27] V. Efros and P. A. Krogstad. Development of a turbulent boundary layer after a step from smooth to rough surface. *Experiments in fluids*, 51(6):1563–1575, July 2011.

[28] W. P. Elliott. The growth of the atmospheric internal boundary layer. *Transactions, American Geophysical Union*, 39:1048–1054, 1958.

[29] A. Ferrante, G. Matheou, and P. E. Dimotakis. LES of an inclined sonic jet into a turbulent crossflow at mach 3.6. *Journal of Turbulence*, 12(2):1–32, 2011.

[30] K. A. Flack and M. P. Schultz. Review of Hydraulic Roughness Scales in the Fully Rough Regime. *Journal of Fluids Engineering*, 2010.

[31] K. A. Flack, M. P. Schultz, and T. A. Shapiro. Experimental support for Townsend's Reynolds number similarity hypothesis on rough walls. *Physics of Fluids*, 17(3):035102, 2005.

[32] O. Flores and J. Jiménez. Effect of wall-boundary disturbances on turbulent channel flows. *Journal of Fluid Mechanics*, 566:357, October 2006.

[33] H. Foysi and S. Sarkar. The compressible mixing layer: an LES study. *Theoretical and Computational Fluid Dynamics*, 24(6):565–588, 2009.

[34] J. R. Garratt. The internal boundary layer—A review. *Boundary-Layer Meteorology*, 1990.

[35] G. Gioia and P. Chakraborty. Turbulent friction in rough pipes and the energy spectrum of the phenomenological theory. *Physical review letters*, 96(4):044502, 2006.

[36] D. Gottlieb and C.W. Shu. On the Gibbs phenomenon and its resolution. *Society for Industrial and Applied Mathematics Review*, 39(4):644–668, 1997.

[37] C. S. B. Grimmond and T. R. Oke. Aerodynamic properties of urban areas derived from analysis of surface form. *Journal of Applied Meteorology*, 38(9):1262–1292, 1999.

[38] M. Guala, M. Metzger, and B. J. McKeon. Interactions within the turbulent boundary layer at high Reynolds number. *Journal of Fluid Mechanics*, 666:573–604, 2011.

[39] F. R. Hama. Boundary-layer characteristics for smooth and rough surfaces. *Transactions - The Society of Naval Architects and Marine Engineers*, (62):333–351, 1954.

[40] J. M. Hamilton, J. Kim, and F. Waleffe. Regeneration mechanisms of near-wall turbulence structures. *Journal of Fluid Mechanics*, 1995.

[41] M. R. Head and P. Bandyopadhyay. New aspects of turbulent boundary-layer structure. *Journal of Fluid Mechanics.*, 107:297–338, 1981.

[42] M. R. Head and I. Rechenberg. The Preston tube as a means of measuring skin friction. *Journal of Fluid Mechanics*, 14(1), 1962.

[43] S. Hoyas and J. Jiménez. Scaling of the velocity fluctuations in turbulent channels up to $Re_\tau = 2003$. *Physics of Fluids*, 18:011702, 2006.

[44] M. Hultmark, M. Vallikivi, S. Bailey, and A. J. Smits. Turbulent Pipe Flow at Extreme Reynolds Numbers. *Physical Review Letters*, 2012.

[45] M. Inoue, R. Mathis, and I.s Marusic. Inner-layer intensities for the flat-plate turbulent boundary layer combining a predictive wall-model with large-eddy simulations. *Physics of Fluids*, 2012.

[46] M. Inoue and D. I. Pullin. Large-eddy simulation of the zero-pressure-gradient turbulent boundary layer up to $Re_\theta = \mathcal{O}(10^{12})$. *Journal of Fluid Mechanics*, pages 1–27, September 2011.

[47] N. A. Jackson. The propagation of modified flow downstream of a change in roughness. *Quarterly Journal of the Royal Meteorological Society*, 102(434):924–933, 1976.

[48] P. S. Jackson. On the displacement height in the logarithmic velocity profile. *Journal of Fluid Mechanics*, 111:15–25, 1981.

[49] I. Jacobi and B. J. Mckeon. Dynamic roughness perturbation of a turbulent boundary layer. *Journal of Fluid Mechanics*, 2011.

[50] I. Jacobi and B. J. McKeon. New perspectives on the impulsive roughness-perturbation of a turbulent boundary layer. *Journal of Fluid Mechanics*, 2011.

[51] W. Jacobs. Variation in Velocity Profile with Change in Surface Roughnesss of Boundary. Technical report, National Advisory Commitee for Aeronautics: NACA Technical Memorandum, SeptemberJ 1940.

[52] J. Jiménez. Turbulent flows over rough walls. *Annual Review of Fluid Mechanics*, 36(1):173–196, January 2004.

[53] J. Jiménez and P. Moin. The minimal flow unit in near-wall turbulence. *Journal of Fluid Mechanics.*, 225:213–240, 1991.

[54] J. Jiménez and A. Pinelli. The autonomous cycle of near-wall turbulence. *Journal of Fluid Mechanics*, 389(1):335–359, 1999.

[55] G. E. Karniadakis, M. Israeli, and S. A. Orszag. High-order splitting methods for the incompressible Navier-Stokes equations. *Journal of Computational Physics*, 1991.

[56] G. E. Karniadakis and S. J. Sherwin. *Spectral/hp Element Methods for Computational Fluid Dynamics*. Oxford University Press, 2005.

[57] A. Kendall and M. Koochesfahani. A method for estimating wall friction in turbulent boundary layers. *AIAA*, 3834:2006, 2006.

[58] J. Klewicki, P. Fife, and T. Wei. On the logarithmic mean profile. *Journal of Fluid Mechanics*, 638:73, 2009.

[59] P. A. Krogstad, R. A. Antonia, and L. W. B. Browne. Comparison between rough- and smooth-wall turbulent boundary layers. *Journal of Fluid Mechanics.*, 245:599–617, 1992.

[60] G. J. Kunkel and I. P. Marusic. Study of the near-wall-turbulent region of the high-Reynolds-number boundary layer using an atmospheric flow. *Journal of Fluid Mechanics.*, 548:375–402, 2006.

[61] J. LeHew. *Spatio-temporal analysis of the turbulent boundary layer and an investigation of the effects of periodic disturbances.* PhD thesis, California Institute of Technology, 2012.

[62] S. Leonardi, P. Orlandi, and R. A. Antonia. Properties of d- and k-type roughness in a turbulent channel flow. *Physics of Fluids*, 19(12):125101, 2007.

[63] S. Leonardi, P. Orlandi, R.J. Smalley, L Djenidi, and R.A. Antonia. Direct numerical simulations of turbulent channel flow with transverse square bars on one wall. *Journal of Fluid Mechanics.*, 491:229–238, 2003.

[64] T. S. Lundgren. Strained spiral vortex model for turbulent fine structure. *Physics of Fluids*, 25:2193–2203, 1982.

[65] R. W. Macdonald, R. F. Griffiths, and D. J. Hall. An improved method for the estimation of surface roughness of obstacle arrays. *Atmospheric environment*, 32(11):1857–1864, 1998.

[66] H. Makita. PhD thesis, University of Tokyo, 1968.

[67] I. Marusic and G. J. Kunkel. Streamwise turbulence intensity formulation for flat-plate boundary layers. *Physics of Fluids*, 15(8):2461, 2003.

[68] I. Marusic, B. J. McKeon, P. A. Monkewitz, H. M. Nagib, A. J. Smits, and K. R. Sreenivasan. Wall-bounded turbulent flows at high Reynolds numbers: Recent advances and key issues. *Physics of Fluids*, 22(6):065103, 2010.

[69] I. Marusic, J. P. Monty, M. Hultmark, and A. J. Smits. On the logarithmic region in wall turbulence. *Journal of Fluid Mechanics*, 2013.

[70] G. Matheou, A. M. Bonanos, C. Pantano, and P. E. Dimotakis. Large-eddy simulation of mixing in a recirculating shear flow. *Journal of Fluid Mechanics*, 646:375, March 2010.

[71] B. J. McKeon, J. Li, W. Jiang, J. F. Morrison, and A. J. Smits. Further observations on the mean velocity distribution in fully developed pipe flow. *Journal of Fluid Mechanics*, 501:135–147, 2004.

[72] B. J. Mckeon and J. F. Morrison. Asymptotic scaling in turbulent pipe flow. *Philosophical Transactions of the Royal Society A: Mathematical, Physical and Engineering Sciences*, 2007.

[73] B. J. McKeon and A. S. Sharma. A critical-layer framework for turbulent pipe flow. *Journal of Fluid Mechanics*, 658:336–382, 2010.

[74] B. J. McKeon, C. J. Swanson, M. V. Zagarola, R. J. Donnelly, and A. J. Smits. Friction factors for smooth pipe flow. *Journal of Fluid Mechanics*, 2004.

[75] M. M. Metzger and J. C. Klewicki. A comparative study of near-wall turbulence in high and low Reynolds number boundary layers. *Physics of Fluids*, 2001.

[76] M. M. Metzger and J.C. Klewicki. A comparative study of near-wall turbulence in high and low Reynolds number boundary layers. *Physics of Fluids*, 13:692–701, 2001.

[77] C. B. Millikan. A critical discussion of turbulent flows in channels and circular tubes. In *Proceedings of the 5th International Congress of Applied Mechanics*, pages 386–392, 1938.

[78] A. Misra and D. I. Pullin. A vortex-based subgrid stress model for large-eddy simulation. *Physics of Fluids*, 9:2443–2454, 1997.

[79] P. Moin and J. Kim. Numerical investigation of turbulent channel flow. *Journal of Fluid Mechanics.*, 118:341–377, 1982.

[80] A. S. Monin. The atmospheric boundary layer. *Annual Review of Fluid Mechanics*, 2:225–250, 1970.

[81] J. P. Monty. *Developments in smooth wall turbulent duct flows.* PhD thesis, The University of Melbourne, 2005.

[82] L. F. Moody. Friction factors for pipe flow. *Transactions of ASME*, 66(8):671–684, 1944.

[83] Y. Morinishi, T.S. Lund, O.V. Vasilyev, and P. Moin. Fully conservative higher order finite difference schemes for incompressible flow. *Journal of Computational Physics*, 143(1):90–124, 1998.

[84] J. F. Morrison, B.J. McKeon, W. Jiang, and A.J. Smits. Scaling of the streamwise velocity component in turbulent pipe flow. *Journal of Fluid Mechanics*, 508:99–131, 2004.

[85] A. Nakayama, K. Hori, and R.L. Street. Filtering and LES of flow over irregular rough boundary. *Center for Turbulence Res.: Proc. of Summer Prof.*, pages 145–156, 2004.

[86] J. W. Naughton and J. L. Brown. Surface interferometric skin-friction measurement technique.

[87] T. B. Nickels, I. Marusic, S. Hafez, N. Hutchins, and M. S. Chong. Some predictions of the attached eddy model for a high Reynolds number boundary layer. *Philosophical Transactions of the Royal Society* A, 365:807–822, 2007.

[88] J. Nikuradse. Strömungsgestze in rauhen rohren. *V.D.I. Forschungsheft*, -(361):1–22, 1933.

[89] P. Orlandi and S. Leonardi. DNS of turbulent channel flows with two- and three-dimensional roughness. *Journal of Turbulence*, 7(January 2012):N73, January 2006.

[90] P. Orlandi, S. Leonardi, R. Tuzi, and R. A. Antonia. Direct numerical simulation of turbulent channel flow with wall velocity disturbances. *Physics of Fluids*, 15(12):3587, 2003.

[91] J. M. Österlund. *Experimental studies of zero pressure-gradient turbulent boundary layer flow.* PhD thesis, KTH, Mechanics, 1999.

[92] J. M. Österlund, A. V. Johansson, H. M. Nagib, and M. H. Hites. A note on the overlap region in turbulent boundary layers. *Physics of Fluids*, 12(1):1, 2000.

[93] H. A. Panofsky and A. A. Townsend. Change of terrain roughness and the wind profile. *Quarterly Journal of the Royal Meteorological Society*, 90(384):147–155, 1964.

[94] V. C. Patel. Calibration of the preston tube and limitations on its use in pressure gradients. *Journal of Fluid Mechanics*, 23:185–208, 1965.

[95] W. Pendergrass and SPS Arya. Dispersion in neutral boundary layer over a step change in surface roughnessi. mean flow and turbulence structure. *Atmospheric Environment*, 18(7):1267–1279, 1984.

[96] J. B. Perot. An analysis of the fractional step method. *Journal of Computational Physics*, 108(1):51–58, 1993.

[97] A. E. Perry and M. S. Chong. On the mechanism of wall turbulence. *Journal of Fluid Mechanics.*, 119:173–217, 1982.

[98] A. E. Perry and P. N. Joubert. Rough-wall boundary layers in adverse pressure gradients. *Journal of Fluid Mechanics*, 17(2):193–211, 1963.

[99] A. E. Perry and J. D. Li. Experimental support for the attached-eddy hypothesis in zero-pressure- gradient turbulent boundary layers. *Journal of Fluid Mechanics*, 1990.

[100] U. Piomelli. Wall-layer models for large-eddy simulation. *Prog. Aero. Sci.*, 44:437–446, 2008.

[101] U. Piomelli and E. Balaras. Wall-layer models for large-eddy simulations. *Annu. Rev. Fluid Mech.*, 34:349–374, 2002.

[102] H. Pitsch. Large-Eddy Simulation of Turbulent Combustion. *Annual Review of Fluid Mechanics*, 38(1):453–482, 2006.

[103] S. B. Pope. *Turbulent flows*. Cambridge University Press, 2000.

[104] L. Prandtl. Neuere Ergebnisse der Turbulenzforschung. *Zeitschrift des Vereines Deutscher Ingenieure*, 77, February 1933.

[105] J. H. Preston. Determination of turbulent skin friction by means of pitot tubes. *Journal of the Royal Aeronautical Society*, 1954.

[106] D. I. Pullin, M. Inoue, and N. Saito. On the asymptotic state of high Reynolds number, smooth-wall turbulent flows. *Physics of Fluids*, 2013.

[107] D. I. Pullin and P. G. Saffman. Vortex dynamics in turbulence. *Annual review of fluid mechanics*, **30**:31–51, 1997.

[108] K. S. Rao, J. C. Wyngaard, and O. R. Cote. The structure of the two-dimensional internal boundary layer over a sudden change of surface roughness. *Journal of Atmospheric Sciences*, 1974.

[109] M. R. Raupach, R. A. Antonia, and S. Rajagopalan. Rough-wall turbulent boundary layers. *Applied Mechanics Reviews*, 44(1):1–25, 1991.

[110] O. Reynolds. On the dynamical theory of incompressible viscous fluids and the determination of the criterion. *Proceedings of the Royal Society of London*, 56(336-339):40–45, 1894.

[111] S. K. Robinson. Coherent motions in the turbulent boundary layer. *Annu. Rev. Fluid Mech.*, 23:601–639, 1991.

[112] M. Rudman and H. M. Blackburn. Large eddy simulation of turbulent pipe flow. *Second International Conference on CFD in the Minerals & Process Industries*, 1999.

[113] Namiko Saito, Dale I Pullin, and Michio Inoue. Large eddy simulation of smooth-wall, transitional and fully rough-wall channel flow. *Physics of Fluids*, 24(7):075103, 2012.

[114] H Schlichting. *Boundary-Layer Theory*. McGraw-Hill, 1968.

[115] G.B. Schubauer and C.M. Tchen. *Turbulent Flow*. Princeton University Press., 1961.

[116] M. P. Schultz and K. A. Flack. The rough-wall turbulent boundary layer from the hydraulically smooth to the fully rough regime. *Journal of Fluid Mechanics*, 580:381, May 2007.

[117] M. P. Schultz and K. A. Flack. Turbulent boundary layers on a systematically varied rough wall. *Physics of Fluids*, 21:Art. No 015104, 2009.

[118] C. C. Shir. A numerical computation of air flow over a sudden change of surface roughness. *Journal of Atmospheric Sciences*, 1972.

[119] M. A. Shockling, J. J. Allen, and A. J. Smits. Roughness effects in turbulent pipe flow. *Journal of Fluid Mechanics.*, 564(564):267–285, 2006.

[120] R. L. Simpson. A generalized correlation of roughness density effects on the turbulent boundary layer. *AIAA Journal*, 11(2):242–244, 1973.

[121] J. Smagorinsky. General circulation experiments with the primitive equations. i. the basic experiment. *Mon. Weather Rev.*, 91:99–164, 1963.

[122] A. J. Smits, B. J. McKeon, and I. Marusic. High Reynolds number wall turbulence. *Annual Review of Fluid Mechanics*, 43(1):353–375, January 2011.

[123] A. J. Smits, S. T. B. Young, and P. Bradshaw. The effect of short regions of high surface curvature on turbulent boundary layers. *Journal of Fluid Mechanics*, 94:209–242, 1979.

[124] W. H. Snyder and I. P. Castro. The critical reynolds number for rough-wall boundary layers. *Journal of Wind Engineering and Industrial Aerodynamics*, 90:41–54, 2002.

[125] P. R. Spalart, R. D. Moser, and M. M. Rogers. Spectral methods for the Navier–Stokes equations with one infinite and two periodic directions. *J. Comp. Phys.*, 96:297–324, 1991.

[126] M. F. Tachie, D. J. Bergstrom, and R. Balachandar. Rough wall turbulent boundary layers in shallow open channel flow. *J. Fluids Engng.*, 122:533–541, 2000.

[127] A. Talamelli, F. Persiani, J. H. M. Fransson, P Henrik Alfredsson, A. V. Johansson, H. M. Nagib, J. D. Rüedi, K. R. Sreenivasan, and P. A. Monkewitz and. CICLoPE—a response to the need for high Reynolds number experiments. *Fluid Dynamics Research*, 2009.

[128] I. Tani. Boundary-layer transition. *Annual Reviews of Fluid Mechanics*, 1(1):169–196, 1969.

[129] J. A. Templeton, G. Medic, and G. Kalitzin. An eddy-viscosity based near-wall treatment for coarse grid large-eddy simulation. *Physics of Fluids*, 17:105–101, 2005.

[130] J. A. Templeton, M. Wang, and P. Moin. A predictive wall model for large-eddy simulation based on optimal control techniques. *Physics of Fluids*, 20:065–104, 2008.

[131] A. A. Townsend. *The structure of turbulent shear flow.* Cambridge University Press, second edition, 1976.

[132] M. Vallikivi, M. Hultmark, S. C. C. Bailey, and A. J. Smits. Turbulence measurements in pipe flow using a nano-scale thermal anemometry probe. *Experiments in fluids*, 51(6):1521–1527, 2011.

[133] J. Vollmer, R. Mencl, and H. Mueller. Improved laplacian smoothing of noisy surface meshes. In *Computer Graphics Forum*, volume 18, pages 131–138. Wiley Online Library, 1999.

[134] T. Von Kármán. Mechanical similitude and turbulence. *NACA Technical Mememorandum*, 611, 1931.

[135] W. Weng, P. A. Taylor, and J. R. Salmon. A 2-d numerical model of boundary-layer flow over single and multiple surface condition changes. *Journal of Wind Engineering and Industrial Aerodynamics*, 98(3):121 – 132, 2010.

[136] X. Wu and P. Moin. Direct numerical simulation of turbulence in a nominally zero-pressure-gradient flat-plate boundary layer. *Journal of Fluid Mechanics*, 630:5–41, 2009.

[137] M.V. Zagarola and A. J. Smits. Mean-flow scaling of turbulent pipe flow. *Journal of Fluid Mechanics*, 1998.